Polarization spectroscopy of Lyman-α for the study of anisotropic electron velocity distribution function in fusion plasma

Nilam Balkrishna NIMAVAT

Doctor of Philosophy

Department of Fusion Science

School of Physical Sciences

SOKENDAI (The Graduate University for Advanced Studies)

2019 School Year

Abstract

A principal object of the controlled fusion is to confine the plasma for a sufficient time. Confining a fusion grade plasma by means of strong magnetic fields has been emerged as the most effective approach that can lead to achieve thermonuclear fusion. The transport of particles and energy in a plasma is a serious problem that limits confinement. At present there is considerable theoretical interest in the transport effects associated with a high-temperature plasma in toroidal confinement devices.

The electron velocity distribution function (EVDF) in a plasma is one of the most important attributes of the plasma. It is essential in determining the ionization rates of atoms and ions, electric current, heat flow, and other transport phenomena. Often the EVDF is assumed to be isotropic without any experimental or theoretical verification. In some cases EVDF may show substantial anisotropy. The EVDF can be anisotropic in magnetically confined plasma such as tokamaks, helical devices, and mirror devices due to several reasons, e.g., in presence of electromagnetic wave heating, the variation in magnetic field strength. The measurement of anisotropy in the EVDF is indispensable for understanding transport phenomena, equilibria, and current drive in a fusion plasma. Although the anisotropic EVDF plays a key role in a magnetically confined fusion plasma, it has not been actively investigated in plasma experiments.

There are several local diagnostics methods to determine anisotropic EVDF such as a direction Langmuir probe. However, the use of Langmuir probes are limited to low temperature and low density plasmas. A possibility to diagnose anisotropic distribution functions by means of the Thomson scattering measurement

was also investigated. In addition, techniques e.g., absorption of waves and polarization in emission lines of atoms or ions have been subject of interest with the main goal of obtaining anisotropy in the EVDF.

The results of theoretical calculations and electron beam impact experiments indicates that collisional excitation by electrons having anisotropic velocity distribution creates inhomogeneous distribution of population among the magnetic sublevels in excited levels. The imbalance of population among magnetic sublevels is expressed with a quantity known as the "alignment". The emission lines from such aligned levels are generally polarized. Thus, plasma polarization spectroscopy provides a possibility to study anisotropy in the EVDF. The advantage of this method is that it is a non-perturbative method. Also, spectroscopic measurements are unaffected by RF or microwave field and also they do not contaminate the plasma.

Spectral profiles of a hydrogen line from the LHD (Large Helical Device) plasma have been studied earlier and emission locations were identified on the magnetic field map. The results indicate that the dominant emissions are located outside confined region of the plasma. In such regions the confinement characteristics of electrons are strongly dependent on their velocity pitch angle with respect to the magnetic field direction. Due to the varying magnetic field strength in LHD, electrons move under influence of a mirror effect. Electrons having a small pitch angle with respect to the magnetic field direction, known as passing electrons, can escape easily from the magnetic mirror while those with a large pitch angle, known as trapped electrons, are trapped inside the ripples of the magnetic field strength. This factor may cause anisotropy in the EVDF in the edge LHD plasma.

The main objective of this thesis work is to study anisotropy in the EVDF by means of the polarization spectroscopy. Since reliable data of the cross sections for population creation and alignment creation are available for the Lyman-α line at 121.57 nm, it is possible to develop a plasma diagnostics using polarization characteristics of this line for the purpose of determining the anisotropic EVDF. Additionally, the simple energy level structure of this line enables construction of

an accurate theoretical model which makes it more favorable to use in the present studies.

Polarization-resolved measurements of the hydrogen Lyman-α line have been carried out in LHD to measure the polarization in Lyman-α coming from the edge LHD plasma. On the other hand, to be able to interpret the anisotropy in the EVDF in terms experimentally measured polarization degree construction of the Population-Alignment Collisional-Radiative (PACR) model is necessary. Thus, the present work mainly consists of two parts: (i) development of the PACR model for Lyman-α and (ii) measurement of polarization degree in Lyman-α line.

The polarization measurement system on LHD uses a normal incidence monochromator and additionally installed optical components, namely, a high-reflectivity mirror, a polarization analyzer, and a half-waveplate. These optical components have been designed and developed by the CLASP (Chromospheric Lyman-Alpha Spectro-Polarimeter) team. The exhaustive testing of the performance of these components was carried out by the CLASP team using the UVSOR (Ultraviolet Synchrotron Orbital radiation) facility located at Okazaki, Japan.

Inside the spectrometer the high-reflectivity mirror and the polarization analyzer have been installed before the CCD detector, while the half-waveplate is placed just after the entrance slit and it is continuously rotated during the measurement. The main purpose of using the polarization analyzer is to extract one linear polarization component from an incident light based on the principle of polarization of light by reflection at Brewster's angle. The mirror works to incident the diffracted light coming from the grating to the polarization analyzer at its Brewster's angle, i.e., 68°. By using combination of the rotating half-waveplate and the polarization analyzer, linearly polarized Lyman-α line at all angles has been measured. From obtained spectra temporal profiles of the Lyman-α have been generated. The intensity shows a modulation which is synchronized with the half-waveplate rotation period, confirming that the line is polarized.

Polarization degree has been evaluated for many LHD discharges with different plasma parameters. The dependence of polarization degree on electron

density has been investigated. With increasing electron density decrease in polarization degree is anticipated due to two possibilities (i) the anisotropy in the EVDF itself reduces with increasing electron density and (ii) the collisional relaxation of the imbalance of population among the magnetic sublevels. However, it has been found that measured polarization degree does not show clear dependence on electron density.

The results of previous studies carried out on the LHD plasma, indicates that the dominant emissions of hydrogen are located outside the confined region of the plasma and it can be approximated that they are located at $r_{\text{eff}} = 0.67\,\text{m}$. Here r_{eff} is the effective minor radius of plasma. From this result it is clear that on the spectrometer line of sight ($Z = -0.4\,\text{m}$) Lyman-α is emitted from two locations, i.e., $r_{\text{eff}} = \pm 0.67\,\text{m}$. Negative and positive values represent the inboard side and the outboard side of the device, respectively. The measured intensity consists of emission from both the sides and it is not possible to know individual contribution from these two emissions.

The known magnetic field parameters at emission locations in LHD enable to generate synthetic profiles of Lyman-α emission at the inboard and outboard sides separately. From such study the information regarding dominant emission location and relation between the phase of experimental intensity and the magnetic field direction can be obtained. The results of this phase analysis indicate that in the experimental intensity the dominant contribution to the polarized emission comes from the emission at the inboard side plasma. Also, it has been found that the synthetic profile for the inboard side agrees with measured profile only when the polarization degree is negative. This observation suggests that the electron temperature in the direction perpendicular ($T_{\perp}$) to the magnetic field is higher than electron temperature in the direction parallel ($T_{\parallel}$) to the magnetic field.

Information regarding dominant populating and depopulating processes relating to 2P level of hydrogen is prerequisite for development of the PACR model for Lyman-α line. The Collisional-Radiative (CR) model is a very useful tool for this investigation. We have made collisional radiative calculations concerning 2P

level of hydrogen considering the plasma parameters at the Lyman-α emission region, T_e : 10 eV–30 eV and n_e : $10^{18}\,m^{-3}$–$10^{19}\,m^{-3}$. Here T_e and n_e stand for electron temperature and electron density, respectively. It has been found that the main populating process is the electron-impact excitation from the ground state and the dominant depopulating process is the radiative decay to the ground state. On the basis of this knowledge rate equations for the population and alignment have been constructed in the PACR model.

The PACR model is extension of the CR model, in which the alignment of levels is also treated in addition to the populations of levels. We have developed the PACR model for Lyman-α line considering the edge LHD plasma conditions, where the Lyman-α is emitted, and actual geometry of present measurements. The present model treats an anisotropic EVDF having different $T_\parallel$ and $T_\perp$. The rate equations for the population and the alignment have been solved under the quasi steady-state approximation. By comparing the experimental results with the theoretical results the anisotropy in the EVDF has been evaluated for many LHD discharge with different plasma conditions. The variation in anisotropy with n_e and T_e has been investigated. Although decrease in anisotropy is anticipated with increase in n_e due to collisional relaxation, the results indicate that anisotropy does not exhibit any clear dependence on n_e. It has been found that anisotropy demonstrates very clear increasing behavior with increasing T_e. Such behavior of anisotropy is expected because with increasing T_e the reduced collisionality results in higher anisotropy.

In conclusion, by comparing the experimental polarization degree with the theoretical model results anisotropy in the EVDF has been evaluated for many LHD discharges with various plasma conditions. It has been found that anisotropy in the EVDF mainly depends on T_e and it increases with increasing T_e. The results obtained through this thesis work provide significant information regarding anisotropy in the EVDF in the edge LHD plasma, which is of considerable importance in understanding plasma confinement and transport phenomena in the LHD plasma.

Dedicated to the loving memory of my elder brother,

Yagnesh Ramaiya

Acknowledgments

Foremost, I would like to express my deepest and sincere gratitude to my supervisor Dr. Motoshi Goto for giving me this golden opportunity to work him and for his continuous support, patience, and motivation during the study. His excellent guidance helped me in all the time of research and I am indebted to him for this. He has been a true inspiration for me to grow as a research scientist. The knowledge and skills I gained from working with him are priceless.

I am grateful to Dr. Tetsutarou Oishi for many interesting discussions and his support during the experimental work and carrying out experiments at UVSOR facility. My heartfelt thanks goes to Prof. Shigeru Morita for his encouragement and many insightful suggestions. I am thankful to Dr. Ryohei Makino for his kind help and involvement in performing experiments at UVSOR facility. Also, I would like to express my sincere gratitude to the professors of NIFS for very interesting lectures on plasma physics, and scientific English and for the tremendous efforts they made to make lectures more informative and understandable. A special thanks goes to Prof. Byron Peterson for his lectures on scientific English writing and for his help to improve my manuscripts. I am very thankful to Dr. Kenneth Robinson for carefully reading manuscripts and for his many important suggestions to improve my scientific English writing skills.

I gratefully acknowledge the financial support I received from the Japanese government during these three years of my study in Japan. My sincere thanks and appreciation goes to the staff of Graduate Student Affairs Section for the kind help they offered me from finding an apartment in Tajimi to their kind cooperation related to any academic concerns.

My most sincere thanks goes to my colleague Junki Morimoto for his generous help in dealing with the work related to my daily life in Japan. I am indebted to him for all his support and help that his has offered me. I am very

thankful to Dr. Norihiro Ikemoto for giving me many useful things to use at apartment. I am grateful to the technical staff of LHD Experiment Group for their support in carrying out experiments in LHD.

I would like to express my sincere gratitude to the CLASP team from National Astronomical Observatory of Japan for providing the optical components to carry out experiments in LHD. Without these components it would not have been possible to realize the polarization measurement system for LHD. Specially, I sincerely thank Prof. Ryouhei Kano for his kind help and guidance to carry out experiments for testing of the components at UVSOR facility.

My heartfelt thank goes to my colleagues, Dr. Guillaume Seguineaud, Trang Le, Dr. Yang Liu, Yuki Goto, Yasuaki Haba, Dr. Jie Huang, Takeru Ohgo, Dr. Bostz Huang, Neng Pu, and Bing Ma. I also express my thanks to Suphachok Buaruk from Thailand. I share many good memories and adventures with all of them.

I gratefully acknowledge the support and cooperation of Dr. Joydeep Ghosh, from Institute for Plasma Research (IPR) in India. It was his support that made it possible for me to join this doctoral program in Japan. I am very thankful to members of spectroscopy diagnostics group at IPR, Dr. Malay Bikas Chowduri, Ms. Ranjana Manchanda, Dr. Santanu Banerjee, Nandini Yadav, Abha Kanik, and Sharvil Patel. I started my journey of research in the field of plasma physics and nuclear fusion with them and learned many things from working with them. Also, I would like to express my sincere gratitude to Dr. Shwetang Pandya for his continuous guidance related to daily life in Japan and specially related to my research work. His guidance and suggestion have been tremendously helpful to me. My big thanks to Mrs. Bhavinee Pandya also for her many useful suggestions to start life in Japan.

In the end, I wish to express my gratitude to my family, my parents, grandparents, brothers, sisters-in-law, and my sweet little niece, Reeva. My family always supported me in every possible way and motivated me during this journey. Specially I am grateful to my elder brother, Yagnesh Ramaiya, for all the love and care he gave us and for always inspiring me to pursue higher education. Therefore, I humbly dedicate this thesis to him. My heartfelt thanks also goes to my Gurudev.

Contents

List of Figures

List of Tables

CHAPTER 1

Introduction

1.1 Thermonuclear fusion for clean energy

The continuous use of non-renewable energy sources causes the serious problem of energy crisis and therefore, modern society requires environmentally friendly solutions for energy production. Solar, wind, hydro, geothermal and other renewable sources of energy are widely popular throughout the world today. Although these sources provide a clean and safe option for energy production, each source has some limitations. For example, solar energy and wind energy strongly depends on the weather conditions. Nuclear fission is also one of the most popular energy sources at present. Nuclear fission power plants are safe, reliable, and cost-effective for electrical power production. Since this approach uses radioactive materials, management of the radioactive waste is a serious problem.

Energy can be released not only from the fission of heavy nuclei but also from the fusion of light nuclei. Thermonuclear fusion is one of the attractive energy sources because the output energy is controllable and management of the radioactive waste is much easier compared to the fission power plants. Considering

the cross-section of the fusion reactions [2], the most promising fusion reaction for the fusion reactor is:

$$D_1^2 + T_1^3 \rightarrow He_2^4\,(3.5\text{ MeV}) + n_0^1\,(14.1\text{ MeV}),$$

where D_1^2, T_1^3, He_2^4, and n_0^1 are the deuterium, tritium, α particle and neutron, respectively. In this reaction, neutron with a kinetic energy of 14.6 MeV leaves the plasma without any interaction with bulk particles, and can be used for the electric power generation. The α particle with kinetic energy of 3.5 MeV contributes to maintain the high-temperature plasma through collisions with bulk electrons and ions. In order to build a fusion reactor two conditions must be fulfilled:

- Heating the DT fuel to a temperature ~ 10 keV
- Confinement of the heated fuel long enough with sufficient pressure for a few percent of the fusion fuel to burn.

There are several approaches to confine the plasma [3], e.g., gravity, inertia [4], electromagnetic waves, magnetic fields [5]. At present, confining the plasma through magnetic fields is being extensively studied. The magnetic field lines for confining the plasma may be open or closed. The devices employing open magnetic field lines are known as linear devices and those with closed magnetic field lines are known as toroidal devices. A magnetic mirror machine is an example of a linear device. Due to rapid particle loss along the magnetic field lines, a magnetic mirror machine can not achieve an adequate power gain. Hence, such devices are not suitable as a nuclear fusion reactor.

The main types of magnetic confinement fusion experiments are tokamaks and stellarators, which are toroidal devices. Over past several decades, many toroidal devices have been built, namely, the Joint European Torus (JET) in UK, DIII-D [6] and TFTR in USA, JT-60U [7] and the Large Helical Device (LHD) [8] in Japan, and the Wendelstein 7-X (W7-X) [9] in Germany. The ITER (International Thermonuclear Experimental Reactor) [10] in France is under construction.

1.2 Importance of studying anisotropic electron velocity distribution function

The electron velocity distribution function (EVDF) in a plasma is one of the most important attributes of the plasma. In many cases the EVDF is assumed to be isotropic without any experimental or theoretical verification. EVDF may show significant anisotropy due to several reasons, e.g., in presence of electromagnetic wave heating, the variation in magnetic field strength. For clear understanding of plasma confinement and transport phenomena in a magnetically confined plasma, the measurement of anisotropy in the EVDF is necessary. In spite of the fact that the anisotropic EVDF plays an important role in a plasma, there is a lack of studies focused on it in plasma experiments.

In LHD a decrease in the electron density was observed during high-power heating, particularly in the presence of electron cyclotron heating (ECRH) [11], indicating that the EVDF becomes anisotropic during ECRH. Yamaguchi et al. proposed and verified a method to obtain the ratio of parallel and perpendicular stored energies using magnetic measurement [12, 13] with the main objective of investigating the anisotropic pressure in the LHD plasma. They employed dia- magnetic coils and saddle coils for evaluating anisotropic stored energy. The equilibrium of anisotropic plasmas has been investigated theoretically since last many years. At the Joint European Torus (JET) and Tore Supra, plasma equilibrium was investigated in the presence of high auxiliary power, and results show unphysical equilibria when assuming isotropic pressure [14]. Some diagnostics techniques, e.g., electrical probes [15, 16], a directional energy analyzer [17], Thomson scattering [18, 19], absorption of waves [20, 21] and polarization in emission lines of atoms or ions [1], have been investigated earlier to study the anisotropic EVDF.

From electron beam impact experiments and theoretical calculations it is well known that anisotropic electron-impact excitation creates non-uniform

population distribution of excited magnetic sublevels and the subsequent emission is polarized. Thus, plasma polarization spectroscopy provides a possibility to study anisotropy in the EVDF. The advantage of this method is that it is a non-perturbative method. In many applications, investigating plasma with a non-perturbative diagnostics method is preferred. Contrary to probes, spectroscopic measurements are not affected by RF or microwave field and also they do not contaminate the plasma. This thesis work is mainly focused on studying anisotropy in the EVDF with the polarization spectroscopy.

1.3 Introduction to polarization spectroscopy

Plasma spectroscopy is one of the disciplines in plasma physics in which a spectrum of radiation emitted from a plasma is observed and its features are interpreted in terms of the properties of the plasma. In conventional plasma spectroscopy, mainly line intensities, broadening, and shift of spectral lines are observed. From such observations the information regarding plasma parameters such as electron temperature and density, whether it is ionizing or recombining plasma can be obtained. The ability of plasma spectroscopy can be expanded by incorporating the polarization characteristics of the radiation in framework. Investigating polarization of radiation gives information of how atoms or ions were excited in the plasma. The term "Plasma Polarization Spectroscopy" was first introduced by Kazantsev et al. [22].

Emission lines and continua can be polarized because of the anisotropy of the plasma. This anisotropy may be due to anisotropic collisional excitation or due to an external field, electric or magnetic [1]. The polarization phenomena are mainly divided into three classes:

Class 1: This class contains polarization phenomena due to an electric or a magnetic field. When an atom is placed in an external electric field or a magnetic field it is subjected to the Stark effect or the Zeeman effect and therefore a spectral

line splits into several components and each of the components is polarized. When all the components are added together, the line is overall unpolarized. These phenomena are known for a long time and the formulation of these effects is well established. Experiments have been carried out to determine the poloidal field in the tokamak plasmas using the Zeeman-split lines. Detection of a Motional Stark effect can give information about a magnetic field.

Class 2: In this class of polarization phenomena, an external field is absent. Atoms are subjected to anisotropic excitation such as the directional electron collisions, photo-excitation by a laser beam, reabsorption of radiation in an anisotropic geometry, and so on. For the first anisotropy, the key is the anisotropic velocity distribution of plasma electrons that excite the atoms. By investigating polarization in emission lines originated due to collisions with electrons having anisotropic velocity distribution, it is possible to deduce the shape of EVDF of the plasma in the velocity space. The presence of a weak magnetic field would make the produced atomic anisotropy rotate around the field direction, or it even defines the local axis of axial symmetry.

Class 3: This is the combination of Class 1 and Class 2. Anisotropic excitation under an electric field or a magnetic field, or even both of them. This class is very difficult to treat, however, this class can be explored with the help of plasma diagnostics such as z-pinch plasmas.

In this thesis work, we are mainly concerned with the polarization phenomena of class 2 caused by the spatial anisotropy in the velocity distribution of the colliding electrons. The main objective of present research is to investigate the polarization in Lyman-α line from the edge LHD plasma due to the anisotropic electron collisions and to obtain information regarding anisotropy in the EVDF.

1.4 Stokes parameters

A standard way of specifying the state of polarization of a light beam is to use the Stokes parameters. The stokes parameters have the advantage of being real quantities that can be directly related to detectable signals of polarization measurements. Considering a situation in which a beam of light emitted by an ensemble of atoms at a large distance is observed. It is assumed here that the light is plane parallel and propagating in the $+z$-direction. If the ensemble of atoms is rotated by a certain angle; the emitted light is virtually a plane parallel light beam propagating in the $+z$-direction. Here, a linear polarizer and two circular polarizers have been used in front of detector to measure the intensity of the beam. Two circular polarizers are employed to detect right-circularly and left-circularly polarized light, respectively. The observed intensity is denoted as I_θ or I_r or I_l, where I_θ is the intensity observed with the linear polarized with its transmission axis making angle θ with respect to the $x-$axis. I_r and I_l represents right-circularly and left-circularly polarized light, respectively. The Stokes parameters are defined as

$$
\begin{aligned}
I &= I_0 + I_{\pi/2} = I_{\pi/4} + I_{3\pi/4} = I_\mathrm{r} + I_\mathrm{l} \\
Q &= I_0 - I_{\pi/2} \\
U &= I_{\pi/4} - I_{3\pi/4} \\
V &= I_\mathrm{r} - I_\mathrm{l}.
\end{aligned}
$$

It may be shown that, $Q^2 + U^2 + V^2 \leq I^2$.
The degree of polarization of the light beam is defined as

$$P = \frac{\sqrt{Q^2 + U^2 + V^2}}{I}.$$

For unpolarized light, the parameters are given as

$$I, \quad Q = U = V = 0.$$

1.5 Polarization spectroscopy in astrophysics

Plasma polarization spectroscopy is a very useful tool to study the anisotropic properties of a plasma. This technique can be employed for investigating not only magnetically confined plasmas but also astrophysical plasmas. Solar physics has been pioneering in exploiting polarization information contained in the radiation coming from the Sun to understand solar magnetism. Magnetic field strengths in the solar atmosphere range from the very weak field of the order $B \leq 10^{-3}\,\mathrm{T}$ to the strong fields of the order $B \geq 10^{-1}\,\mathrm{T}$. Because of such diverse regimes of magnetic field, different phenomena affecting the polarization of the emitted radiation can occur in solar plasmas, e.g., Zeeman effect, Hanle effect, alignment-to-orientation conversion, which can be investigated to infer the magnetic topology of the emitting plasma.

1.5.1 Chromospheric Lyman-Alpha Spectro-Polarimeter

In astrophysics spectro-polarimetric observations in the vacuum-ultraviolet range of wavelength are emerging as a new diagnostic tool for high-temperature plasmas. In particular the hydrogen Lyman-α line at 121.57 nm is considered to be the most suitable line for this purpose because it is the brightest line in the VUV range which is emitted from the upper solar chromosphere and the transition region and the most importantly the Hanle effect on this line is sensitive to the magnetic field strengths expected in the upper chromosphere.

With the aim of measuring the linear polarization of the Lyman-α line and to explore the magnetism of the solar chromosphere and transition region for the first time, the high-throughput Chromospheric Lyman-Alpha Spectro-Polarimeter (CLASP) [23] was developed. In the development of CLASP researchers from Japan, the USA, Spain, France, and Norway were involved and it was launched with NASA's sounding rocket. The CLASP consists of a Cassegrain telescope, a spectropolarimeter, and a slit-jaw optical system.

The CLASP spectropolarimeter consists of a rotating half-waveplate, two polarization analyzers, two camera mirrors, and a grating. These components have been specially designed for Lyman-α line. In the present experiments in LHD, the polarization measurement system uses the half-waveplate [24], the polarization analyzer, and the mirror [25] provided by the CLASP team.

1.6 Introduction to the Large Helical Device

Figure 1.1 shows schematic drawing of the main of the LHD [8]. The Large Helical

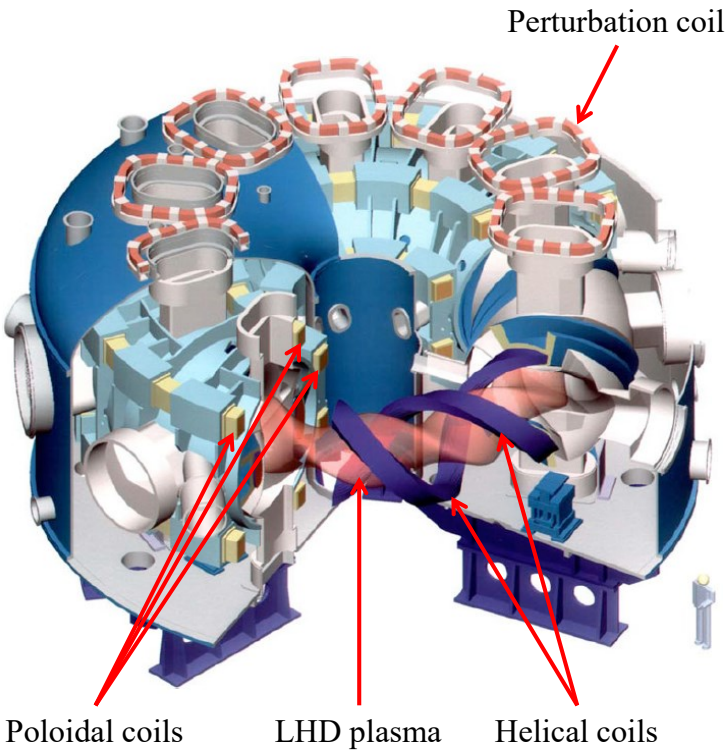

Fig. 1.1: A bird's-eye view of LHD

Device (LHD) is heliotron-type magnetic confinement fusion experimental device, which employs large-scale superconducting magnets and enables advanced studies on net-current-free plasmas [8, 26]. The main goal of the LHD experiments is to demonstrate the high performance of helical plasmas in a reactor-relevant plasma regime.

The LHD makes use of a pair of superconducting helical coils with $l/m = 2/10$, to generate the rotational transform and magnetic shear. Here l is the number of the polarity of the helical coils and m is the toroidal field period. Three sets of superconducting poloidal coils control the position of the plasma column, especially, the magnetic axis, the elongation, and the poloidal flux. Additionally, 10 pairs of perturbation coils are also set up at the top and bottom of the main body to generate a major resonant magnetic field with $m/n = 1/1$ or $2/1$.

Heating facilities available in LHD

In LHD to initiate and sustain the plasma three different heating methods, namely, neutral beam injection (NBI) [27], ion cyclotron resonant frequency (ICRF) heating [28], and electron cyclotron resonance heating (ECRH) [29], are used. Figure 1.2 shows top view of the arrangement of heating facilities available in LHD [8].

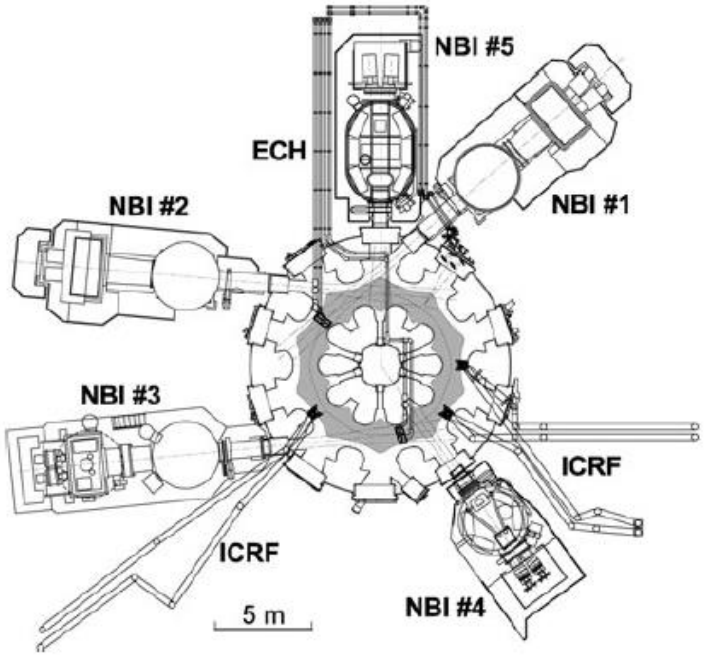

Fig. 1.2: Top view of the arrangement of heating facilities in LHD

The NBI system consists of three negative-ion-source based NBI beams (n-NBI) with energy of 180 keV and two positive-ion-source based NBI beams (p-NBI) with energy of 40 keV. The n-NBI mainly heats bulk electrons and is generally used for maintaining short pulse discharges in wide plasma and discharge parameter ranges, whereas the p-NBI is specially used for heating bulk ions in low-density plasma discharges. In LHD, an ECRH system has been operated for preionization and plasma heating and it consists of eight gyrotrons with frequencies 77 GHz, 82.7 GHz, 84 GHz, and 154 GHz [29, 30]. The total injection power of ECRH to the plasma is ~ 4 MW.

Main parameters of LHD

The main parameters of LHD are listed in Table 1.1.

Major radius (R)	$3.5 - 4.2$ m
Minor radius (a)	$0.50 - 0.65$ m
Plasma volume (V_{p})	$20 - 30\,\mathrm{m}^3$
Magnetic field (B_{t})	< 3 T
ECRH power (P_{ECRH})	4 MW
ICRF power (P_{ICRF})	2 MW
Total NBI power (P_{NBI})	28 MW
Central electron temperature (T_{e0})	20 keV
Central ion temperature (T_{i0})	10 keV
Central electron density (n_{e0})	$1 \times 10^{18} - 1 \times 10^{21}\,\mathrm{m}^{-3}$

Tab. 1.1: Main parameters of LHD

1.7 Objective and structure of the thesis

The main objective of this thesis work to evaluate the anisotropy in the EVDF using polarization spectroscopy. By incorporating the optical components provided by the CLASP (Chromospheric Lyman-Alpha Spectro-Polarimeter) team, polarization-resolved measurements of Lyman-α have been realized in LHD. We have designed and developed an optical system to measure the polarization of Lyman-α line coming from the edge LHD plasma.

To derive anisotropy in the EVDF from the measured polarization degree, a theoretical model known as the Population-Alignment Collisional-Radiative (PACR) model is required. The quantity alignment is a measure of population imbalance among the magnetic sublevels in a state. The PACR model is extension of the Collisional-Radiative model in which besides the population, the alignment of the level is also treated.

This thesis work is mainly divided into two parts:

1. Measurement of polarization in Lyman-α line from the edge LHD plasma
2. Development of the PACR model for Lyman-α line.

The structure of the thesis is as following:

- In chapter 1 we have described the importance of studying anisotropy in the EVDF along with the short introduction of LHD.
- In chapter 2 the collisional-radiative model is given briefly. We have made collisional radiative calculations concerning level $p = 2$ of hydrogen with the main goal to investigate the dominant populating and depopulating processes of this level. The details of the calculations have been also presented in this chapter.
- In chapter 3 the theoretical framework for the PACR model is described. We have developed the PACR model for the Lyman-α line and details are presented in chapter 4.

- The polarization measurement system on LHD is presented in chapter 5 with the details of each individual component used in the system. Also, the evaluation of polarization degree from the measured data is explained in the chapter.
- In chapter 6 the results of the present work have been shown in details and finally in chapter 7 summary and conclusion is given.

CHAPTER 2

Collisional-Radiative Calculations

The main objective of this thesis work is to evaluate anisotropy in the electron velocity distribution function (EVDF) from experimentally measured polarization degree in the Lyman-α line at 121.57 nm from the edge LHD plasma. To achieve this goal, development of a theoretical model known as "the Population-Alignment Collisional-Radiative (PACR) model" is absolutely necessary.

As shown in Fig. 2.1 Lyman-α line is emitted due to radiative transitions $1\,^2S_{1/2} - 2\,^2P_{3/2}$ and $1\,^2S_{1/2} - 2\,^2P_{1/2}$ at wavelengths 121.5668 nm and 121.5673 nm, respectively. Since intensity of the emitted Lyman-α line depends on the population of 2P state of hydrogen atoms, for constructing the PACR model knowing the dominant processes responsible for populating and depopulating the 2P state is prerequisite. On the basis of this knowledge rate equations for the population and alignment are constructed in the PACR model.

The Collisional-Radiative model is a versatile tool in dealing with a problem of population. In this chapter, the theoretical framework for the Collisional-Radiative model is described briefly which is based on Ref. [1, 31]. We have carried out collisional-radiative calculations to investigate the contribution of different

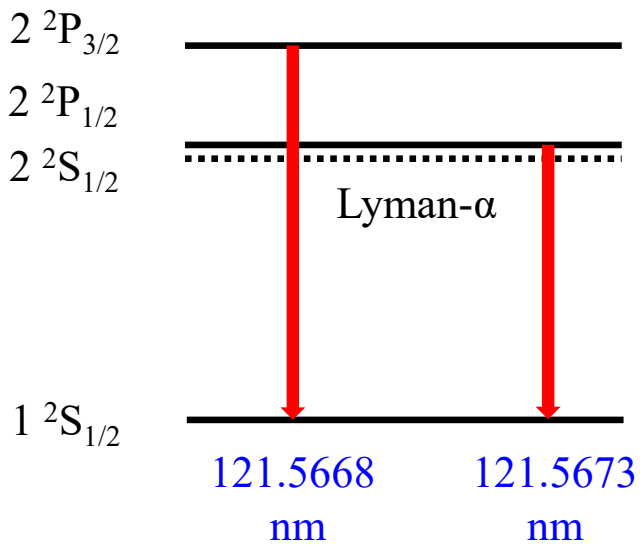

Fig. 2.1: Lyman-α line transitions

processes in populating and depopulating the 2P state of hydrogen. Initially the calculations have been made by considering only n levels, where n is the principal quantum number, and later fine structure levels of the $n = 2$ level have been taken into account. The population of a level is a function of electron density and electron temperature. The present measurements have been made for the Lyman-α line emitted from the edge LHD plasma and therefore, for these calculations typical plasma parameters of the edge LHD plasma have been borne in mind and results are presented in this chapter.

2.1 Collisional-Radiative Model

Figure 2.2 shows a schematic energy-level diagram of an atom or an ion. The populations of level p and r in the ionization stage $(z-1)$ are of main interest. z is the charge state of the next ionization-stage ions. The level $p = 1$ means the ground state. $E_{z-1}(p,r)$ and $\chi_{z-1}(p)$ stand for the energy difference between levels p and r and the ionization potential of p, respectively. The population of level p is denoted as $n_{z-1}(p)$ and the statistical weight as $g_{z-1}(p)$.

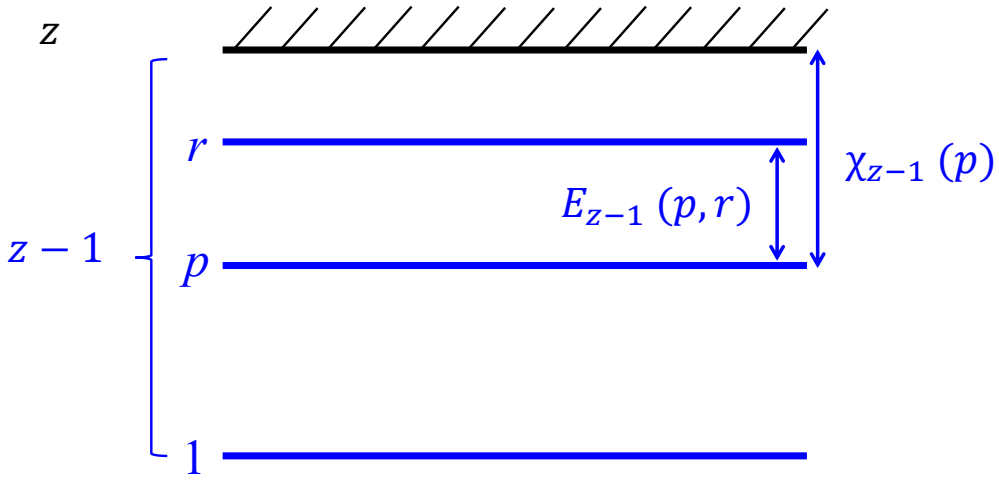

Fig. 2.2: Energy-level diagram

The transition processes considered for developing the model are shown in Fig. 2.3. $A(r,p)$ is the spontaneous transition probability in units of s^{-1}.

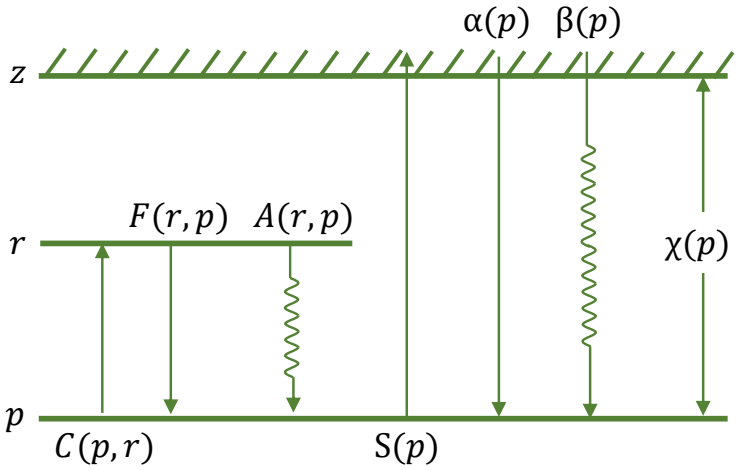

Fig. 2.3: Atomic processes taken into account for developing collisional-radiative model

Table 2.1 shows the various atomic processes and corresponding rate coefficients with units.

Atomic process	**Rate coefficient**
Electron impact excitation from level p to r	$C(p,r)$ $[\mathrm{m^3 s^{-1}}]$
Electron impact deexcitation from level r to p	$F(r,p)$ $[\mathrm{m^3 s^{-1}}]$
Ionization from level p	$S(p)$ $[\mathrm{m^3 s^{-1}}]$
Radiative recombination into level p	$\beta(p)$ $[\mathrm{m^3 s^{-1}}]$
Three-body recombination into level p	$\alpha(p)$ $[\mathrm{m^6 s^{-1}}]$

Tab. 2.1: Atomic processes and rate coefficients

2.1.1 Rate equation for the population

Here the plasma is assumed to be optically thin and having a thermal electron velocity distribution function, i.e., the Maxwell distribution. The electron temperature and density are denoted by T_e and n_e, respectively. For a level p, the rate equation which describes the temporal development of the population in the plasma can be written as

$$\begin{aligned}\frac{\mathrm{d}}{\mathrm{d}t}n(p) = &\sum_{r<p} C(r,p) n_\mathrm{e} n(r) \\ &- \left[\sum_{r<p} A(p,r) + \left\{\sum_{r<p} F(p,r) + \sum_{r>p} C(p,r) + S(p)\right\} n_\mathrm{e}\right] n(p) \\ &+ \sum_{r>p} [A(r,p) + F(r,p) n_\mathrm{e}] n(r) \\ &+ [\beta(p) + \alpha(p) n_\mathrm{e}] n_\mathrm{e} n_z .\end{aligned} \tag{2.1}$$

In above equation, $r < p$ means that level r lies energetically below level p, and a summation sign with $r < p$ means the summation over level r lying below level p, which is under consideration. $r > p$ indicates that level r is energetically higher

than level p. The quantities like $C(r,p)n_e$ or $A(p,r)$, having units of s^{-1} are known as "the rate" or "the probability", and those like $C(r,p)n_e n(r)$ or $A(p,r)n(p)$, having units of $m^{-3}s^{-1}$, are known as "the flux".

The first line represents the excitation flux by electron impact from lower-lying levels including the ground state. The third line represents the populating flux, collisional and radiative, from higher-lying levels, whereas the fourth line is the populating flux by direct recombination. The second line is the total depopulating flux from this level, which includes depopulation due to collisional excitation to higher levels, collisional deexcitation to lower level, radiative decay to lower levels, and ionization.

2.1.2 Introducing the concept of Quasi Steady-State approximation

Although the rate equations could be solved numerically, a problem remains of how many levels should be included in the set of equations. An alternative approach has been proposed by Fujimoto [1, 31], which is more general though approximate and it has been found that in the majority of practical problems, this method gives quite accurate results.

For the purpose of illustrating this method, neutral hydrogen or hydrogen-like ions have been considered. In this case, p or r is understood to represent the principal quantum number of the level. The relaxation time $t_{rl}(p)$ for $n(p)$ from Eq. (2.1) is defined as

$$t_{rl}(p) = \left[\sum_{r<p} A(p,r) + \left\{ \sum_{r<p} F(p,r) + \sum_{r>p} C(p,r) + S(p) \right\} n_e \right]^{-1}. \tag{2.2}$$

This quantity is a measure of the time constant in which this population, $n(p)$, reaches its stationary-state value provided that the populating flux into this level is constant. Equation (2.2) indicates that, at low plasma densities, the relaxation

time is determined by the radiative decay rate or the natural lifetime, while at high densities, it is given by the collisional depopulation rate.

From Eq. (2.2) the approximate relaxation time of the ground-state population may be given as

$$t_{\mathrm{rl}}(1) \simeq [S(1)n_{\mathrm{e}}]^{-1}. \tag{2.3}$$

The ion density n_z has a similar relaxation time under normal conditions. It can be concluded that in many practical cases

$$t_{\mathrm{rl}}(p) << t_{\mathrm{rl}}(1) \quad \text{for} \quad p \geq 2 \tag{2.4}$$

is valid. It is also expected that the total number of populations in excited levels is much smaller than the sum of the ground-state population and the ion density.

$$\sum_{p\geq 2} n_{z-1}(p) << [n_{z-1}(1) + n_z]. \tag{2.5}$$

It has been found that Eq. (2.4) and Eq. (2.5) are well satisfied, except for very extreme cases.

Eq. (2.4) and Eq. (2.5) indicate that unless $n(1)$ or n_z, and/or plasma parameters undergo a very rapid change, it can be expected that at a certain time the excited-level populations have already reached their stationary-state values that are given by $n_{z-1}(1)$ and n_z, as well as by T_{e} and n_{e}, at that instance. This situation is called "the quasi-steady state (QSS)".

2.1.3 Defining the Recombining plasma component and the Ionizing plasma component

The above mentioned considerations imply that, in the coupled rate equations Eq. (2.1), the time derivative of the excited-level populations may be approximated to

zero:

$$\frac{\mathrm{d}}{\mathrm{d}t}n(p) = 0 \quad \text{for} \quad p = 2, 3, \ldots, \tag{2.6}$$

while the time derivative should be retained for the ground-state population $n_{z-1}(1)$ and the ion density n_z.

The problem of population can be formulated as follows. The system is divided into two subsystems:

1. the populations of the whole excited levels
2. the ground-state population and the ion density.

The set of coupled linear equations, Eq. (2.1) with Eq. (2.6), for the first subsystem can be expressed in the matrix form

$$\begin{pmatrix} \cdots \\ \cdots \\ \cdots \\ \cdots \end{pmatrix} \begin{pmatrix} n(2) \\ \cdot \\ n(p) \\ \cdot \end{pmatrix} = \begin{pmatrix} \cdot \\ \cdot \\ \cdot \\ \cdot \end{pmatrix} n(1) + \begin{pmatrix} \cdot \\ \cdot \\ \cdot \\ \cdot \end{pmatrix} n_z. \tag{2.7}$$

The dimension of the matrix, or the number of levels, should be limited at some appropriate values. The elements of the square matrix on the left-hand side and the column matrices on the right-hand side are terms on the right-side of Eq. (2.1) and are functions of T_e through the collisional rate coefficients and of n_e. It is obvious from the structure of Eq. (2.7) that this equation is readily solved for $p \geq 2$ as a sum of two terms, each of which is proportional to $n(1)$ and n_z, respectively. The solution of $n(p)$ can be assumed of following form:

$$\begin{aligned} n(p) &= R_0(p) n_z n_\mathrm{e} + R_1(p) n(1) n_\mathrm{e} \\ &\equiv n_0(p) + n_1(p). \end{aligned} \tag{2.8}$$

Equation (2.8) shows that an excited-level population is the sum of the two components; the first component being proportional to the ion density n_z and the second to the ground-state atom density $n(1)$. These components of populations

are termed as "the recombining plasma component" and "the ionizing plasma component", respectively. Figure 2.4 schematically shows this situation.

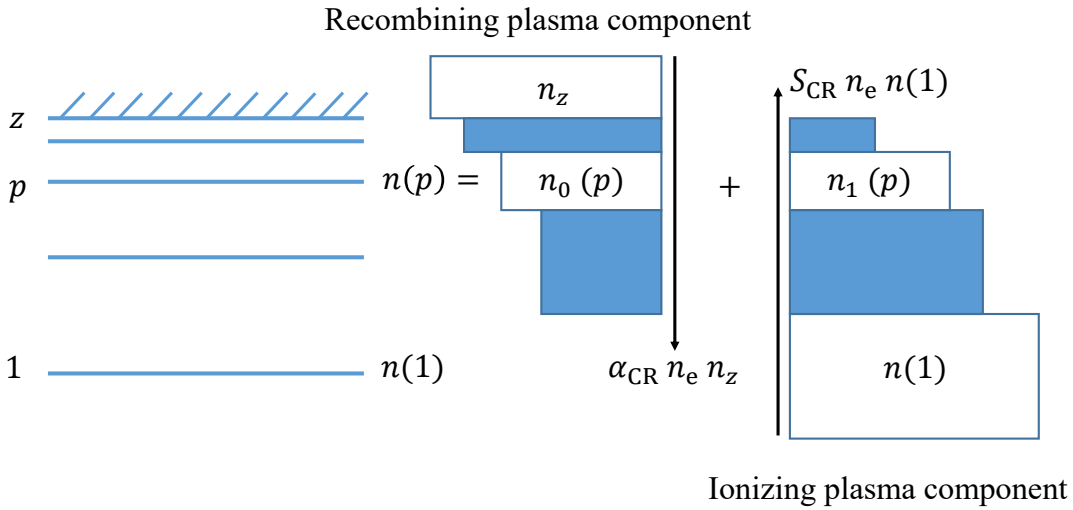

Fig. 2.4: Structure of the excited-level populations in the Collisional-Radiative model [1]

By substituting Eq. (2.8) into the coupled linear equations Eq. (2.7), two sets of coupled equations are obtained, one for $R_0(p)$ and another for $R_1(p)$. The solutions of $R_0(p)$ and $R_1(p)$ are called "the population coefficients" and they are functions of T_e and n_e. The theoretical framework described above is called "the collisional-radiative (CR) model".

Equation (2.8) shows the solutions for the excited-level populations and by substituting these values in Eq. (2.1), for $p = 1$ Eq. (2.1) reduces to

$$\begin{aligned}\frac{\mathrm{d}}{\mathrm{d}t}n(1) = &-\left[\sum_{r\geq 2} C(1,r) + S(1)\right] n_\mathrm{e} n(1) \\ &+ \sum_{r\geq 2}[A(r,1) + F(r,1)n_\mathrm{e}]\,[R_0(r)n_z + R_1(r)n(1)]n_\mathrm{e} \\ &+ [\beta(1) + \alpha(1)n_\mathrm{e}]n_z n_\mathrm{e}.\end{aligned} \tag{2.9}$$

With

$$S_{\mathrm{CR}} = \sum_{r\geq 2} C(1,r) + S(1) - \sum_{r\geq 2} R_1(r)[F(r,1)n_{\mathrm{e}} + A(r,1)], \tag{2.10}$$

$$\alpha_{CR} = \alpha(1)n_{\mathrm{e}} + \beta(1) + \sum_{r\geq 2} R_0(r)[F(r,1)n_{\mathrm{e}} + A(r,1)] \tag{2.11}$$

Eq. (2.9) can be rewritten as

$$\frac{\mathrm{d}}{\mathrm{dt}} n(1) = -S_{\mathrm{CR}}\, n(1)\, n_{\mathrm{e}} + \alpha_{CR}\, n_z\, n_{\mathrm{e}}. \tag{2.12}$$

S_{CR} and α_{CR} are called the collisional-radiative (CR) ionization rate coefficient and CR recombination rate coefficient, respectively and they are functions of n_{e} and T_{e}.

2.2 Collisional-Radiative calculations for $p = 2$ level of hydrogen

We have made collisional-radiative calculations concerning level $p = 2$ of hydrogen using the collisional-radiative model code provided by Sawada [32]. The aim of this study is to investigate the dominant processes responsible for populating and depopulating the level $p = 2$ by considering the edge LHD plasma conditions. T_{e}, and n_{e} of the edge LHD plasma, where Lyman-α is emitted, are approximately in the range 10 eV–30 eV and $10^{18}\,\mathrm{m}^{-3}$–$10^{19}\,\mathrm{m}^{-3}$, respectively. In present case, for $p = 2$ level, the population is mainly determined by collisional and radiative transitions. The contribution of recombining transitions, three-body recombination and radiative recombination, in populating this level is negligible. In other words, the ionizing plasma component of population is dominant, hence for this calculation only the ionizing plasma component is considered.

Figure 2.5 shows processes considered in the calculation.

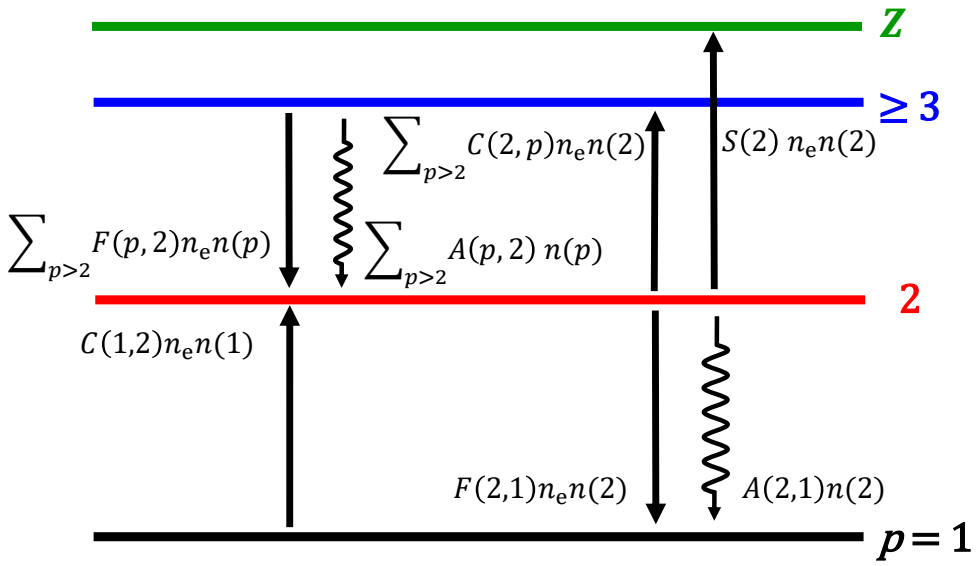

Fig. 2.5: Transition processes considered for Collisional-Radiative calculations relating to level $p = 2$

The rate equation for level $p = 2$ can be written as

$$\begin{aligned}\frac{\mathrm{d}}{\mathrm{d}t}n(2) \; &= C(1,2)n_e n(1) + \sum_{r>2}\Big\{A(r,2) + F(r,2)n_e\Big\}n(r) \\ &- \left[A(2,1) + \left\{F(2,1) + \sum_{r>2} C(2,r) + S(2)\right\}n_e\right]n(2).\end{aligned} \tag{2.13}$$

The first line represents populating fluxes into level $p = 2$, collisional and radiative both, while the second line represents depopulating fluxes from the level.

The rate coefficients, transition probabilities and population of levels have been obtained using the collisional-radiative model code provided by Sawada [32] and using these values populating and depopulating fluxes have been evaluated.

2.2.1 Populating fluxes into level $p = 2$

Figure 2.6 shows the breakdown of populating fluxes concerning level $p = 2$ into individual fluxes. The result is valid for T_e in the range from 10 eV to 30 eV. The blank area in the figure represents collisional transition and the hatched area

represents radiative transition, while numerals indicate the principal quantum number of the level from which the transition originates. The shaded area shows n_e range from $10^{18}\,m^{-3}$ to $10^{19}\,m^{-3}$, which is the typical range of electron density in the region of our interest. The values are normalized by the total populating flux.

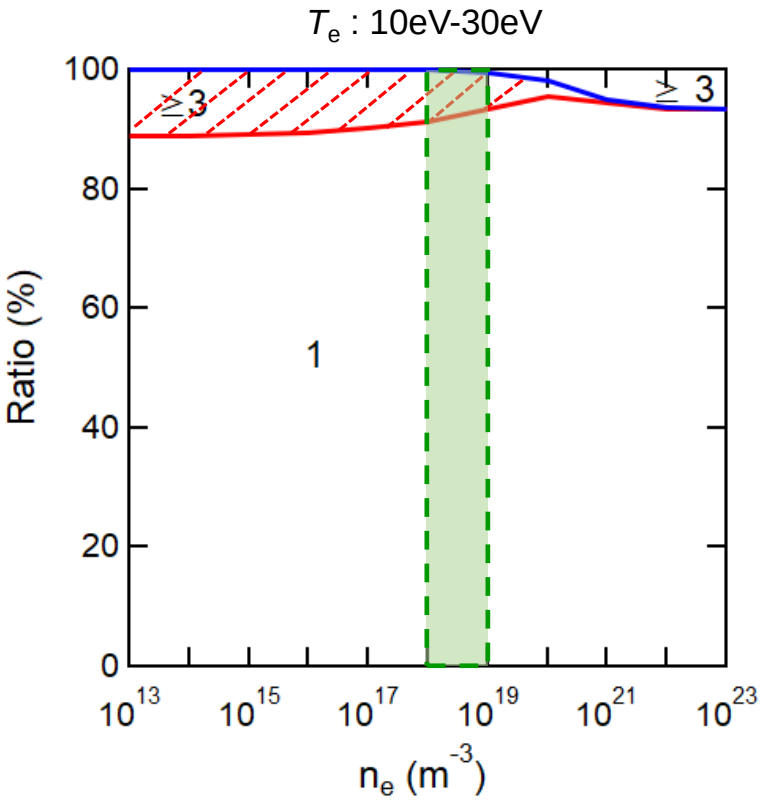

Fig. 2.6: Breakdown of populating processes concerning level $p = 2$ into individual fluxes

The result indicates that:

- For the n_e range $10^{13}\,m^{-3}$ to $10^{23}\,m^{-3}$, more than 90% of the populating flux into the level is due to the electron-impact excitation from the ground state.
- For n_e values lower than $10^{18}\,m^{-3}$, approximately 10% contribution comes from the radiative decay from the higher energy levels.
- In the high density range contribution due to the radiative decay from the higher energy levels becomes almost zero and instead there is about 10% populating flux due to collisional deexcitation from the higher energy levels.

- Electron-impact excitation from the ground state remains the dominant process in populating the level.

2.2.2 Depopulating fluxes from level $p = 2$

Figure 2.7 shows the breakdown of depopulating fluxes concerning level $p = 2$ into individual fluxes.

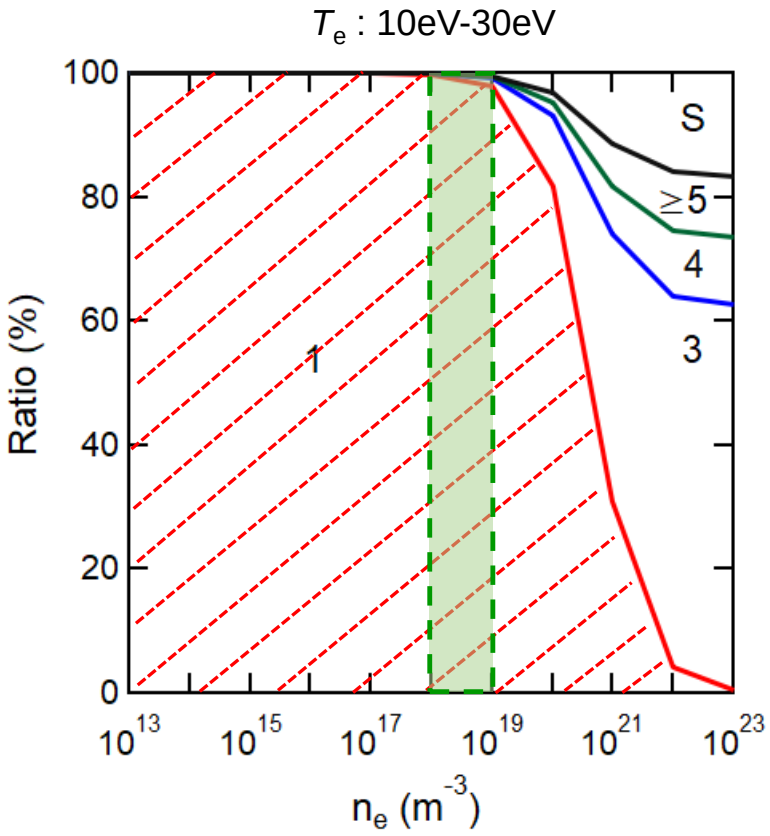

Fig. 2.7: Breakdown of depopulating processes concerning level $p = 2$ into individual fluxes

The result is also valid for T_e in the range from 10 eV to 30 eV. The blank area in the figure represents collisional transition and the hatched area represents radiative transition, while numerals indicate the principal quantum number of the level on which the transition terminates. The shaded area shows n_e range from $10^{18}\,\mathrm{m}^{-3}$ to $10^{19}\,\mathrm{m}^{-3}$, which is the typical range of electron density in the region

of interest. The values are normalized by the total depopulating flux. The result shows that:

- For the n_e range from $10^{13}\,m^{-3}$ to $10^{19}\,m^{-3}$ almost 100% depopulation of the level is due to radiative decay to the ground state.
- In the high density range collisional transitions dominate over radiative transitions and dominant depopulating fluxes are the collisional excitation to higher energy levels.
- Within the n_e range of interest, radiative decay to the ground state is the main depopulating process.

2.3 Influence of 2S − 2P transition in populating 2P state

The results presented in Sec. 2.2 are obtained considering main energy levels and the fine structure of levels is not taken into account. In addition to populating flux from the ground state, it is also necessary to examine the contribution of electron-impact excitation from the 2S state to 2P state in populating 2P state.

The populating flux into the 2P state due to 1S−2P and 2S−2P transitions, respectively, is expressed as

$$\mathrm{Flux}_{1S-2P} = C(1S, 2P)\, n_e\, n(1) \tag{2.14}$$

$$\mathrm{Flux}_{2S-2P} = C(2S, 2P)\, n_e\, n(2S). \tag{2.15}$$

Here, n_e is electron density, $C(1S, 2P)$ and $C(2S, 2P)$ are excitation rate coefficients for 1S−2P and 2S−2P transitions, respectively. $n(1)$ and $n(2S)$ represent populations of the ground state and 2S state, respectively.

The excitation rate coefficient for a transition $p - q$ assuming Maxwell distribution is defined as

$$C(p, q) = \int_{E_{thr}}^{\infty} \sigma_{p,q}(E)\, f(E)\, v\, \mathrm{d}E, \tag{2.16}$$

where $f(E)$ is Maxwell distribution function, $E_{\rm thr}$ is the energy difference between levels p and q, $\sigma_{p,q}(E)$ is the excitation cross section for the $p-q$ transition and v is the velocity of electron. The cross sections for electron-impact excitation concerning transitions 1S − 2P and 2S − 2P have been obtained from Refs. [33] and [34], respectively, and are shown in Fig. 2.8 (a). The rate coefficients for both the transitions are given in Fig. 2.8 (b) as a function of energy and are obtained from Ref. [34].

The present investigation has been done for $T_{\rm e} = 10\,{\rm eV}$, an approximate value at the region of Lyman-α emission in the LHD plasma. The Maxwell distribution curve for this $T_{\rm e}$ is also given in Fig. 2.8 (a). We have evaluated the populating flux into 2P state due to 1S − 2P and 2S − 2P transitions by taking the ground state population $n(1) = 1\,{\rm m}^{-3}$. The population of 2S state, $n(2{\rm S})$, is obtained from the collisional-radiative model code.

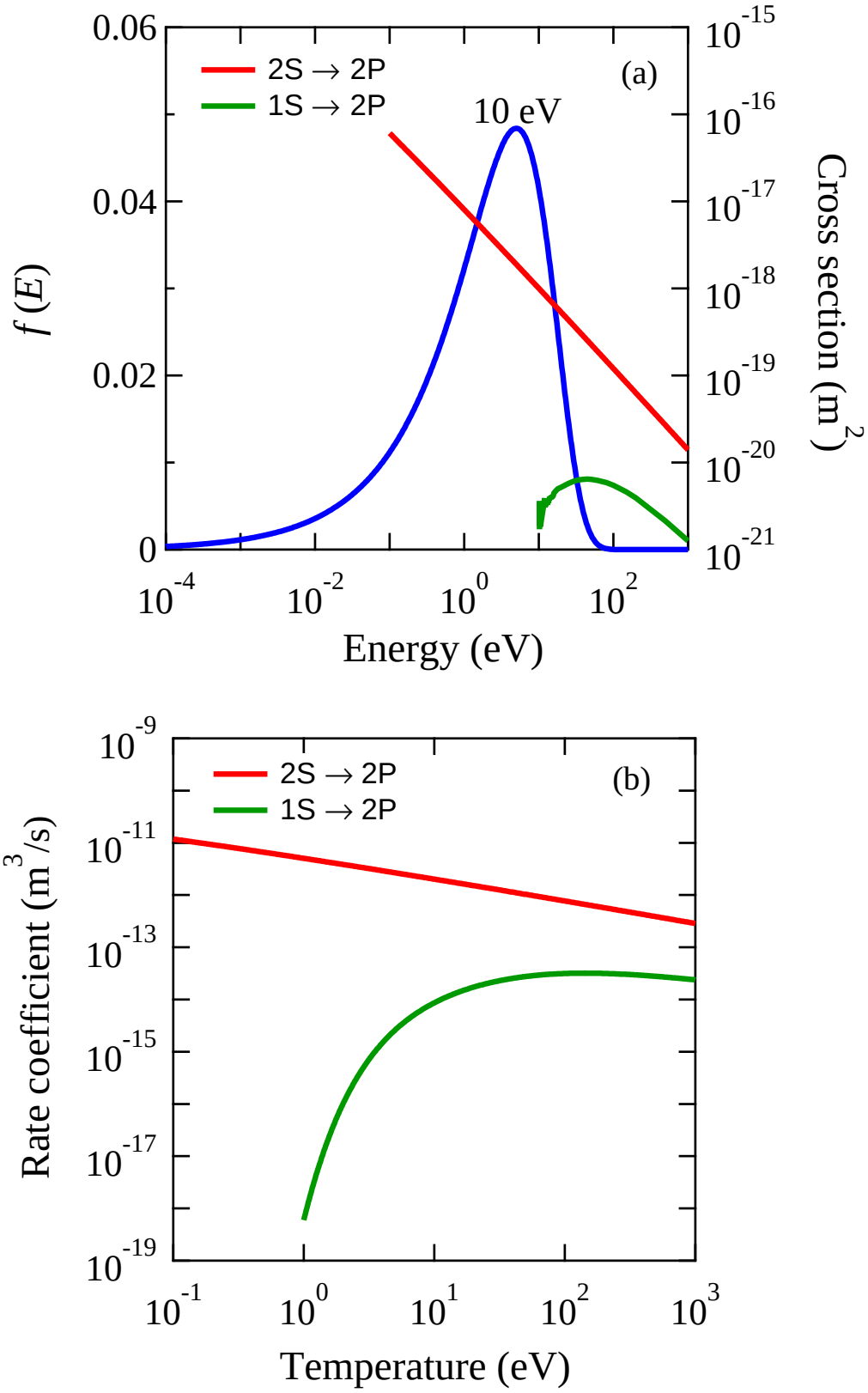

Fig. 2.8: (a) Cross sections for $1S-2P$ and $2S-2P$ transitions with Maxwell distribution curve at $T_e = 10\,eV$ (b) rate coefficients for both the transitions as a function of T_e

The obtained values of populating flux are shown in Tab. 2.2.

n_e in m^{-3}	Flux 2S → 2P [$m^{-3}s^{-1}$]	Flux 1S → 2P [$m^{-3}s^{-1}$]	Ratio
1.0×10^{18}	1.34×10^{1}	8.62×10^{3}	1.55×10^{-3}
1.0×10^{19}	1.28×10^{3}	8.62×10^{4}	1.49×10^{-2}

Tab. 2.2: Comparison of populating flux into 2P state due to 1P − 2P and 2S − 2P transitions

The evaluated fluxes suggest that for the n_e range of interest, $10^{18}\,m^{-3}$ to $10^{19}\,m^{-3}$, the populating flux into 2P state due to 1S − 2P transition is much higher and therefore, the contribution from 2S − 2P transition can be neglected.

2.4 Influence of 2P − 2S transition in depopulating 2P state

In addition to radiative transition 2P − 1S in depopulating 2P state it is also important to investigate the contribution of 2P − 2S transition due to collisional deexcitation. For this purpose the depopulating fluxes due to both the transitions needs to calculated.

By using the Klein-Rosseland relationship [31], it can be seen that the deexcitation rate coefficient for a transition $q - p$, $F(q,p)$, is related with the excitation rate coefficient for a transition $p - q$, $C(p,q)$ as

$$F(q,p) = \frac{g(p)}{g(q)} \exp\left[\frac{E(p,q)}{kT_e}\right] C(p,q), \tag{2.17}$$

where $E(p,q)$ is the energy difference between levels p and q, kT_e is the electron temperature in eV, and $g(p)$ and $g(q)$ are the statistical weights of p and q levels, respectively.

The depopulating flux from 2P state for both the transitions, 2P − 2S

and 2P − 1S, can be evaluated as

$$\text{Flux}_{2\text{P}-1\text{S}} = A(2\text{P}, 1\text{S})\; n(2\text{P}) \tag{2.18}$$

$$\text{Flux}_{2\text{P}-2\text{S}} = F(2\text{P}, 2\text{S})\; n_\text{e}\; n(2\text{P}), \tag{2.19}$$

where, n_e is the electron density, $n(2\text{P})$ is the population of 2P state, $A(2\text{P}, 1\text{S})$ and $F(2\text{P}, 2\text{S})$ are the spontaneous transition probability and deexcitation rate coefficients for the corresponding transitions, respectively.

Here we have considered $T_\text{e} = 10$ eV, approximate value of T_e at hydrogen emission location. The quantities $n(2\text{P})$ and $A(2\text{P}, 1\text{S})$ have been obtained from the collisional-radiative model code. Using the relation Eq. (2.17) the rate coefficient $F(2\text{P}, 1\text{S})$ has been evaluated from rate coefficient $C(1\text{S}, 2\text{P})$, shown in Fig. 2.8(b). The obtained values of depopulating flux for $n_\text{e} = 1 \times 10^{18}$ m^{-3} and 1×10^{19} m^{-3} are shown in Tab. 2.3.

n_e in m^{-3}	Flux 2P → 2S [m^{-3}s^{-1}]	Flux 2P → 1S [m^{-3}s^{-1}]	Ratio
1.0×10^{18}	2.03×10^{1}	1.25×10^{4}	1.62×10^{-3}
1.0×10^{19}	1.94×10^{3}	1.19×10^{5}	1.63×10^{-2}

Tab. 2.3: Comparison of depopulating flux from 2P state due to 2P − 2S and 2P − 1S transitions

The evaluated depopulating fluxes suggest that for the n_e range of interest, 10^{18} m^{-3} to 10^{19} m^{-3}, the depopulating flux from 2P state due to 2P − 1S radiative transition is much higher and therefore, the contribution from 2P − 2S transition in depopulating 2P state can be neglected.

In conclusion, electron-impact excitation from the ground and radiative decay to the ground state are the main processes responsible for populating and depopulating 2P state of hydrogen, respectively, in the T_e and n_e range of interest.

CHAPTER 3

Population-Alignment Collisional-Radiative (PACR) model

In a Collisional-Radiative model a Maxwellian distribution is implicitly assumed for the electron velocity distribution function (EVDF), and the concept of temperature is used to quantify the activities of electrons. However, in actual plasmas the EVDF can deviate from the Maxwell distribution and can even be anisotropic. Electron-impact excitation by electrons having an anisotropic velocity distribution produce imbalance of population among the magnetic sublevels in a state and the emission lines from such levels are generally polarized. The imbalance of population among the sublevels in a level is expressed with a quantity known as the alignment.

Plasma Polarization Spectroscopy is the framework which deals with polarization of emission lines, due to the anisotropy of electron collisions. The intensity of the radiation from atoms in a plasma provides information concerning how many atoms are excited, i.e., the population of the upper level. The polarization characteristics of the radiation provides information about how these

atoms are excited in a plasma, i.e., about the alignment of the upper level. The Population-Alignment Collisional-Radiative (PACR) model is the theoretical tool which enables to interpret the observed intensity and polarization of emission lines in terms of an anisotropic EVDF.

In this chapter, the theoretical framework for the PACR model is described briefly, which is based on Ref. [1]. The theoretical framework developed in the photon-atom interaction studies constitutes the theoretical basis of the PACR model. In particular, the formulations described in this chapter are based on Omont [35] and applied to the present problem in Fujimoto et al. [36].

3.1 Population and Alignment

Here an axisymmetric system with respect to the quantization axis is assumed where there is no orientation among the magnetic sublevels. These assumptions imply that the atomic system can be described as an incoherent superposition of level states, and that its density matrix [37] reduces to a sum of density matrices for each level αJ or p,

$$\rho(p) = \sum_{MN} \rho_{M,N}(p) |\alpha JM\rangle\langle\alpha JN|, \tag{3.1}$$

where $\rho_{M,N}(p)$ with $N \neq M$ is the coherence and with $N = M$ is the population of the magnetic sublevel M. In place of $|\alpha JM\rangle\langle\alpha JN|$, the irreducible tensorial set is introduced

$$T_q^{(k)} = \sum_M N(-1)^{J-N} \langle JJM - N|kq\rangle |\alpha JM\rangle\langle\alpha JN|, \tag{3.2}$$

where $\langle JJM - N|kq\rangle$ is the Clebsch-Gordan coefficient. As it has been assumed that there is no orientation among the sublevels, in the present discussion only situations in which $\rho_{M,N}(p) = 0$ for $N \neq M$ is considered. Expanding Eq. (3.1) in

terms of Eq. (3.2).

$$\rho(p) = \rho_0^0(p)T_0^{(0)}(p) + \rho_0^2(p)T_0^{(2)} + \cdots , \tag{3.3}$$

where the expansion coefficients are given by

$$\rho_q^k(p) = \sum_{MN}(-1)^{J-N}\langle JJM - N|kq\rangle\rho_{M,N}(p). \tag{3.4}$$

It is noted that the odd rank terms are dropped in Eq. (3.3) because, owing to the symmetry of the situation, they do not appear in the formulation below. This is connected with the fact that, for an atom, a collision of a perturber incident on it from $+z$-direction cannot be distinguished from a collision from the $-z$-direction. Therefore, an orientation $\rho_q^1(p)$ does not appear. In the following only the first two terms are retained in this equation and higher rank terms are neglected. Thus two quantities are assigned to each level p: the population $\rho_0^0(p)$ and the alignment $\rho_0^2(p)$. The conventional population is given by

$$n(p) = \sqrt{2J_p + 1}\,\rho_0^0(p). \tag{3.5}$$

The population was the central problem of the conventional intensity spectroscopy and it was treated on the assumption of a Maxwell distribution for EVDF. The alignment is a measure of the population imbalance among the magnetic sublevels in a level, and it gives rise to linear polarization of emission lines. For the purpose of simplicity, $a(p)$ is used in place of $\rho_0^2(p)$.

Figure 3.1 shows, as an example of $J = 2$, the population distribution having (a) positive alignment and (b) a negative alignment. Figure 3.2 shows the structure of system which has been considered here. Each level has been assigned two quantities, $n(p)$ and $a(p)$, both in units of m^{-3}. It is assumed here that the ground state atoms, denoted as "1" in Fig. 3.2, are not aligned.

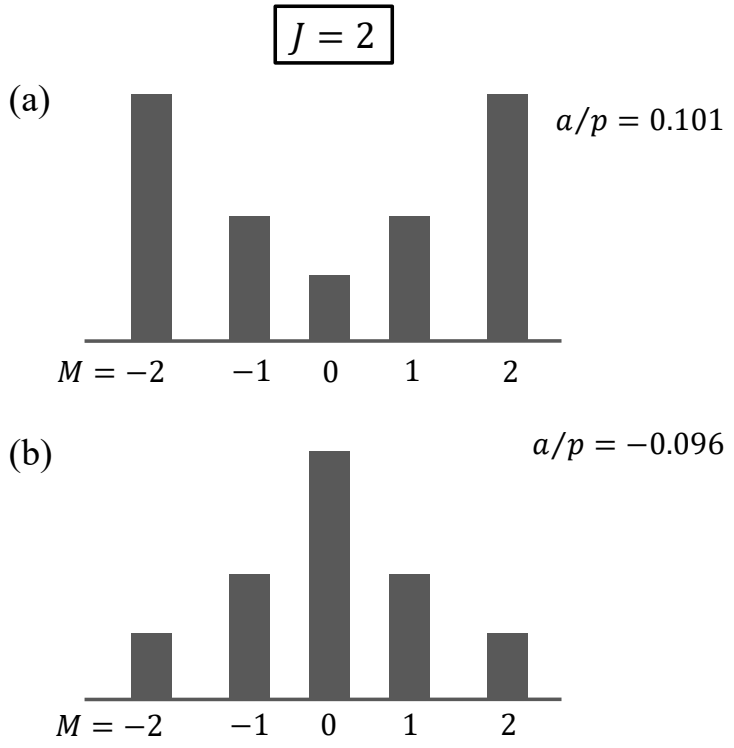

Fig. 3.1: Examples of (a) positive and (b) negative alignment [1]

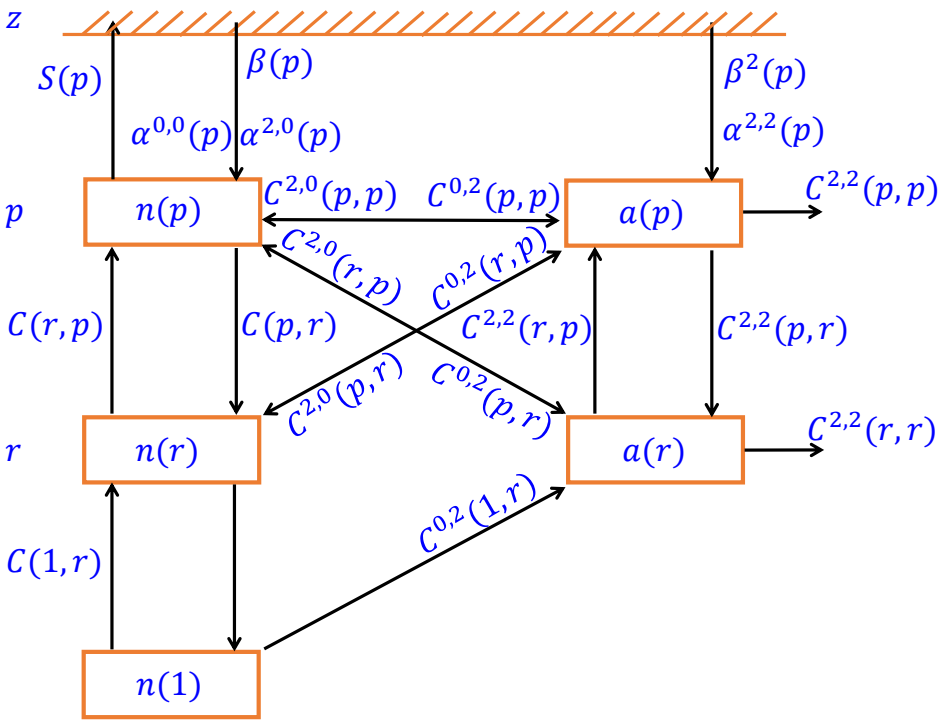

Fig. 3.2: Populations and alignments of levels and collision processes between them [1]

The polarization degree, P, is defined as

$$P = \frac{I_\pi - I_\sigma}{I_\pi + I_\sigma}, \tag{3.6}$$

where, I_π is the light linearly polarized in the direction parallel to the quantization axis, whereas I_σ is the light circularly polarized in the plane perpendicular to the quantization axis. For an axisymmetric system, $I_{\sigma+} \approx I_{\sigma-}$, with $I_{\sigma+}$ and $I_{\sigma-}$ corresponding to right circularly polarized light and left circularly polarized light, respectively. In this expression, $I_{\sigma+} \approx I_{\sigma-} \equiv I_\sigma$ is used. The total intensity emitted during any transition is given by

$$I_{\mathrm{tot}} = I_\pi + 2I_\sigma. \tag{3.7}$$

Instead of polarization degree P, a quantity known as longitudinal alignment, A_{L}, is employed to simplify theoretical expressions and it is expressed as

$$A_{\mathrm{L}} = \frac{I_\pi - I_\sigma}{I_\pi + 2I_\sigma} \tag{3.8}$$

$$= \frac{2P}{3 - P}. \tag{3.9}$$

For a transition from $p \to s$, A_{L} is related to the relative alignment, $a(p)/n(p)$, as

$$A_{\mathrm{L}}(p,s) = (-1)^{J_p+J_s}\sqrt{\frac{3}{2}}(2J_p+1)\begin{Bmatrix} J_p & J_p & 2 \\ 1 & 1 & J_s \end{Bmatrix}\frac{a(p)}{n(p)}, \tag{3.10}$$

where $\{\cdots\}$ is the $6-j$ symbol.

The collisional-radiative (CR) model is generalized to incorporate the system of $a(p)$, and this new method is known as the Population-Alignment Collisional-Radiative (PACR) model. In this model, transition processes as creation of alignment in a level from a population in another level, transfer of alignment from a level to another level, and so on have included. Figure 3.2 shows these collision processes.

3.2 Alignment creation cross sections

In PACR model the cross sections relating to the population and the alignment are employed and denoted by $Q_q^{kk'}(r,p)$ for excitation or deexcitation from $\alpha' J' \to \alpha J$ or $r \to p\,(r \neq p)$. The basic cross section data are the cross sections $Q_{\alpha JM,\alpha' J' M'}$ from a magnetic sublevel $\alpha' J' M'$ to a magnetic sublevel αJM, where α is the relevant quantum number for the level. The cross sections are defined as

$$Q_0^{0,0}(r,p) = (2J+1)^{-1} \sum_{MM'} Q_{\alpha JM,\alpha' J' M'} \tag{3.11}$$

$$Q_0^{0,2}(r,p) = (2J+1)^{-1} \sum_{MM'} (-1)^{J'-M'} \langle J'J'M' - M|20\rangle\, Q_{\alpha JM,\alpha' J' M'} \tag{3.12}$$

$$Q_0^{2,0}(r,p) = \sum_{M} (-1)^{J-M} \langle JJM - M|20\rangle \sum_{M'} Q_{\alpha JM,\alpha' J' M'} \tag{3.13}$$

$$Q_0^{2,2}(r,p) = \sum_{MM'} (-1)^{J+J'+M+M'} \langle J'J'M' - M'|20\rangle \langle JJM - M|20\rangle Q_{\alpha JM,\alpha' J' M'}, \tag{3.14}$$

where $\langle JJM - M|kq\rangle$ is the Clebsch-Gordan coefficient. Here, $Q_0^{0,0}(r,p)$ is cross section for the excitation or deexcitation. $Q_0^{0,2}(r,p)$ represents cross section for the alignment creation. $Q_0^{2,0}(r,p)$ and $Q_0^{2,2}(r,p)$ are the cross sections for the alignment-to-population and the alignment destruction, respectively.

The alignment creation cross section, $Q_0^{0,2}(r,p)$, is expressed in terms of the experimentally derived longitudinal alignment $A_{\mathrm{L}}(p,s)$ of the transition line $p \to s$ [1]. For a transition $r \to p \to s$ the alignment creation cross section by excitation or deexcitation is given by

$$Q_0^{0,2}(r,p) = (-1)^{J_p+J_s} \sqrt{\frac{2}{3}}\,(2J_p+1)^{-1} \begin{Bmatrix} J_p & J_p & 2 \\ 1 & 1 & J_s \end{Bmatrix}^{-1} A_{\mathrm{L}}(p,s)\, Q_0^{0,0}(r,p). \tag{3.15}$$

3.3 Electron velocity distribution function and rate coefficients

An axisymmetric system with respect to the quantization is assumed here. The velocity distribution can be expanded in terms of Legendre polynomials,

$$f_v(\theta) = \sum_K f_K P_K(\cos\theta) \tag{3.16}$$

with

$$f_K = \frac{2K+1}{2} \int f_v(\theta) P_K(\cos\theta) \sin\theta \, \mathrm{d}\theta \tag{3.17}$$

A situation is considered in which the perturbers are not monoenergetic, but they have a distribution over v; the distribution is expressed by $f(v,\theta)$. It should be noted here that the normalization condition is

$$\int\int\int f(v,\theta) v^2 \mathrm{d}v \sin\theta \mathrm{d}\theta \mathrm{d}\phi = 1, \tag{3.18}$$

or

$$\int\int f(v,\theta) v^2 \sin\theta \mathrm{d}\theta = 1/2\pi. \tag{3.19}$$

The rate coefficients for transition $\alpha J \to \alpha' J'$ or $r \to p$ are defined as

$$C^{0,0}(r,p) = \int Q_0^{0,0}(r,p) 4\pi f_0(v) v^3 dv, \tag{3.20}$$

$$C^{0,2}(r,p) = \int Q_0^{0,2}(r,p) [4\pi f_2(v)/5] v^3 dv, \tag{3.21}$$

$$C^{2,0}(r,p) = \int Q_0^{2,0}(r,p) [4\pi f_2(v)/5] v^3 dv, \tag{3.22}$$

$$\begin{aligned} C^{2,2}(r,p) = & \int [Q_0^{2,2}(r,p) + Q_1^{2,2}(r,p) + Q_2^{2,2}(r,p)][4\pi f_0(v)/5] v^3 dv \\ & + \int [2Q_0^{2,2}(r,p) + Q_1^{2,2}(r,p) - 2Q_2^{2,2}(r,p)][4\pi f_2(v)/35] v^3 dv \\ & + \int [6Q_0^{2,2}(r,p) - 4Q_1^{2,2}(r,p) + Q_2^{2,2}(r,p)][4\pi f_4(v)/105] v^3 dv. \end{aligned} \tag{3.23}$$

Here, $C_0^{0,0}(r,p)$ is rate coefficient for the excitation or deexcitation. $C_0^{0,2}(r,p)$ represents rate coefficient for the alignment creation. $C_0^{2,0}(r,p)$ and $C_0^{2,2}(r,p)$ are

the rate coefficients for the alignment-to-population and the alignment destruction, respectively.

It is noted that the above expressions of the rate coefficient may look different from the conventional definition, e.g., $C(r,p) = \int f(v) v \sigma(r,p) \mathrm{d}v$. This is due to the difference in the expressions for the distribution functions; in the conventional expression the EVDF is assumed isotropic and the normalization condition is $\int f(v) \mathrm{d}v = 1$, while in the present formulation, the corresponding normalization is $\int 4\pi f_0(v) v^2 \mathrm{d}v = 1$.

3.4 Rate equations for the population and the alignment

The temporal developments of the population, $n(p)$, and the alignment, $a(p)$, of level p are described by rate equations. The rate equation for the ionizing plasma component of population is expressed as

$$\begin{aligned}\frac{\mathrm{d}}{\mathrm{d}t} n_1(p) = & \sum_{r \neq p} \Big[C(r,p) n_\mathrm{e} + A(r,p) \Big] n_1(r) \\ & - \left[\sum_r A(p,r) + \left(\sum_{r \neq p} C(p,r) + S(p) \right) n_\mathrm{e} \right] n_1(p) \\ & + \sum_{r \neq p} C^{2,0}(r,p) n_\mathrm{e} a_1(r) \\ & - C^{2,0}(p,p) n_\mathrm{e} a_1(p).\end{aligned} \tag{3.24}$$

The first line on the right-hand side represents populating flux into level p from higher and lower lying levels. It includes both the collisional and radiative fluxes. The second line is the total depopulating flux from level p due to collisional and radiative transitions. The third line gives the creation of population in this level from population imbalance among the magnetic sublevels, i.e., the alignment, in other levels. The last line is a correction term to the second line due to the presence of alignment and unequal depopulation rates among the magnetic sublevels in this level.

The rate equation for the ionizing plasma component of alignment is written as

$$\begin{aligned}\frac{\mathrm{d}}{\mathrm{d}t}a_1(p) =& \sum_{r\neq p} C^{0,2}(r,p)n_\mathrm{e}n_1(r) \\ & - C^{0,2}(p,p)n_\mathrm{e}n_1(p) \\ & + \sum_{r\neq p}\Big[A^{2,2}(r,p) + C^{2,2}(r,p)n_\mathrm{e}\Big]a_1(r) \\ & - \Big[\sum_r A(p,r) + C^{2,2}(p,p)n_\mathrm{e}\Big]a_1(p).\end{aligned} \tag{3.25}$$

The first line on the right-hand side represents the creation of alignment in this level from population in other levels. The second line consists of two contributions, the first part corresponds to the creation of alignment by unequal depopulation rates of the magnetic sublevels in this level, and the second part is the alignment creation by elastic collisions. The third line corresponds to the transfer of alignment from other levels to this level. The last line is for the decay of alignment. The first term is due to the radiative decay to lower energy levels. The second term is for the collisional relaxation of alignment in this level.

CHAPTER 4

PACR model for Lyman-α line

The theoretical framework for polarization of an emission line caused by the anisotropic collisions with electrons, known as the PACR (Population-Alignment Collisional-Radiative) model is described in chapter 3. We have developed the PACR model for Lyman-α line by following the methodology proposed by Fujimoto [1]. The model results enable to interpret the experimentally measured polarization degree in Lyman-α line in terms of anisotropy in the EVDF. An anisotropic EVDF having different electron temperatures in the directions parallel and perpendicular with respect to the magnetic field has been considered for constructing the model. In this chapter we present details of the developed PACR model for Lyman-α [38].

4.1 Polarization in Lyman-α line produced by electron impact on atomic hydrogen

Many theoretical calculations and experiments were carried out for the polarization in Lyman-α line produced by electron-impact excitation of atomic hydrogen [39,

40, 41]. The results were obtained under the condition that hydrogen atoms are excited by a monoenergetic electron beam, and that the emitted Lyman-α radiation is observed from 90° with respect to the incident electron beam axis as shown in Fig. 4.1.

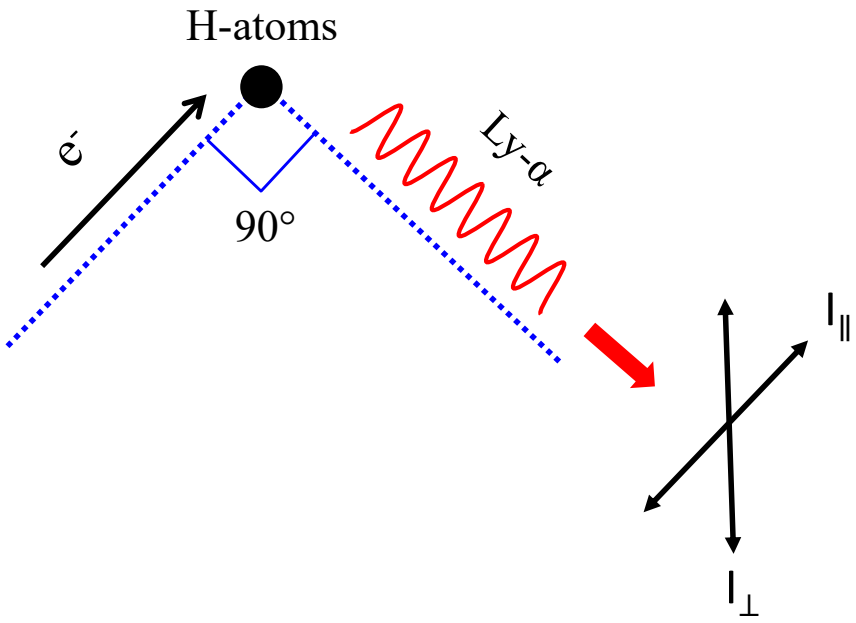

Fig. 4.1: Schematic representation of the experimental condition for measuring the polarization of Lyman-α line from atomic hydrogen excited by electron impact

The polarization degree is defined as:

$$P = \frac{I_{\parallel} - I_{\perp}}{I_{\parallel} + I_{\perp}},$$

where $I_{\parallel}$ and $I_{\perp}$ are the intensities with the electric vector parallel and perpendicular to the electron beam axis, respectively. Fite and Brackmann reported the first experimental measurement of the polarization in Lyman-α line produced by electron impact excitation of atomic hydrogen in 1958 [39]. However, the data were essentially of a preliminary nature, and have very large error bars. Subsequently, the experimental results for the polarization in Lyman-α line produced by (i) electron impact on atomic and molecular hydrogen, and (ii) by electric field quenching of metastable 2S hydrogen atoms were reported by Ott et al. [40]. In this experiment a LiF crystal placed at its Brewster's angle was used as a

polarization analyzer. In 1997, James et al. also conducted experiments with the same purpose of measuring the polarization in Lyman-α line from atomic hydrogen by electron impact from near threshold to 1800 eV [41]. Additionally, they also performed convergent-close-coupling (CCC) calculations of the Lyman-α polarization.

The main objective of the above mentioned studies was to provide accurate measurements of the polarization in Lyman-α line produced by electron-impact excitation of atomic hydrogen to obtain information concerning the relative populations of the degenerate magnetic sublevels in the excitation process. In addition, since electron-impact excitation cross sections are generally measured in a crossed-beam configuration, in which the emitted radiation is detected at 90° with respect to the electron-beam axis, precise polarization measurements are necessary to correct these data to obtain values for the integral cross section.

Figure 3 of Ref.[41] shows results of various experiments and theoretical calculations for the polarization in Lyman-α, with the incident electron beam energy varied from 10 eV to 1800 eV. The results indicate that the value of polarization degree is positive and negative for lower and higher electron energies, respectively. In Fig. 4.2 the results reported by James et al. [41] have been shown which are used in constructing the PACR model for Lyman-α line.

4.2 PACR model for Lyman-α

The Lyman-α line consists of two components, i.e., $1\,^2S_{1/2} - 2\,^2P_{1/2}$ and $1\,^2S_{1/2} - 2\,^2P_{3/2}$. Figure 4.3 shows all the possible transitions among magnetic sublevels relating to the Lyman-α line. As indicated in the figure, $\Delta m_J = 0$ transition emits $\pi-$light, linearly polarized in the quantization axis direction, and $\Delta m_J = \pm 1$ transitions emit $\sigma-$light, circularly polarized in the plane perpendicular to the quantization axis. Here m_J means magnetic quantum number of the state having total angular momentum quantum number J. When all the magnetic sublevels are

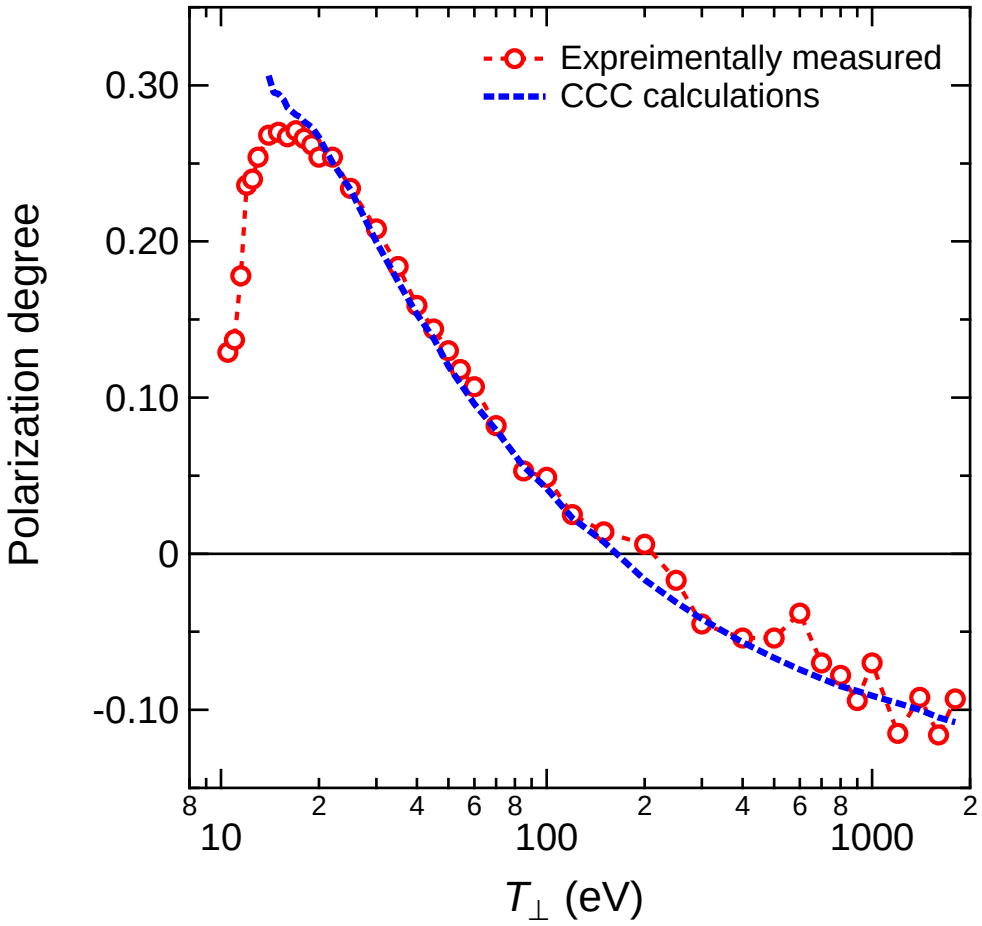

Fig. 4.2: Experimental and theoretical values for polarization in Lyman-α line from atomic hydrogen excited by electron impact over energy range from threshold to 1800 eV.

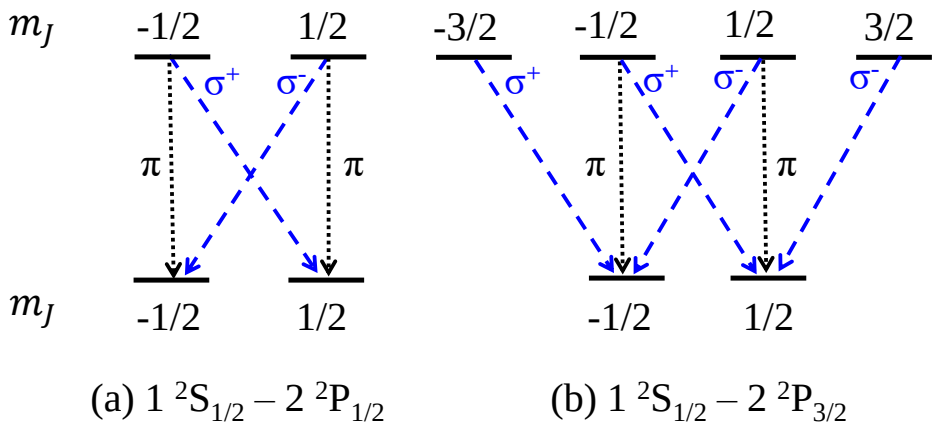

Fig. 4.3: Transitions among the magnetic sublevels relating to the Lyman-α line. The dashed and dotted lines indicate $\sigma-$light and $\pi-$light, respectively.

populated uniformly, emitted light intensity is isotropic, i.e., the line is not polarized. However, when atoms are excited by anisotropic collisions with electrons, the imbalance of population is created among sublevels and results in the polarization of emitted light.

4.2.1 Construction of rate equations

Here, the quantization axis is taken to be in the magnetic field direction. We assume an axisymmetric system with respect to the quantization axis where there is no orientation among the magnetic sublevels, i.e., the populations of m_J and $-m_J$ sublevels are the same. For this reason the emitted light corresponding to the $1\,^2\mathrm{S}_{1/2} - 2\,^2\mathrm{P}_{1/2}$ transition is not polarized, while the $1\,^2\mathrm{S}_{1/2} - 2\,^2\mathrm{P}_{3/2}$ transition may emit polarized light. For developing the model, first the $1\,^2\mathrm{S}_{1/2} - 2\,^2\mathrm{P}_{3/2}$ transition is considered and in the final result influence of the unpolarized $1\,^2\mathrm{S}_{1/2} - 2\,^2\mathrm{P}_{1/2}$ transition is taken into account.

As described in Sec. 3.1, in PACR model each energy level p is assigned two quantities: the population $n(p)$ and the alignment $a(p)$. In present case level p is $2\,^2\mathrm{P}_{3/2}$ level of Hydrogen. The structure of PACR model considered for the case of Lyman-α line is shown in Fig. 4.4. The quantities indicated by $C^{0,0}(1,p)$, $C^{0,2}(1,p)$, and $C^{2,2}(p,p)$ represent the rate coefficients for population creation, alignment creation, and alignment destruction, respectively.

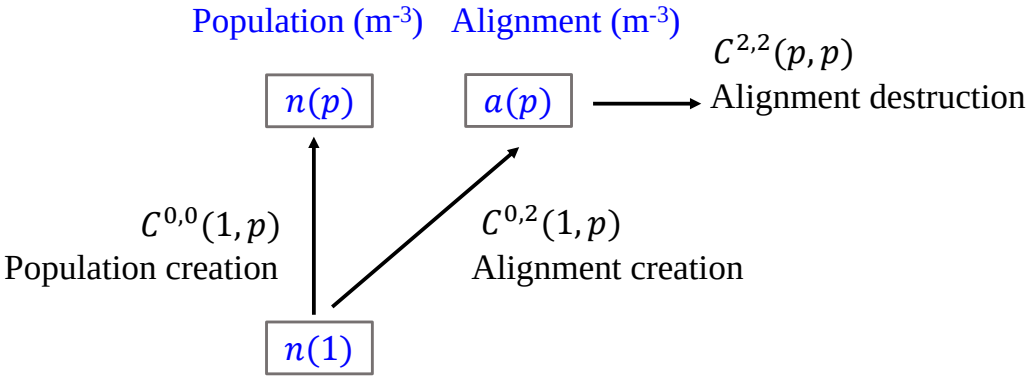

Fig. 4.4: Structure of PACR model considered for Lyman-α line

The collisional-radiative calculations, carried out by considering plasma parameters of the edge LHD plasma as discussed in chapter 3, show that the population of the excited state $2\,^2P_{3/2}$ is balanced by the electron impact excitation from the ground state and the spontaneous radiative decay. This situation is illustrated in Fig. 4.5.

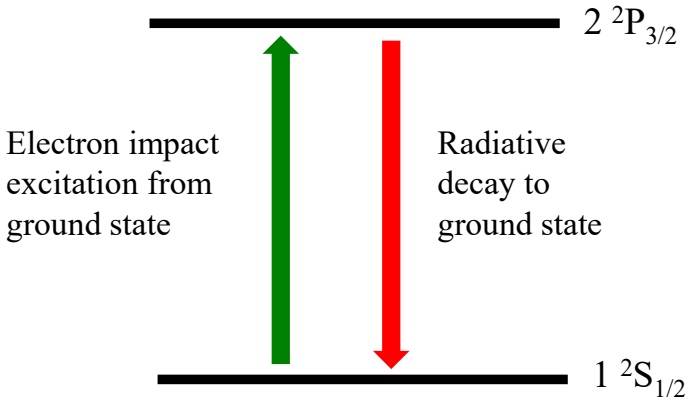

Fig. 4.5: Population of the state $2\,^2P_{3/2}$ is balanced by the electron-impact excitation from the ground state and by radiative decay to ground state

By using this result it is clear that in Eq. 3.24, terms corresponding to the electron impact excitation from the ground state and radiative decay to the ground state survives. Since the population is balanced by these two processes, rate of change of population is negligible and the rate equation for population can be expressed as

$$C^{0,0}(1,p)\, n_e\, n(1) = \sum_s A(p,s)\, n(p), \tag{4.1}$$

where $C^{0,0}(1,p)$ is the rate coefficient for electron-impact excitation, $A(p,s)$ is the Einstein A coefficient for the transition from a level p to a lower level s, and n_e is the electron density. Similarly, from Eq. 3.25 the rate equation for $a(p)$ can be written as

$$C^{0,2}(1,p)\, n_e\, n(1) = \left[\sum_s A(p,s) \; + C^{2,2}(p,p)\, n_e\right] a(p), \tag{4.2}$$

where $C^{0,2}(1,p)$ and $C^{2,2}(p,p)$ are the rate coefficients for the alignment creation

and the alignment destruction, respectively. The detailed description and expressions for the rate coefficients $C^{0,0}(1,p)$, $C^{0,2}(1,p)$, and $C^{2,2}(p,p)$ are given in Sec. 4.2.4. The population, $n(p)$, and the alignment, $a(p)$, are then derived as

$$n(p) = \frac{C^{0,0}(1,p)\, n_{\rm e}}{\sum_s A(p,s)}\, n(1), \tag{4.3}$$

$$a(p) = \frac{C^{0,2}(1,p)\, n_{\rm e}}{\left[\sum_s A(p,s) \; + C^{2,2}(p,p)\, n_{\rm e}\right]}\, n(1). \tag{4.4}$$

The ratio $a(p)/n(p)$ is referred to as the relative alignment and can be expressed as following:

$$\frac{a(p)}{n(p)} = \frac{C^{0,2}(1,p)}{\left[\sum_s A(p,s) \; + C^{2,2}(p,p)\, n_{\rm e}\right]}\, \frac{\sum_s A(p,s)}{C^{0,0}(1,p)}. \tag{4.5}$$

4.2.2 Definition of Longitudinal alignment ($A_{\rm L}$) and Polarization degree (P)

For a transition from a level p to a level s, the longitudinal alignment $A_{\rm L}$ is related to the relative alignment, $a(p)/n(p)$, as [1]

$$A_{\rm L}(p,s) = (-1)^{J_p+J_s}\sqrt{\frac{3}{2}}(2J_p+1) \left\{ \begin{array}{ccc} J_p & J_p & 2 \\ 1 & 1 & J_s \end{array} \right\} \frac{a(p)}{n(p)}, \tag{4.6}$$

where $\left\{ \cdots \right\}$ is the 6-j symbol.

We consider a case in which the emission line is observed from a direction perpendicular to the quantization axis, using a linear polarizer. The polarization degree, P, and the longitudinal alignment, $A_{\rm L}$, are defined as [1]

$$P = \frac{I_{\parallel} - I_{\perp}}{I_{\parallel} + I_{\perp}}, \tag{4.7}$$

$$A_{\mathrm{L}} = \frac{I_{\parallel} - I_{\perp}}{I_{\parallel} + 2I_{\perp}}, \tag{4.8}$$

where $I_{\parallel}$ and $I_{\perp}$ are the linearly polarized light intensities in the directions parallel and perpendicular to the quantization axis, respectively. In other words, the polarization degree, P, can be obtained from the longitudinal alignment, A_L, using the following relation [1]

$$P = \frac{3A_{\mathrm{L}}}{2 + A_{\mathrm{L}}}. \tag{4.9}$$

Our main goal is to evaluate the polarization degree. To this end we first evaluate longitudinal alignment, A_{L}, by using the Eq. (4.6) and then from this value we calculate the value of polarization degree using Eq. (4.9).

4.2.3 Anisotropic electron velocity distribution function

Calculations of the rate coefficients, $C^{0,0}(1,p)$, $C^{0,2}(1,p)$, and $C^{2,2}(p,p)$ are carried out under a certain EVDF. We assume that the EVDF is axisymmetric with respect to the quantization axis and the electron temperature has different values in the directions parallel and perpendicular to the quantization axis, i.e., magnetic field in our case.

The explicit expression for such EVDFs is given as [1]

$$f(v,\theta) = 2\pi\left(\frac{m}{2\pi k}\right)^{\frac{3}{2}}\left(\frac{1}{T_{\perp}^{2}T_{\parallel}}\right)^{\frac{1}{2}} \exp\left[-\frac{mv^{2}}{2k}\left(\frac{\sin^{2}\theta}{T_{\perp}} + \frac{\cos^{2}\theta}{T_{\parallel}}\right)\right], \tag{4.10}$$

where v is the absolute value of the velocity, θ is the pitch angle of the velocity with respect to the magnetic field, and m and k are the electron mass and the Boltzmann constant, respectively. Here, $T_{\parallel}$ and $T_{\perp}$ represent the electron temperature in the directions parallel and perpendicular to the magnetic field, respectively, as shown in Fig. 4.6.

Figure 4.7 shows the image plots for the considered anisotropic EVDF. The image plots have been generated for two different cases:

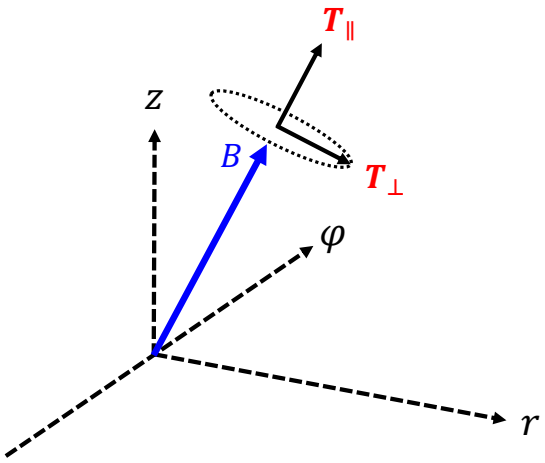

Fig. 4.6: Anisotropic EDVF having different electron temperatures in the parallel and perpendicular with respect to the magnetic field is considered

1. $T_{\parallel} = 10\,\mathrm{eV}$ and $T_{\perp} = 3\,\mathrm{eV}$
2. $T_{\parallel} = 10\,\mathrm{eV}$ and $T_{\perp} = 30\,\mathrm{eV}$.

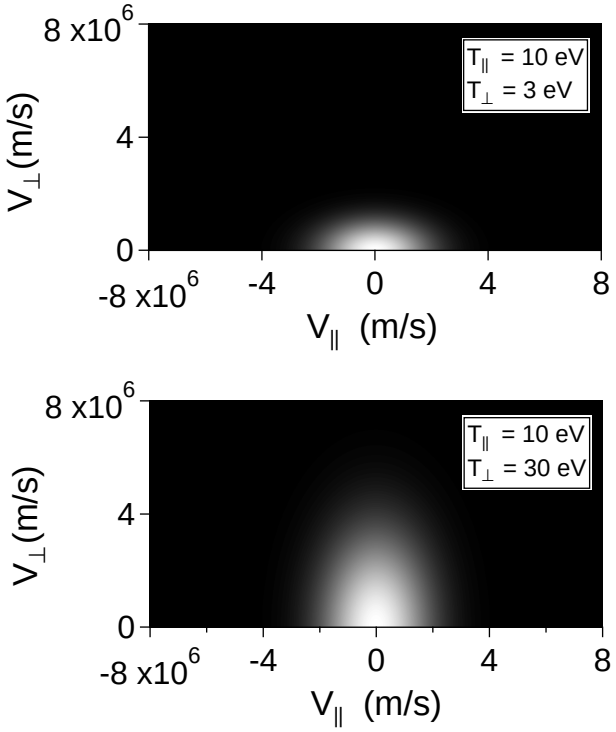

Fig. 4.7: Image plots for the considered anisotropic electron velocity distribution function

Positive and negative sign of $v_{\parallel}$ in images plots represent velocities in the direction parallel and anti-parallel to the magnetic field.

4.2.4 Evaluation of rate coefficients

The rate coefficients $C^{0,0}(1,p)$ and $C^{0,2}(1,p)$ are evaluated as [1]

$$C^{0,0}(1,p) = \int Q_0^{0,0}(1,p)\, 4\pi\, f_0(v)\, v^3\, \mathrm{d}v, \tag{4.11}$$

$$C^{0,2}(1,p) = \int Q_0^{0,2}(1,p)\, \left[4\pi\, f_2(v)\,/\,5\right] v^3\, \mathrm{d}v, \tag{4.12}$$

where $Q_0^{0,0}(1,p)$ and $Q_0^{0,2}(1,p)$ are the excitation and alignment creation cross sections, respectively, for the corresponding transition and are shown in Fig. 4.8. $f_0(v)$ and $f_2(v)$ are the coefficients of expansion of $f(v,\theta)$ by the Legendre polynomials, $P_K(\cos\theta)$, as

$$f(v,\theta) = \sum_K f_K(v)\, P_K(\cos\theta). \tag{4.13}$$

The coefficient $f_K(v)$ is explicitly given as

$$f_K(v) = \frac{2K+1}{2} \int f(v,\theta)\, P_K(\cos\theta)\, \sin\theta\, \mathrm{d}\theta. \tag{4.14}$$

The alignment creation cross section $Q_0^{0,2}(1,p)$ is obtained from the $Q_0^{0,0}(1,p)$ as [1]

$$Q_0^{0,2}(1,p) = (-1)^{J_p+J_s} \sqrt{\frac{2}{3}}\, (2J_p+1)^{-1} \begin{Bmatrix} J_p & J_p & 2 \\ 1 & 1 & J_s \end{Bmatrix}^{-1} A_{\mathrm{L}}(p,1)\, Q_0^{0,0}(1,p). \tag{4.15}$$

The data for $Q_0^{0,0}(1,p)$ and A_{L} are obtained from Refs. [33] and [41], respectively. Here, A_{L} is the value for the case where the hydrogen atoms are excited with a mono-energetic beam of electrons and the emitted Lyman-α radiation is observed from a direction perpendicular with respect to the incident electron beam axis. That means the observation angle is 90°. Figure 4.8 shows these quantities for the $1\,^2\mathrm{S}_{1/2} - 2\,^2\mathrm{P}_{3/2}$ transition.

The alignment destruction process may be understood as the collisional relaxation of the population imbalance among the magnetic sublevels. It is found

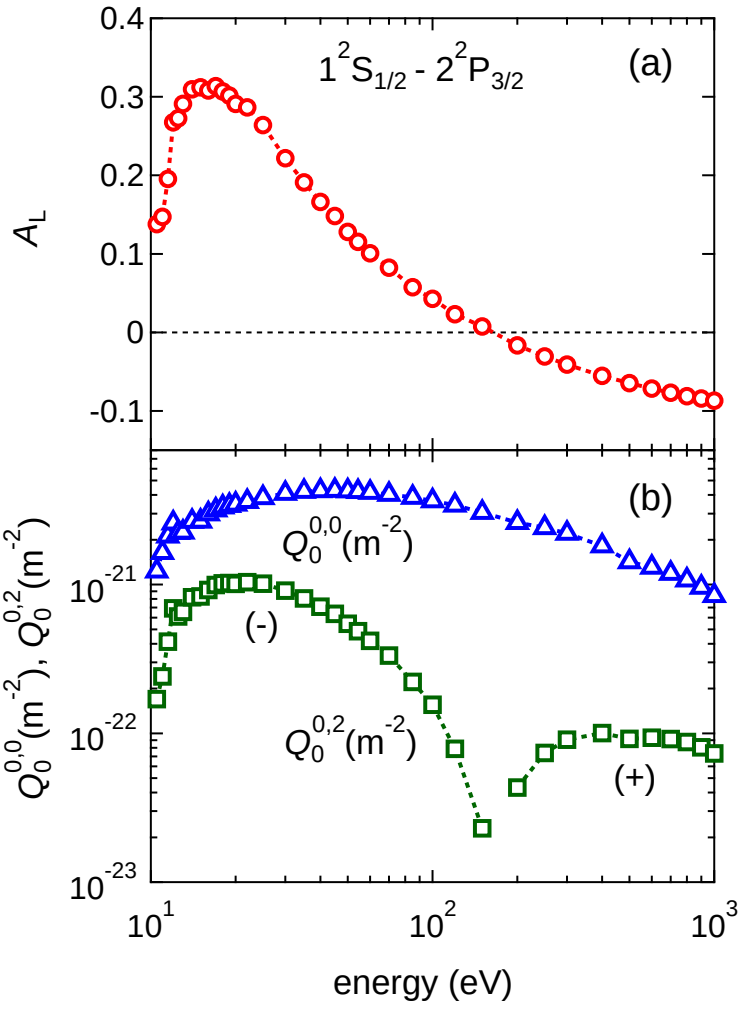

Fig. 4.8: (a) Longitudinal alignment, A_{L}, values under the condition that the hydrogen atoms are excited by a mono-energetic beam of electrons and (b) population creation cross section, $Q_0^{0,0}$, and alignment creation cross section, $Q_0^{0,2}$, for the $1\,^2\mathrm{S}_{1/2}$ - $2\,^2\mathrm{P}_{3/2}$ transition

that this process due to electron collisions relating to a state has some correlation with the Stark broadening of the emission line from that state and its rate coefficient can be approximated by the half width of the Stark broadening [42]. In present model, the Stark broadening data for the Lyman-α line have been adopted for evaluating $C^{2,2}(p,p)$ [43].

Figure 4.9 shows rate coefficients $C^{0,0}(1,p)$ and $C^{0,2}(1,p)$ evaluated using Eqs. 4.11 and 4.12. The values are shown for $T_{\|}$ from 10 eV to 40 eV, and $T_{\perp}$ is varied from 3 eV to 150 eV for each $T_{\|}$ value.

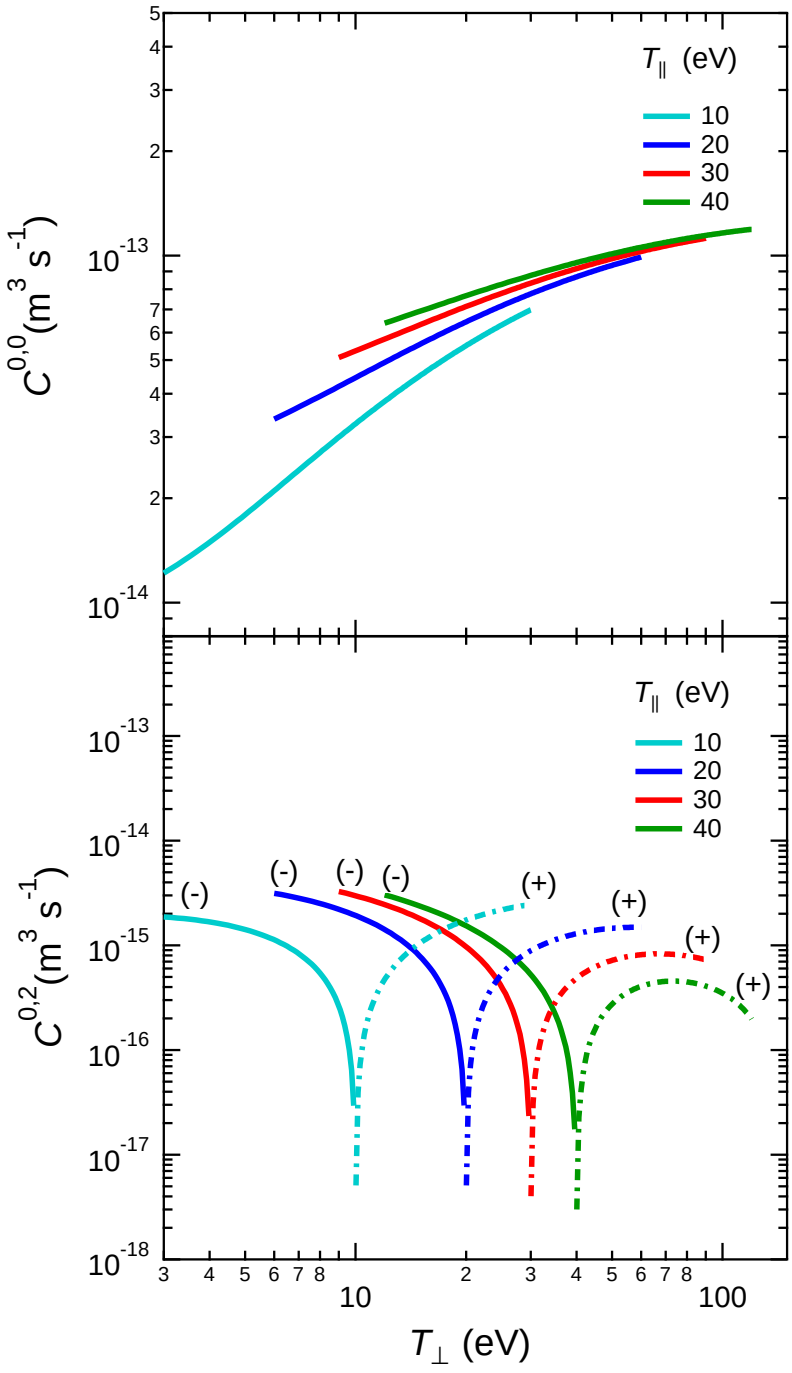

Fig. 4.9: Rate coefficients $C^{0,0}(1,p)$ and $C^{0,2}(1,p)$ evaluated for $T_{\|}$ from 10 eV to 40 eV, and $T_{\perp}$ is varied from 3 eV to 150 eV for each $T_{\|}$ value

4.2.5 PACR model results

The polarization degree for the transition $1\,^2\mathrm{S}_{1/2}-2\,^2\mathrm{P}_{3/2}$, which may emit polarized radiation is defined as

$$P_1 = \frac{I_{\parallel 1} - I_{\perp 1}}{I_{\parallel 1} + I_{\perp 1}}, \tag{4.16}$$

where $I_{\parallel 1}$ and $I_{\perp 1}$ stand for the intensities in the parallel and perpendicular directions to the quantization axis, respectively. The unpolarized transition, $1\,^2\mathrm{S}_{1/2} - 2\,^2\mathrm{P}_{1/2}$, is included in the observed line and its influence is evaluated. We assume that the $2\,^2\mathrm{P}_{1/2}$ and $2\,^2\mathrm{P}_{3/2}$ states are populated according to their statistical weights, i.e.,

$$n(2\,^2\mathrm{P}_{1/2}) = \frac{1}{2}\, n(2\,^2\mathrm{P}_{3/2}), \tag{4.17}$$

where $n(2\,^2\mathrm{P}_{1/2})$ and $n(2\,^2\mathrm{P}_{3/2})$ are the total populations of the states $2\,^2\mathrm{P}_{1/2}$ and $2\,^2\mathrm{P}_{3/2}$, respectively. The resulting polarization degree, denoted here as P_{res}, which takes into account both the transitions is expressed as

$$P_{\mathrm{res}} = \frac{(I_{\parallel 1} + I_{\parallel 2}) - (I_{\perp 1} + I_{\perp 2})}{(I_{\parallel 1} + I_{\parallel 2}) + (I_{\perp 1} + I_{\perp 2})}. \tag{4.18}$$

Here, $I_{\parallel 2}$ and $I_{\perp 2}$ are the intensities of the $1\,^2\mathrm{S}_{1/2}-2\,^2\mathrm{P}_{1/2}$ transition in the directions parallel and perpendicular to the quantization axis, respectively. Because the $1\,^2\mathrm{S}_{1/2} - 2\,^2\mathrm{P}_{1/2}$ line is unpolarized,

$$I_{\parallel 2} = I_{\perp 2} \tag{4.19}$$

$$I_{\parallel 2} + I_{\perp 2} = (I_{\parallel 1} + I_{\perp 1})/2, \tag{4.20}$$

from the assumption above, P_{res} is rewritten as

$$P_{\mathrm{res}} = \frac{I_{\parallel 1} - I_{\perp 1}}{(I_{\parallel 1} + I_{\perp 1}) + (I_{\parallel 2} + I_{\perp 2})} = \frac{2}{3}\, P_1. \tag{4.21}$$

The P_{res} evaluated for $T_\perp = 10\,\mathrm{eV}$ and $20\,\mathrm{eV}$ are shown in Fig. 4.10. The values of $T_\perp$ and electron density, n_{e}, are the typical values at the Lyman-α emission region.

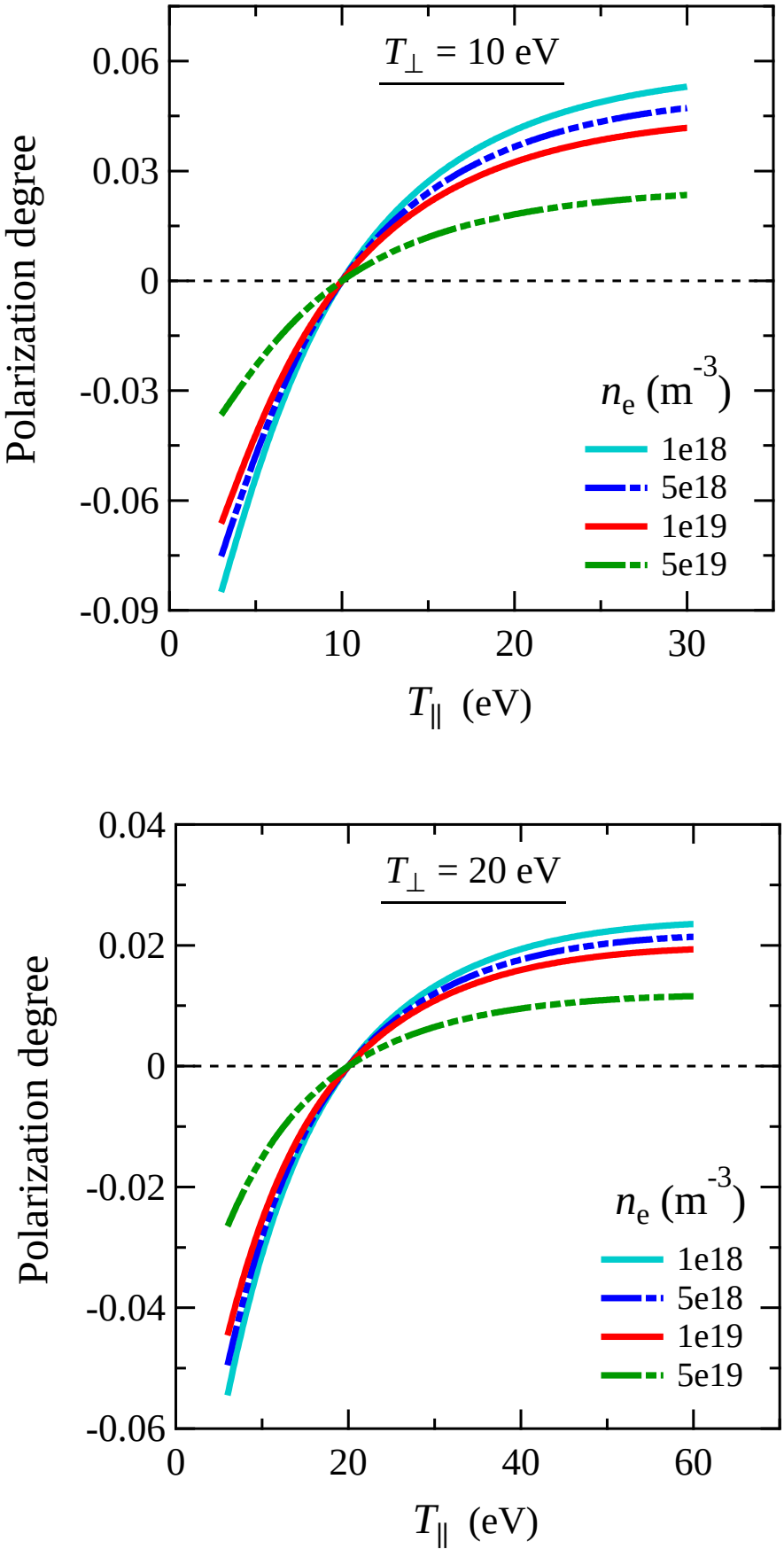

Fig. 4.10: Polarization degree evaluated for $T_\perp = 10\,\text{eV}$ and $20\,\text{eV}$. $T_\parallel$ and $T_\perp$ refer to the electron temperatures in the directions parallel and perpendicular to the magnetic field, respectively.

The results indicate that the value of polarization is negative for $T_\perp > T_\parallel$ and is positive for $T_\perp < T_\parallel$.

It should be noted here that the results of this theoretical model are applicable only to the cases in which emitted Lyman-α radiation is observed from 90° with respect to the quantization axis.

CHAPTER 5

Measurement of Lyman-α polarization in LHD

The polarization-resolved measurements of hydrogen Lyman-α line at 121.57 nm from the edge LHD plasma have been realized by incorporating the optical components designed and developed by the CLASP (Chromospheric Lyman-Alpha Spectro-Polarimeter) [23] team into an existing VUV spectrometer [44, 45]. The polarization measurement system on LHD consists of a normal incidence VUV spectrometer with a CCD (Charge Coupled Device) detector and the additionally installed optical components, namely, a half-waveplate, a polarization analyzer, and a high-reflectivity mirror.

In this chapter the polarization measurement system on LHD is described with the detailed information of each individual component used in the system. Also, an initial result of polarization degree obtained for a typical LHD discharge is presented.

5.1 Normal incidence VUV spectrometer

The VUV spectrometer (McPherson model 2253) is installed on an outboard midplane diagnostic port (#10-O) of the device. Figure 5.1 shows schematic diagram of the VUV spectrometer system with the horizontally-elongated poloidal cross section of LHD. The top view and the side view have been illustrated. This system is capable of measuring the full profile as well as the edge profile of the LHD plasma. However, because the Lyman-α is mainly emitted from the edge plasma, present measurements focus on the edge region of the plasma. The field of view of the spectrometer is indicated with dashed lines.

The focal length of the spectrometer is 3 m and the working wavelength range is from 30 nm to 320 nm. The spectrometer is equipped with two gratings of size 65 mm $\times$ 150 mm with different blazes of 140 nm and 300 nm and the radius of curvature of both the gratings is 2.9983 m. The present measurements have been carried out using the grating blazed at 140 nm. The entrance slit and the grating of the spectrometer are located at a distance of 13.177 m and 16.177 m from the torus center, respectively.

A back-illuminated CCD detector (Andor model DV435 with 1024×1024 pixels) is placed at the exit slit of the spectrometer to record the spectra. The size of the CCD is 13.3 mm $\times$ 13.3 mm with the pixel size of 13 μm $\times$ 13 μm. The CCD is generally operated at a temperature of -20°C to reduce thermal noise.

Since VUV radiation is strongly absorbed by molecular oxygen in the air, the detection of VUV radiation requires a high vacuum inside the system. A turbo molecular pump is used to evacuate the system and the vacuum of the order of $\sim 10^{-8}$ Torr is maintained inside the system.

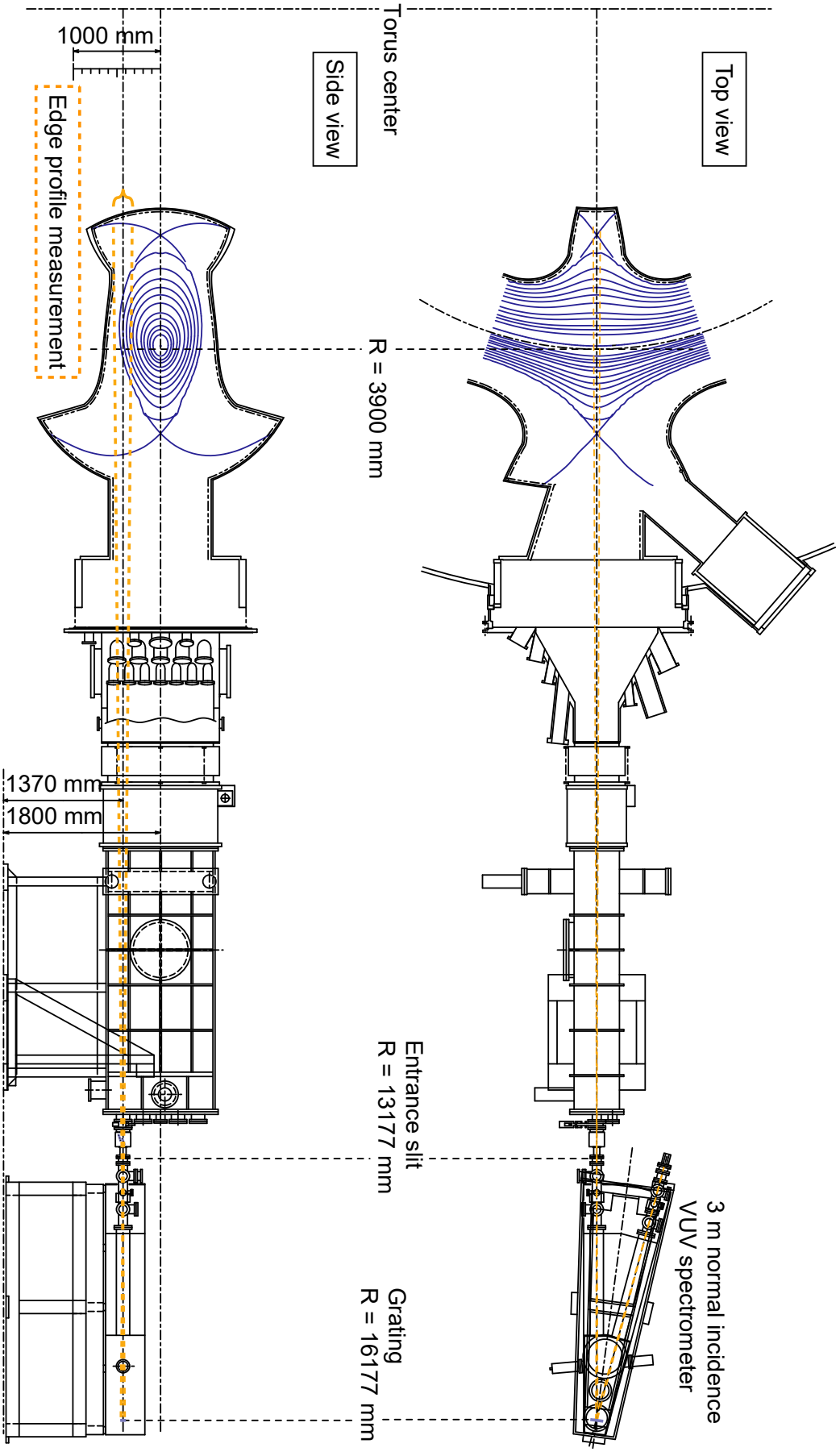

Fig. 5.1: Schematic drawing of the normal incidence VUV spectrometer with the horizontally-elongated poloidal cross section of LHD

5.2 Working of optical components

The schematic representation of mounting arrangement of the high-reflectivity mirror, the polarization analyzer, and the half-waveplate inside the spectrometer is shown in Fig. 5.2. The half-waveplate is placed just after the entrance slit and it is continuously rotated during the measurement, while the mirror and the polarization analyzer are mounted before the CCD detector. By using a combination of a rotating half-waveplate and a polarization analyzer, it is possible to monitor linearly polarized Lyman-α light at all angles. The performance of these components is strongly wavelength dependent and therefore, they are specially designed to use at Lyman-α wavelength. The comprehensive testing programs of the performance of these components have been carried out using the UVSOR (Ultraviolet Synchrotron Orbital Radiation) facility at the Institute for Molecular Sciences, Japan [46, 24, 25].

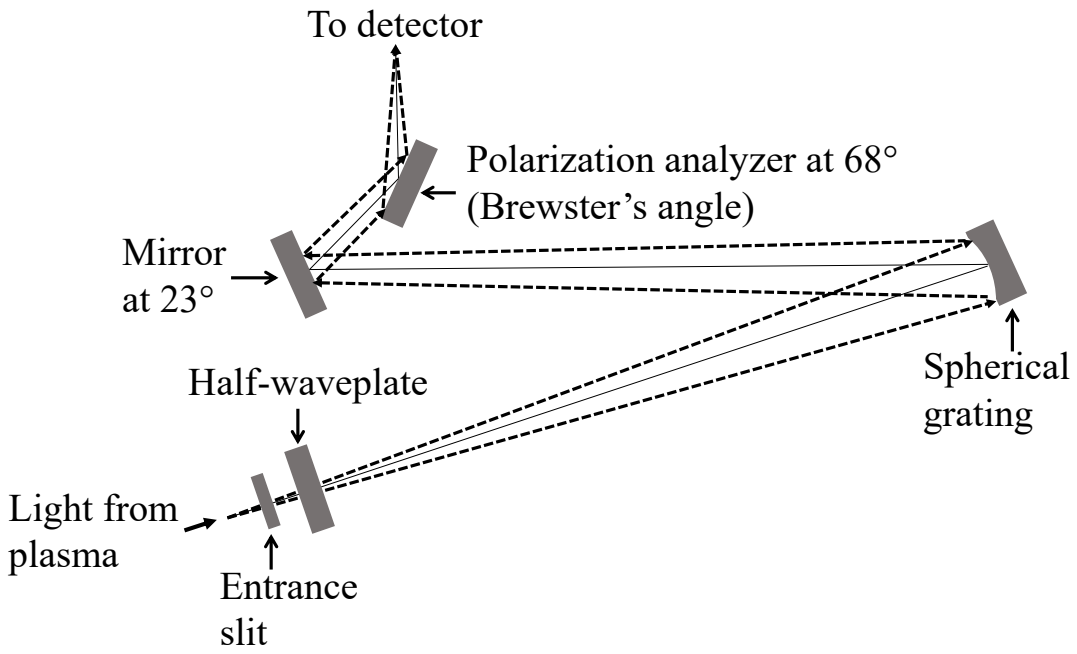

Fig. 5.2: Schematic representation of mounting arrangement of the optical components inside the spectrometer

5.2.1 Polarization analyzer

Diffracted light from the grating includes both p-polarized and s-polarized light. The light with electric vector perpendicular to the plane of incidence is called s-polarized light and the light with electric vector parallel to the plane of incidence is called p-polarized light. The main purpose of using polarization analyzer is to extract one linear polarization component from an incident light based on the principle of polarization of light by reflection at Brewster's angle.

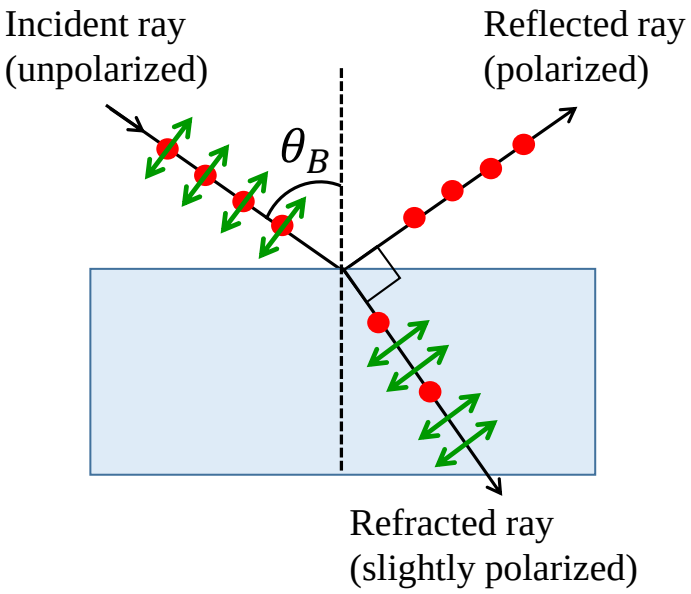

Fig. 5.3: Polarization of light by reflection at Brewster's angle

The Brewster's angle, denoted as θ_B, can be obtained using the following relation:

$$\tan\theta_B = \frac{n_2}{n_1},$$

where n_1 and n_2 are the refractive indices of the medium through which light travels and of the medium by which it gets reflected, respectively. Although MgF_2 plate at its Brewster's angle, $\sim 59°$, can be used as a polarization analyzer, the reflectivity of s-polarized light is very low, $\sim 21\,\%$ [25], and therefore it is not suitable for this purpose.

The polarization analyzer used for present measurements consists of thin two-layer coatings of SiO_2 and MgF_2 on a fused silica substrate [25]. This kind of high reflectivity polarizing coating offers high reflectivity for s-polarized light and almost zero reflectivity for p-polarized light at Lyman-α wavelength when used at its Brewster's angle [25, 47]. The measured value of the Brewster's angle for the polarization analyzer is 68° and the polarizing power, defined as

$$P = \frac{R_s - R_p}{R_s + R_p},$$

is about 0.99 [25], where R_s and R_p are the reflectivity of s-polarized and p-polarized light, respectively. This result indicate that the light reflected from the analyzer mainly consists of s-polarized component of incident light. Consequently, the polarization analyzer is placed at an angle of 68° from a light beam coming from the mirror in present system. Thus, only the s-polarized component of the observed light is monitored at the CCD detector. Due to this fact although the grating efficiency is different for p-polarized and s-polarized light, the final measurements are not affected by different grating efficiency values.

5.2.2 High-reflectivity mirror

Since the Polarization analyzer must be used at its Brewster's angle, 68°, an optical component is required through which a diffracted light coming from the grating is directed to the polarization analyzer in such a way that the incidence angle is 68°. To meet this requirement, the high-reflectivity mirror is placed at 23° angle with respect to a diffracted light beam coming from the grating. With this arrangement the reflected light beam from the mirror is incident on the polarization analyzer with 68° incidence angle.

The high-reflectivity mirror is fabricated with an Al base coating and MgF_2 (Magnesium Fluoride) overcoating on a CLEARCERAM-Z substrate and has a reflectivity of around 80% for both p-polarized and s-polarized light at

121.57 nm [25]. Although bare Aluminum offers a quite high reflectivity in the VUV range, 84% at 121.57 nm, when exposed to air it can easily get oxidized, and the formed oxidation layer significantly absorbs VUV light. On the other hand, it was demonstrated by Canfield et al. [48] that the use of MgF_2 overlayer coating effectively protects Al against oxidation. Hence, the MgF_2 overlayer coating has been applied on Al, and this kind of coating helps in achieving high throughput for the mirror.

5.2.3 Half-waveplate

Here we define angle of the observed linearly polarized light as "polarization angle", denoted as α, and it is measured in the clockwise direction as observed from the grating with reference to the vertical axis. As mentioned above since the polarization analyzer placed at Brewster's angle is utilized, with this system only light with angle $\alpha = 0$ can be monitored. On the other hand, to evaluate the polarization degree it is essential to detect the linearly polarized light at all angles. For this purpose, the half-waveplate specially designed to use at Lyman-α wavelength has been incorporated into the system.

Working principle of a half-waveplate

The half-waveplate used in experiment is made of MgF_2 because MgF_2 offers a high transparency at ultraviolet wavelength and also it is a uniaxial birefringent crystal, i.e., the refractive index of a material depends on polarization and propagation direction of light. The crystal has a single direction governing the optical anisotropy, known as the "optic axis" of crystal. The half-waveplate is fabricated such that the optic axis of the crystal is parallel to the waveplate surface. This results in two axes in the half-waveplate: the ordinary axis, with n_o refractive index, and the extraordinary axis, with n_e refractive index. The extraordinary axis is parallel to the optic axis of the crystal, whereas the ordinary axis is perpendicular

to the optic axis of the crystal. In case of MgF_2 $n_o < n_e$, hence for simplicity, the ordinary axis and the extraordinary axis are also referred to as the fast and the slow axis, respectively. The birefringence is often quantified as the difference between refractive indices n_e and n_o, i.e., $n_e - n_o$.

The half-waveplate used in present measurements is a compound zero-order waveplate, which consists of two stacked MgF_2 plates with slightly different thicknesses and their optic axes are rotated by 90° with respect to each other. The phase retardation, δ, introduced by a zero-order waveplate with a thickness difference of $d_1 - d_2$ is given by

$$\delta = 2\pi \frac{(n_e - n_o)(d_1 - d_2)}{\lambda},$$

where, $n_e - n_o$ is the birefringence at wavelength λ. From the measurements carried out by the CLASP team, it was found that the value of birefringence, $n_e - n_o$, is 0.00419 ± 0.00004 at 121.57 nm and the waveplate with a thickness difference of 14.51 μm will work as a half-waveplate at Lyman-α wavelength [24].

The working principle of a half-waveplate is explained in Fig. 5.4 by a schematic drawing. Suppose a plane-polarized wave is normally incident on a

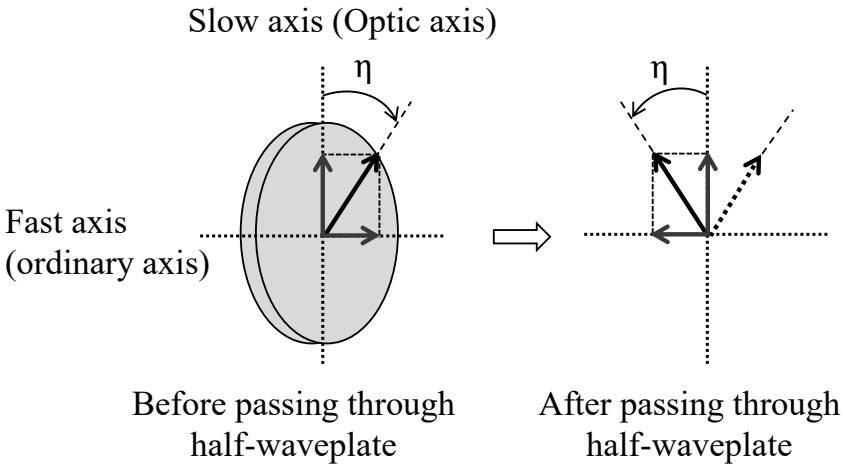

Fig. 5.4: Working principle of a half-waveplate

half-waveplate, and the plane of polarization is at an angle η with respect to the

slow axis (i.e., optic axis). The incident wave can be decomposed into components polarized along the fast axis and the slow axis. The component polarized along the fast axis travels with a speed $v_o = c/n_o$, while the component polarized along the slow axis travels with a speed $v_e = c/n_e$. As a result, the component polarized along the slow axis is retarded by one half-wave, i.e., by 180° in phase, after passing through the half-waveplate. This describes a plane-polarized wave, but making an angle η on opposite side of the slow axis. Thus, the original wave has been rotated by an angle 2η.

Use of half-waveplate in present experiment

In present experiment, the half-waveplate is placed just after the entrance slit and during the measurement it is continuously rotated in the clockwise direction as observed from the grating. The angle of the half-waveplate optic axis, denoted here as θ, is measured in the clockwise direction seen from the grating with respect to the vertical axis.

The incident beam coming from the LHD plasma includes Lyman-α light linearly polarized at all directions. As mentioned earlier although the detector always receives a light linearly polarized in the vertical direction, the direction of the corresponding linearly polarized light at the emission location changes depending on the optic axis angle of the rotating half-waveplate. As illustrated in Fig. 5.5, for the optic axis at an angle θ, the light with polarization angle $\alpha = 2\theta$ is detected at the detector.

During measurement, the cycle time of Lyman-α line spectral observation is 50 ms with an exposure time of 16 ms, and the period of the half-waveplate rotation is 0.8 s. Under such conditions, linearly polarized light at every 45° angle is monitored. In this way by using the combination of a rotating half-waveplate and a polarization analyzer, the spectra of linearly polarized Lyman-α light at all angles have been obtained sequentially.

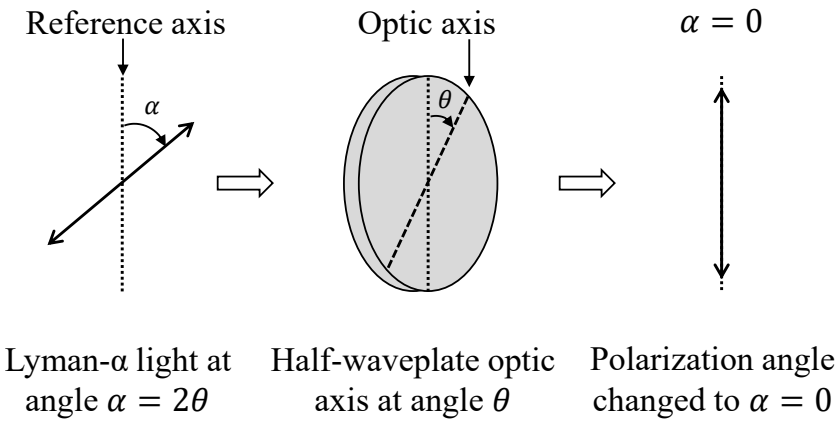

Fig. 5.5: Half-waveplate changes the plane of polarization

The system is also capable of acquiring spectra with better angular resolution, i.e., with smaller step size of angle, by increasing the half-waveplate rotation period. Depending on the steady-state phase duration of the discharge, period of the half-waveplate rotation is decided.

5.3 Viewing geometry of the spectrometer

Here we focus on the LHD discharge with shot no. 138800, which is an electron cyclotron heated (ECH) discharge. For this discharge the magnetic axis is at $R_{\mathrm{ax}} = 3.75\,\mathrm{m}$ and the magnetic field strength is 2.64 T at the magnetic axis. Figure 5.6 shows the schematic drawing of the poloidal cross-section at horizontally-elongated plasma position of LHD with the magnetic surfaces for the magnetic axis at $R_{\mathrm{ax}} = 3.75\,\mathrm{m}$. The line of sight of the spectrometer is shown by a dashed line.

The previous studies on hydrogen line emission from the LHD plasma suggests that the dominant hydrogen emission locations can be approximated to be at $r_{\mathrm{eff}} = 0.67\,\mathrm{m}$ [49, 50] where, r_{eff} is the effective minor radius of the plasma. In Fig. 5.6 the magnetic surface with $r_{\mathrm{eff}} = 0.67\,\mathrm{m}$ is shown using a solid line on the poloidal cross section. From this result it is clear that on the spectrometer line of sight, the Lyman-α line is emitted at both the inboard and outboard sides

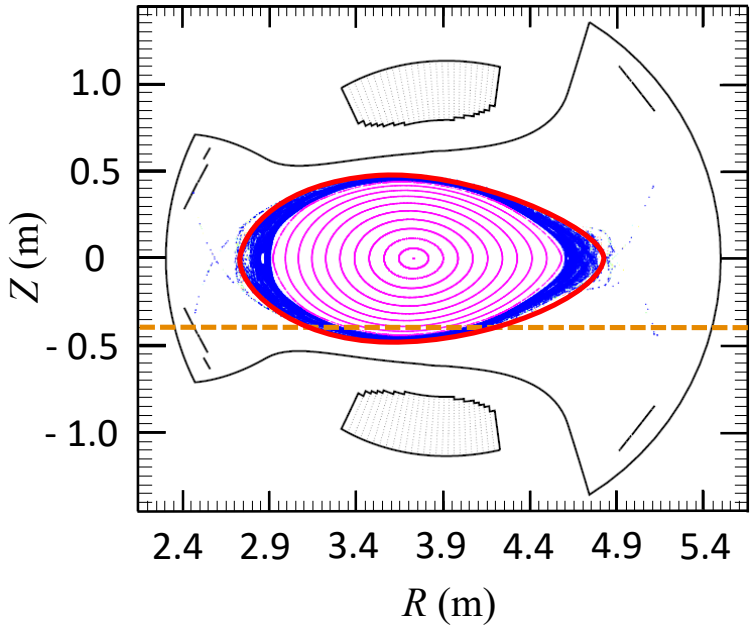

Fig. 5.6: Schematic drawing of poloidal cross section at horizontally-elongated plasma of LHD with the magnetic surfaces for the magnetic axis at $R_{ax} = 3.75\,\mathrm{m}$. The line of sight of spectrometer is indicated by a dashed line.

of the device and the intensity observed by the spectrometer is the sum of these intensities.

5.4 Evaluation of polarization degree

The present measurement has been made for an ECH discharge with shot no. 138800, and having a steady-state phase of about 1 s. The main parameters of the discharge, namely, stored energy (W_P in kJ), total ECH power (in MW), electron temperature at magnetic axis (T_{e0} in keV) line averaged electron density ($\bar{n}_e$ in m^{-3}) at magnetic axis, and H_α signal in arbitrary units, are shown in Fig. 5.7.

In present measurement the cycle time of Lyman-α observation, which is determined by CCD output signal, is 50 ms with the exposure time of 16 ms. Fig. 5.8 shows the CCD output signal for shot no. 138800 during the time $t = 4.2\,\mathrm{s}$ to $t = 4.5\,\mathrm{s}$. In this figure the high signal represents exposure duration. As discussed in Sec. 5.2.3 spectra of linearly polarized Lyman-α light from the edge LHD plasma

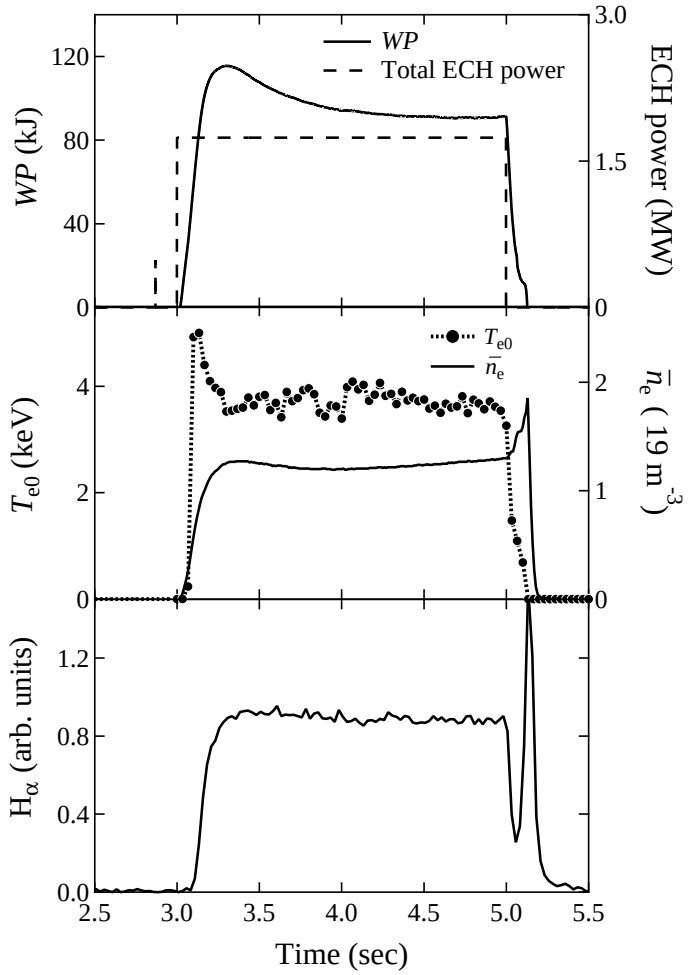

Fig. 5.7: Main parameters of shot no. 138800: (a) stored energy (W_P in kJ) and total ECH power (in MW) (b) electron temperature at magnetic axis (T_{e0} in keV) and line averaged electron density ($\bar{n}_e$ in m^{-3}) at magnetic axis (c) H_α signal in arbitrary units.

have been acquired at every 45° angle with the polarization measurement system. An example of a spectrum acquired during the steady-state time period of the discharge is shown in Fig. 5.9, where both the hydrogen and deuterium lines can be seen.

The intensity integrated over the entire wavelength range shown in Fig. 5.9 for each time frame has been calculated, and the result is plotted as a function of time, t, with circles in Fig. 5.10. The time, t, in this figure corresponds to the middle of exposure duration.

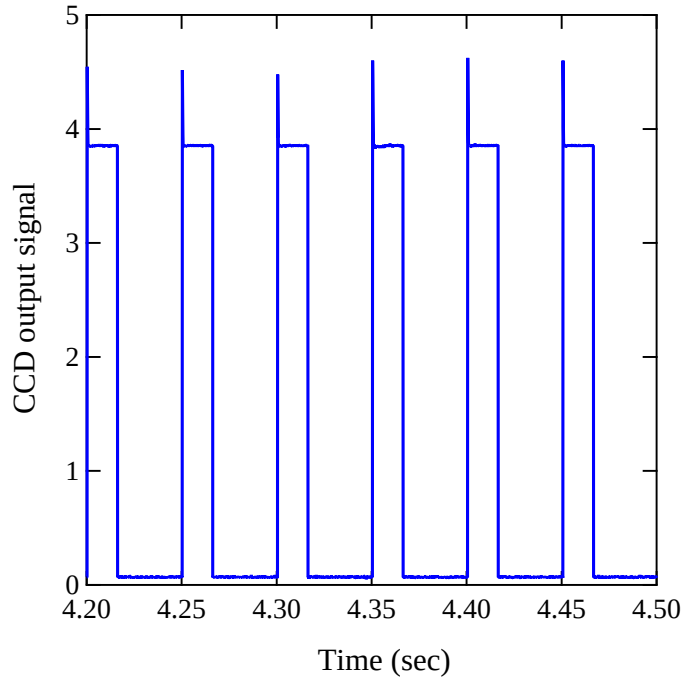

Fig. 5.8: CCD output signal for shot no. 138800.

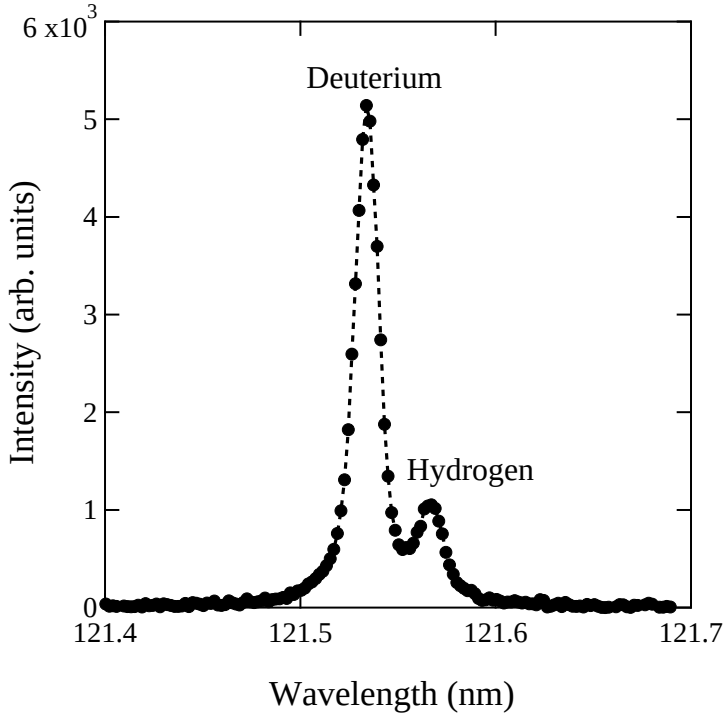

Fig. 5.9: Typical background subtracted spectrum at 121.56 nm obtained during steady-state phase of an LHD discharge showing hydrogen and deuterium peaks.

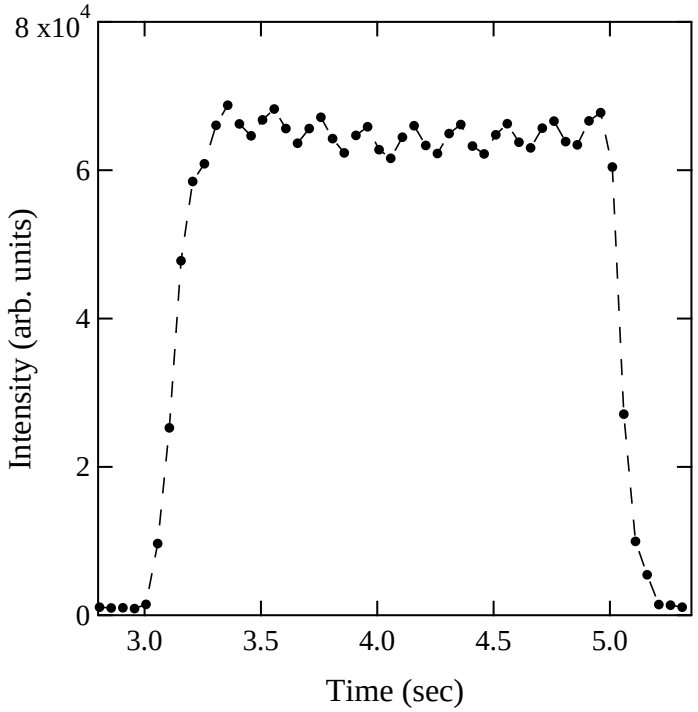

Fig. 5.10: Temporal profile of the Lyman-α line for shot no. 138800

As mentioned earlier, in this experiment the polarization angle is measured in the clockwise direction as seen from the grating with reference to the vertical axis. In Fig. 5.11 the polarization angle of observed light is plotted as a function of time with the dashed-dotted line along with the experimental intensity with open circles. The experimental intensity shows a modulation, which is synchronized with a half-waveplate rotation period. This result clearly indicates that the observed Lyman-α line is polarized. Since the light intensities at polarization angles α and $180° + \alpha$ is not distinguishable, as can be seen from Fig. 5.5, the intensity profile is the same for polarization angles from 0° to 180° and from 180° to 360°. Due to this fact, for simplicity, in Fig. 5.11 the polarization angle is plotted only in the range from 0° to 180°.

For evaluating the polarization degree, the steady-state time phase of the discharge, i.e., from $t = 3.85\,\mathrm{s}$ to $t = 4.65\,\mathrm{s}$, is considered so that it can be assumed that the polarization state is not changed during this time period. This time duration with $\Delta t = 0.8\,\mathrm{s}$ corresponds to one complete rotation of the

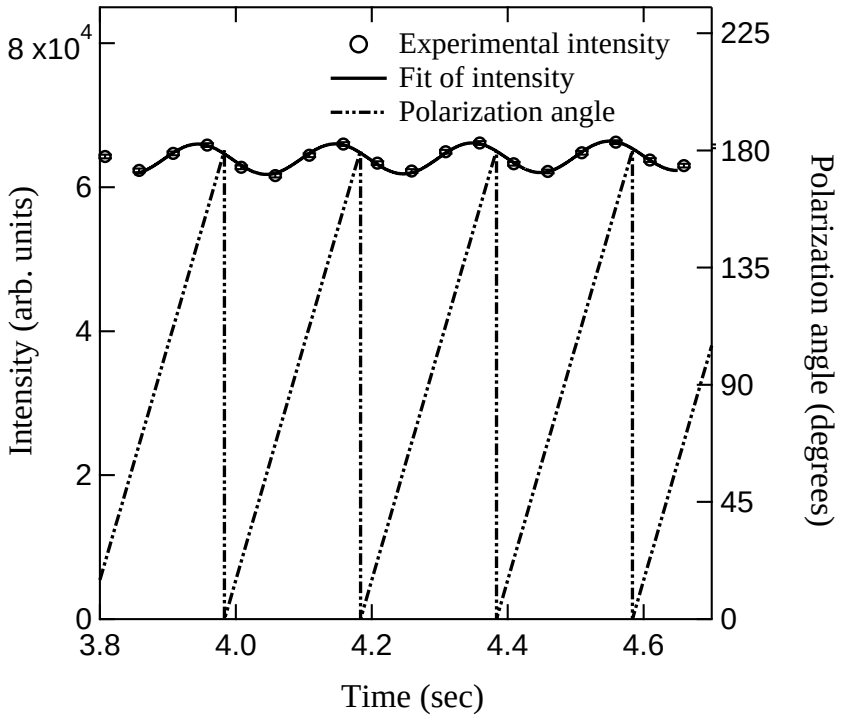

Fig. 5.11: Temporal profile of Lyman-α line is shown with open circles and solid line represents the fitted curve. The polarization angle is shown with the dashed-dotted line.

half-waveplate.

In the present case we define the polarization degree as

$$P = \frac{I_{\max} - I_{\min}}{I_{\max} + I_{\min}}, \tag{5.1}$$

where $I_{\max}$ and $I_{\min}$ are the minimum and maximum intensities in the temporal profile, respectively.

The least-squares fitting is performed on the temporal variation of the intensity, $I(t)$, with a function

$$I(t) = f(t)[1 + P\sin(\omega t + \theta)], \tag{5.2}$$

where $f(t)$ represents the global intensity variation, which is here expressed by a second order polynomial, P is the magnitude of the polarization degree, and θ is

the phase offset. In the present case $\omega = 10\,\pi$. To perform fitting of the temporal variation, a code has been developed in which the profile is first fitted with the second order polynomial function and then the obtained parameters are used as initial guess for the final fitting to get accurate fitting results.

5.5 Results

As mentioned in the previous section, the least-squares fitting has been performed on the temporal variation of intensity for evaluating the polarization degree. As a result of fitting, $P = 0.033$ is obtained. The fitting result is shown with a solid line in Fig. 5.11.

The error in the measured intensity is very small and the actual uncertainty in the present measurement is mainly due to unsteadiness of the discharge which is recognized as the discrepancy of the measured intensities from the fitted curve in Fig. 5.11. The root mean squared error of the measured intensity with respect to the fitted curve is evaluated and given as the error bars in Fig. 5.11. By using the value of the uncertainty in measured intensities, the uncertainty in the polarization degree has been evaluated and the final value of polarization degree is 0.033 ± 0.004.

CHAPTER 6

Study of Lyman-α polarization in LHD

The PACR model for Lyman-α and the polarization measurement system on LHD have been described in previous chapters. In this chapter following results of the study of polarization in Lyman-α from the edge LHD plasma have been presented:

- PACR model results applicable to measurements in LHD
- Phase analysis of the intensity profile
- Dependence of polarization degree on electron density
- Evaluation of anisotropy in the EVDF using the PACR model results
- Dependence of anisotropy on electron density and temperature

6.1 PACR model results applicable to measurements in LHD

The results obtained in Sec. 4.2 correspond to cases when the angle of observation is 90°, i.e., emitted Lyman-α radiation is observed at 90° with respect to the quantization axis (magnetic field direction in present case). However, in present

experiments in LHD the angle of observation may be different from 90°. Therefore, results of the theoretical model can not be used directly and influence of the angle of observation on final result must be taken into account.

6.1.1 Viewing geometry and calculation of angle of observation

The hydrogen Lyman-α line at 121.57 nm has been observed from edge region of the LHD plasma with a 3 m normal incidence VUV spectrometer [44, 45]. Figure 6.1 illustrates a schematic drawing of a horizontally-elongated cross section of LHD along with magnetic surfaces for the magnetic axis at $R_{\mathrm{ax}} = 3.75\,\mathrm{m}$. The variables

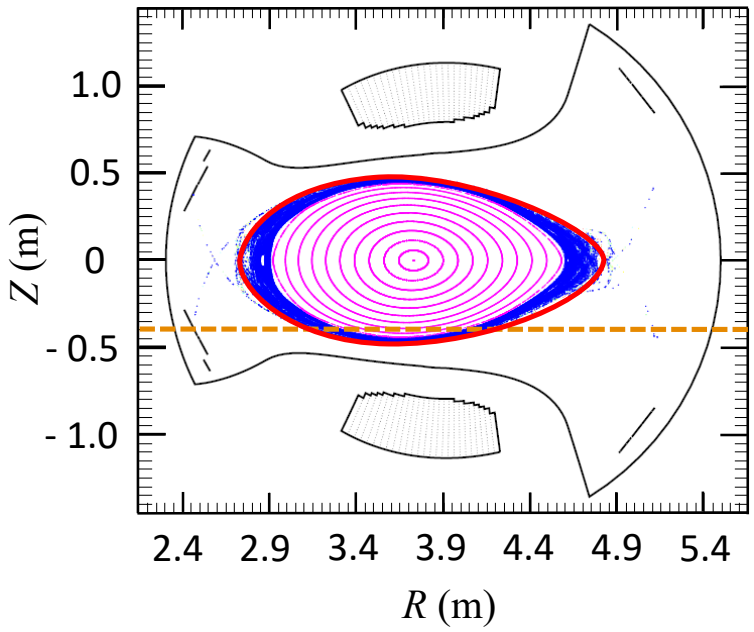

Fig. 6.1: Schematic drawing of magnetic surfaces for the magnetic axis at $R_{\mathrm{ax}} = 3.75\,\mathrm{m}$ along with the spectrometer line of sight, indicated with a dashed line. The magnetic surface with $r_{\mathrm{eff}} = 0.67\,\mathrm{m}$ is highlighted with a solid line.

of Z and R are the vertical and the radial coordinates, respectively. Although the observation range of spectrometer is 15 cm wide in Z coordinate, here we consider only $Z = -0.4\,\mathrm{m}$ position as the main line of sight for simplicity, and it is shown with a dashed line.

According to previous studies conducted on the LHD plasma, hydrogen emission is located outside the confined region in LHD plasma and it can be approximated that dominant emission locations are at $r_{\mathrm{eff}} = 0.67\,\mathrm{m}$ in the LHD plasma [49, 50]. Here, r_{eff} refers to the effective minor radius of the plasma. The magnetic surface with $r_{\mathrm{eff}} = 0.67\,\mathrm{m}$ is highlighted with a solid line in Fig. 6.1. From this result, it is clear that the Lyman-α is emitted at both the inboard and outboard sides of the device, and intensity observed by the spectrometer is sum of these two intensities.

Figure 6.2 shows the angles θ, ζ, and the angle of observation, denoted here as γ. The inclination angle θ represents the angle of the magnetic field $\boldsymbol{B}$ with respect to the z direction. The azimuth angle ζ shows the angle between the projection of the magnetic field $\boldsymbol{B}$ onto the $\phi - r$ plane and the ϕ direction. The angle of observation γ can be obtained from the inclination angle θ and the

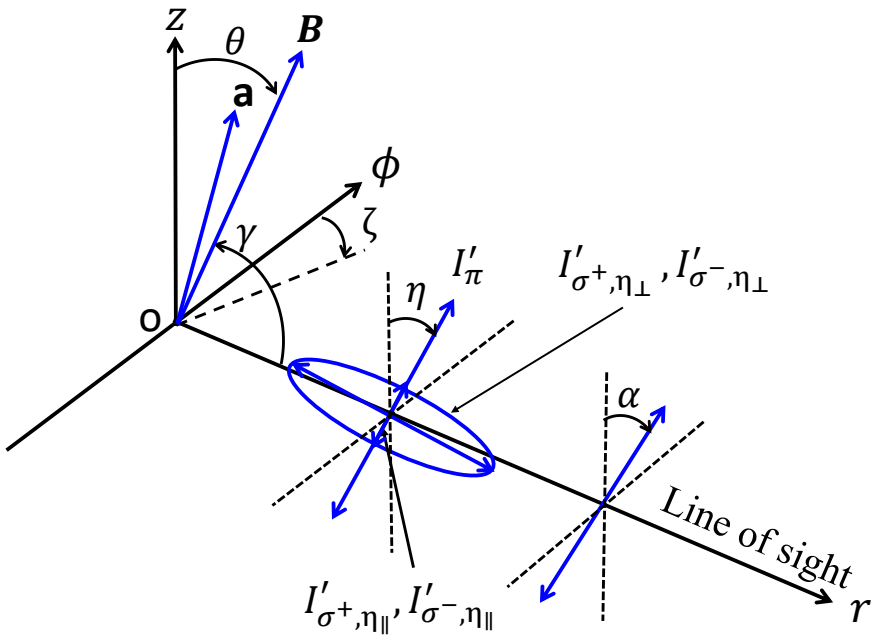

Fig. 6.2: The definitions of angles of the magnetic field with respect to the line of sight. θ and ζ are the inclination and azimuth angles of the magnetic field vector $\boldsymbol{B}$, respectively. γ is the angle between the line of sight and $\boldsymbol{B}$. $\mathbf{a}$ is the unit vector in the same direction as the projection of $\boldsymbol{B}$ onto the $\phi - z$ plane and η is the angle of $\mathbf{a}$ with respect to the z axis.

azimuth angle ζ using the following relation

$$\cos\gamma = \sin\theta\ \sin\zeta. \tag{6.1}$$

In LHD, the magnetic field is determined accurately by the coil currents. The present discussion focuses on the steady-state time period of an electron cyclotron heated discharge with shot no. 138800, in which the plasma axis is at $R_{\rm ax} = 3.75\,\mathrm{m}$. The parameters of the magnetic field vector $\boldsymbol{B}$ at $Z = -0.4\,\mathrm{m}$ are plotted in Fig. 6.3 (a)–(c).

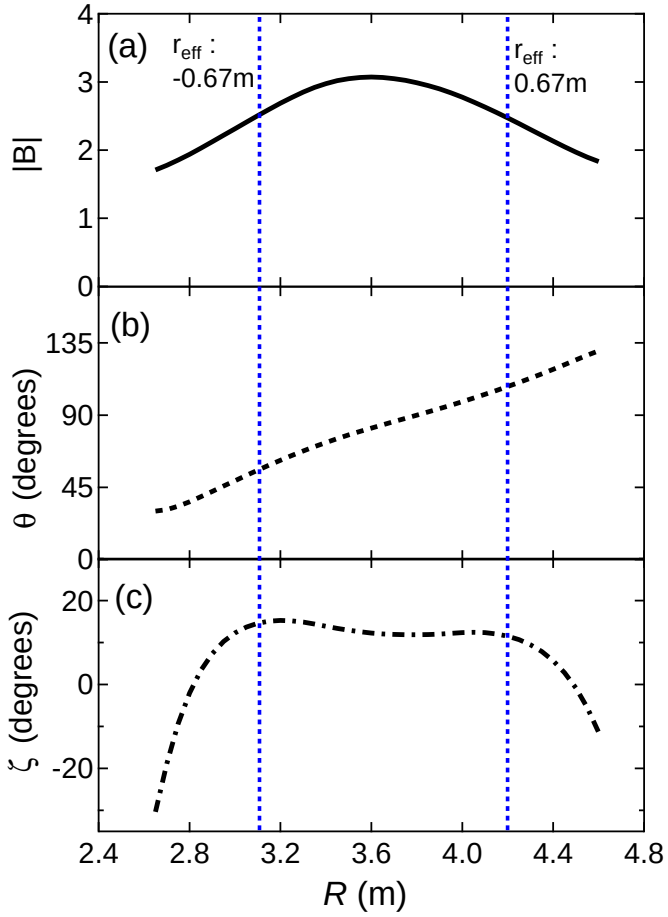

Fig. 6.3: Magnetic field parameters for shot no. 138800 at $Z = -0.4\,\mathrm{m}$: (a) the variation of the magnetic field strength, (b) the inclination angle θ of the magnetic field with respect to the z direction, and (c) the azimuth angle ζ which is the angle between the projection of the magnetic field vector onto the $\phi - r$ plane and the ϕ direction. The $r_{\rm eff} = \pm 0.67\,\mathrm{m}$ locations at the inboard side and the outboard side are indicated with the vertical dashed lines.

Using available data directions and magnitudes of the magnetic field vectors at the emission locations ($r_{\rm eff} = \pm 0.67\,{\rm m}$) on the spectrometer line of ($Z = -0.4\,{\rm m}$), have been determined. The $\boldsymbol{B}$ vectors point upward and downward at the inboard side and the outboard side, respectively. The value of the angle of observation is found to be 77.5° and 79° at the Lyman-α emission locations at the inboard and outboard sides, respectively.

6.1.2 Derivation of the intensity observed from the line of sight

The Lyman-α line is assumed to be emitted at the position O where the magnetic field $\boldsymbol{B}$ is directed as shown in Fig. 6.2. I_π refers to the linearly polarized light parallel to $\boldsymbol{B}$. I_{σ^+} and I_{σ^-} are the circularly polarized light in the direction perpendicular to $\boldsymbol{B}$. For a particular angle of observation γ, we define a unit vector $\boldsymbol{a}$ which is in the same direction as the projection of $\boldsymbol{B}$ onto the $\phi - z$ plane. η is the angle of $\boldsymbol{a}$ with respect to the z axis.

The π component is observed as the light linearly polarized in the direction of $\mathbf{a}$. We denote its intensity as I'_π

$$I'_\pi = I_\pi \sin^2\gamma. \tag{6.2}$$

The σ^+ component gives rise to the intensities in both the parallel and perpendicular directions to $\mathbf{a}$: $I'_{\sigma^+,\eta_\parallel}$ and $I'_{\sigma^+,\eta_\perp}$, respectively.

$$\begin{aligned} I'_{\sigma^+} &= I'_{\sigma^+,\eta_\parallel} + I'_{\sigma^+,\eta_\perp} \\ &= \frac{1}{2}(\cos^2\gamma + 1) I_{\sigma^+}, \end{aligned} \tag{6.3}$$

and the σ^- component gives rise to the intensities

$$\begin{aligned} I'_{\sigma^-} &= I'_{\sigma^-,\eta_\parallel} + I'_{\sigma^-,\eta_\perp} \\ &= \frac{1}{2}(\cos^2\gamma + 1) I_{\sigma^-}. \end{aligned} \tag{6.4}$$

In the experiments on LHD, a half-waveplate specially designed for Lyman-α is rotated to monitor the linearly polarized light emission at all angles. Here, we define the angle of the linearly polarized light as the polarization angle, denoted here as α. The intensity observed at the polarization angle α consists of the π component

$$\begin{aligned} I_{\mathrm{o},\pi} &= I'_\pi \cos^2(\eta - \alpha) \\ &= \sin^2\gamma \cos^2(\eta - \alpha) I_\pi \end{aligned} \tag{6.5}$$

and the σ^+ and σ^- components

$$\begin{aligned} I_{\mathrm{o},\sigma^+} &= I'_{\sigma^+,\eta_\parallel} \cos^2(\eta - \alpha) + I'_{\sigma^+,\eta_\perp} \sin^2(\eta - \alpha) \\ &= \frac{1}{2}\Big\{ \cos^2\gamma \cos^2(\eta - \alpha) + \sin^2(\eta - \alpha) \Big\} I_{\sigma^+} \end{aligned} \tag{6.6}$$

$$\begin{aligned} I_{\mathrm{o},\sigma^-} &= I'_{\sigma^-,\eta_\parallel} \cos^2(\eta - \alpha) + I'_{\sigma^-,\eta_\perp} \sin^2(\eta - \alpha) \\ &= \frac{1}{2}\Big\{ \cos^2\gamma \cos^2(\eta - \alpha) + \sin^2(\eta - \alpha) \Big\} I_{\sigma^-} \end{aligned} \tag{6.7}$$

The angle η is related to θ and ζ as

$$\tan\eta = \tan\theta \ \cos\zeta \tag{6.8}$$

It should be noted here that the angles θ and η are calculated with respect to the $+z$ axis and the azimuth angle ζ is calculated with respect to the $+\phi$ axis. The total observed intensity at the polarization angle α is given as

$$I_{\mathrm{obs}} = I_{\mathrm{o},\pi} + I_{\mathrm{o},\sigma^+} + I_{\mathrm{o},\sigma^-}. \tag{6.9}$$

We assume axisymmetry with respect to the magnetic field direction. Therefore, in this case $I_{\sigma^+} = I_{\sigma^-} \equiv I_\sigma$. Thus, the final expression for $I_{\rm obs}$ can be given as

$$I_{\rm obs} = \sin^2\gamma\ \cos^2(\eta-\alpha)\, I_\pi\ + \left\{ \cos^2\gamma\ \cos^2(\eta-\alpha) + \sin^2(\eta-\alpha) \right\} I_\sigma. \quad (6.10)$$

The polarization degree is defined here with respect to the unit vector **a** and it is given as

$$P = \frac{I_\parallel - I_\perp}{I_\parallel + I_\perp}, \quad (6.11)$$

where $I_\parallel$ and $I_\perp$ are intensities observed in the directions parallel and perpendicular to the unit vector **a**. In Eq. (6.10) when $\alpha = \eta$, intensity $I_\parallel$ is observed and when $\alpha = \eta + \pi/2$, intensity $I_\perp$ is observed. The obtained intensities are given by the following equations:

$$I_\parallel = I_\pi\ \sin^2\gamma + I_\sigma\ \cos^2\gamma, \quad (6.12)$$

$$I_\perp = I_\sigma. \quad (6.13)$$

Equation (6.11) can be rewritten as

$$P = \frac{(I_\pi\ \sin^2\gamma + I_\sigma\ \cos^2\gamma) - (I_\sigma)}{(I_\pi\ \sin^2\gamma + I_\sigma\ \cos^2\gamma) + (I_\sigma)} \quad (6.14)$$

$$= \frac{\left(\frac{I_\pi}{I_\sigma}\ \sin^2\gamma + \cos^2\gamma\right) - 1}{\left(\frac{I_\pi}{I_\sigma}\ \sin^2\gamma + \cos^2\gamma\right) + 1} \quad (6.15)$$

In above equation the value of I_π/I_σ has been obtained from the PACR model results for $\gamma = 90°$. For observation angle $\gamma = 77.5°$, the model results have been obtained and shown in Fig. 6.4.

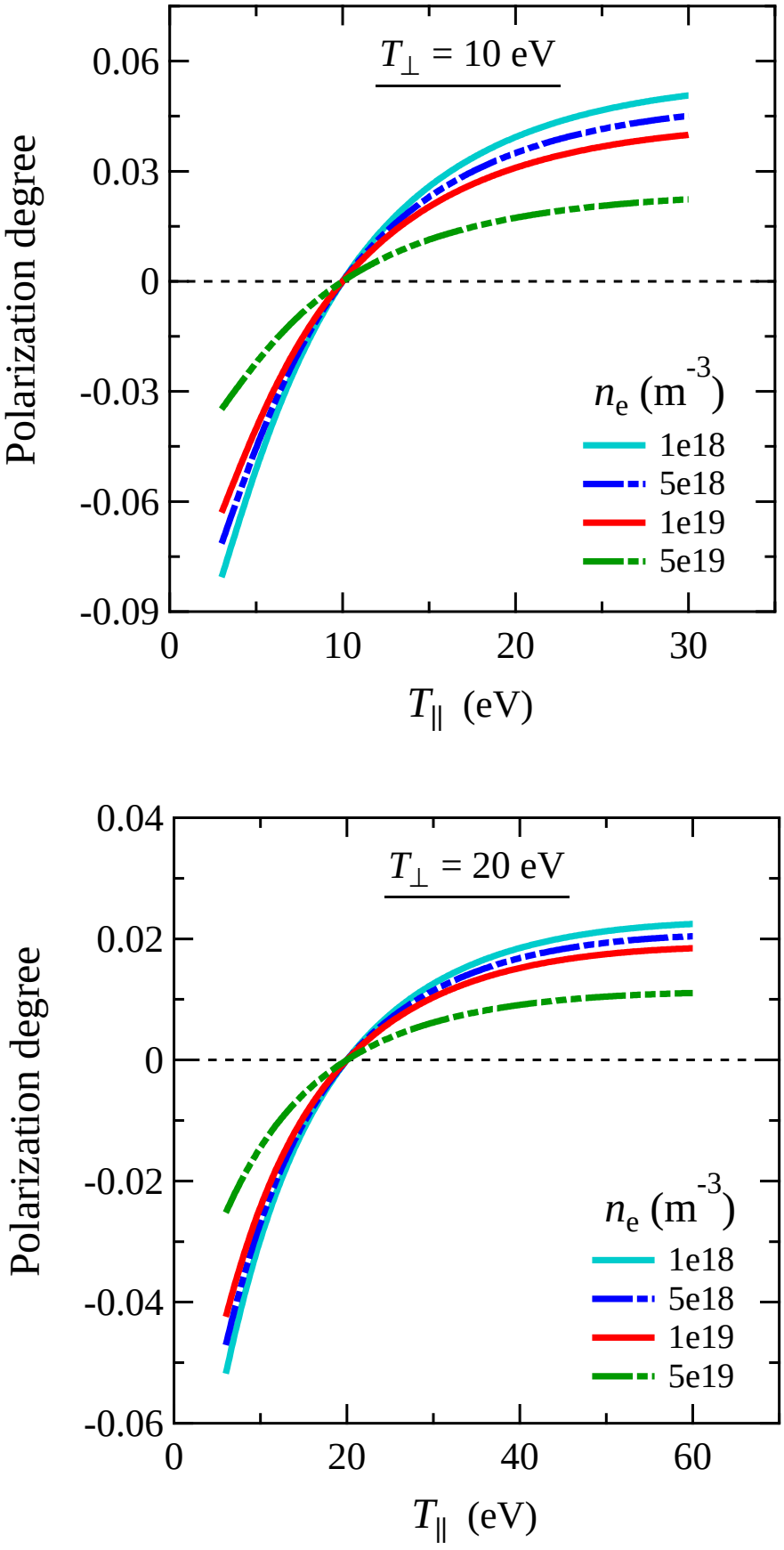

Fig. 6.4: Polarization degree calculated for $T_\perp = 10\,\mathrm{eV}$ and $20\,\mathrm{eV}$ with $\gamma = 77.5°$

6.2 Comparison of polarization degrees evaluated for $\gamma = 90°$ and 77.5°

Figure 6.5 shows the comparison between polarization degrees evaluated for $\gamma = 90°$ and 77.5° with $T_\perp = 10\,\mathrm{eV}$. The comparison is given for $n_\mathrm{e} = 1 \times 18\,\mathrm{m}^{-3}$ and $1 \times 19\,\mathrm{m}^{-3}$. The results indicate that there is a very small difference in polarization degree evaluated for these two observation angles.

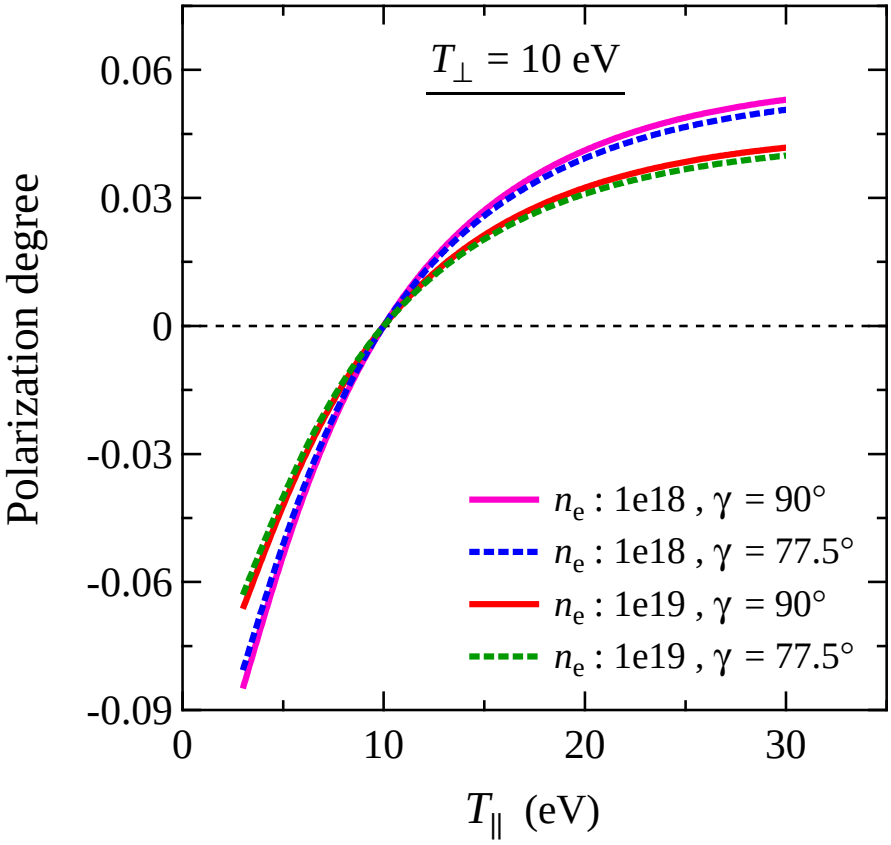

Fig. 6.5: Comparison between polarization degrees evaluated for $\gamma = 90°$ and 77.5° with $T_\perp = 10\,\mathrm{eV}$

The similar comparison has been made for $T_\perp = 20\,\mathrm{eV}$ and is illustrated in Fig. 6.6. Here also we have considered $n_\mathrm{e} = 1 \times 18\,\mathrm{m}^{-3}$ and $1 \times 19\,\mathrm{m}^{-3}$.

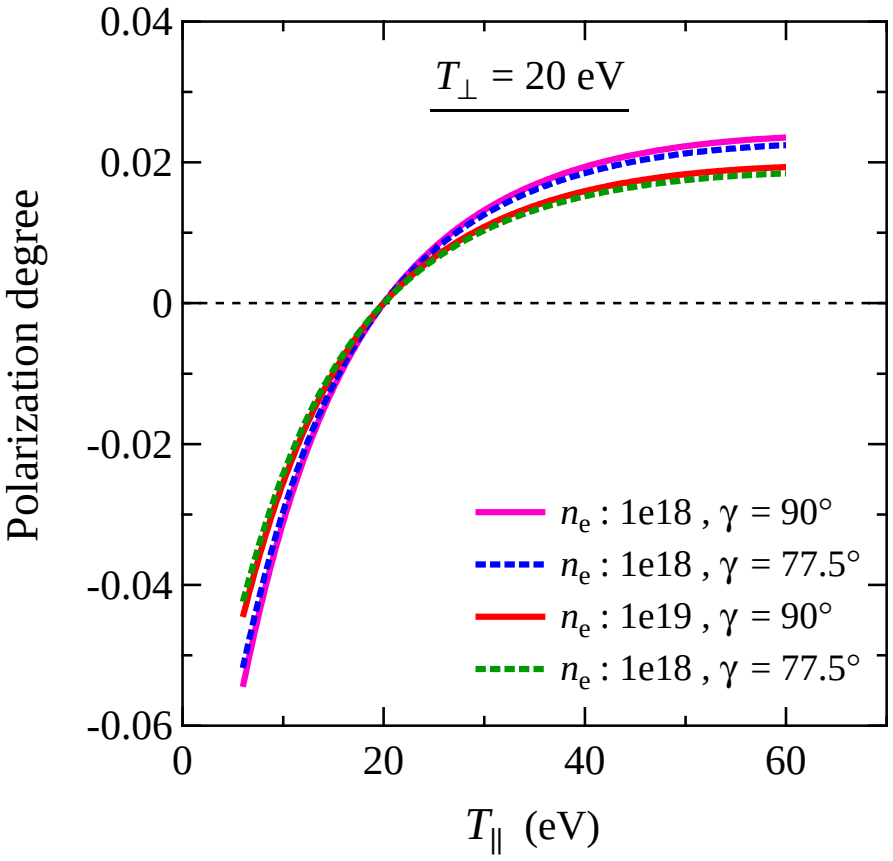

Fig. 6.6: Comparison between polarization degrees evaluated for $\gamma = 90°$ and 77.5° with $T_\perp = 20\,\mathrm{eV}$

6.3 Phase analysis of the intensity profile

This discussion is focused on shot no. 138800 of LHD. Figure 6.7 shows the temporal profile of Lyman-α line with the fit of intensity. The variation of polarization angle, denoted as α, with time is also shown.

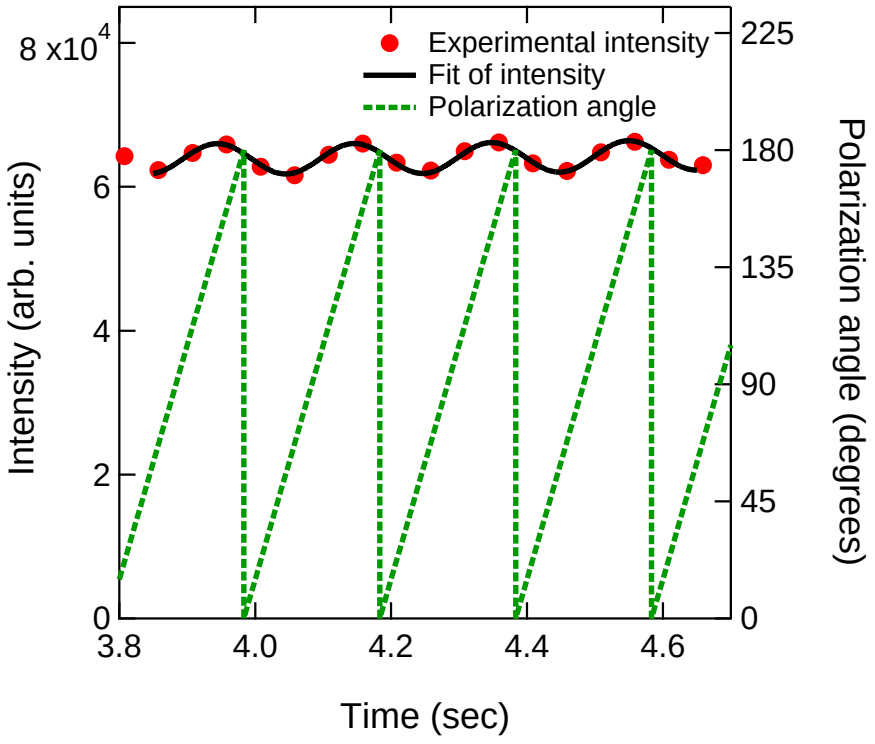

Fig. 6.7: Temporal profile of Lyman-α line for shot no. 138800 is shown with circles and solid line represents the fitted curve. The polarization angle is shown with a dashed line.

Here we consider the time duration from $t = 3.98\,\mathrm{s}$ to $t = 4.18\,\mathrm{s}$ in which α is changed from 0° to 180° and the change in intensity with α is given in Fig. 6.8 for this time duration. This plot indicates that the minimum and maximum intensities are observed at $\alpha = 55.5°$ and $\alpha = 145.5°$, respectively. The aim of this phase analysis is to investigate that why at these two particular angles intensity shows minimum and maximum values.

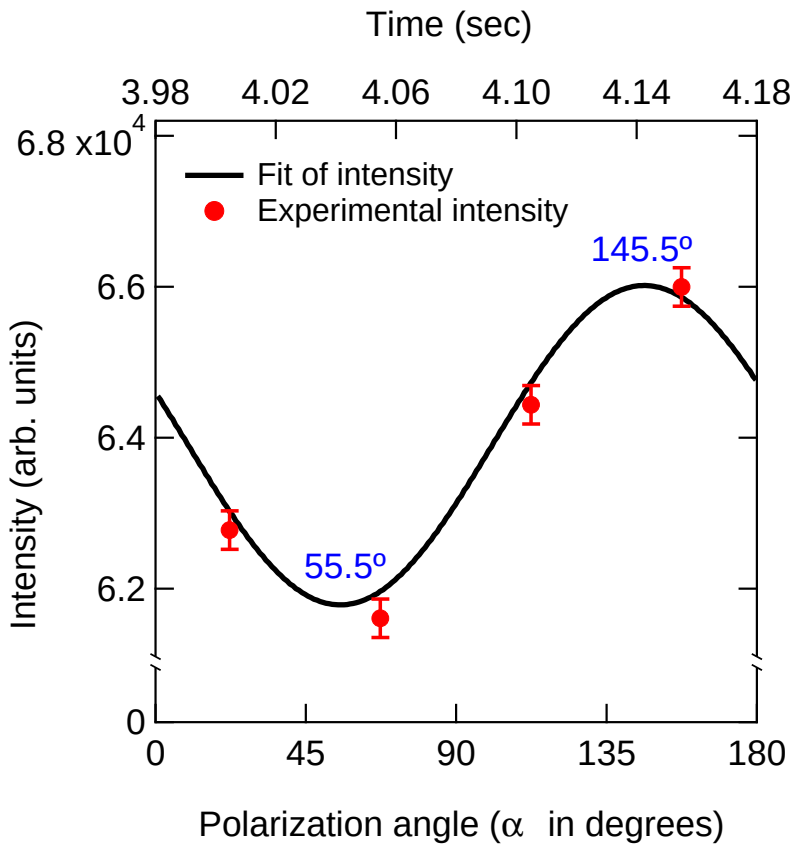

Fig. 6.8: Plot of Lyman-α intensity vs. polarization angle, α. The minimum and maximum intensities are observed at $\alpha = 55.5°$ and $\alpha = 145.5°$, respectively.

From such investigation, following information can be inferred:

- Relation between the magnetic field direction and intensity profile
- Dominant Lyman-α emission location

As it can be seen that from Fig. 6.1, on the line of sight there are two emission locations. The experimental intensity consists of Lyman-α emission from both the inboard and outboard sides of plasma and it is not possible to obtain their individual contributions in the experimental intensity. However, using Eq. (6.10) it is possible to generate synthetic profiles for the emission at the inboard and outboard sides separately. Equation (6.10) can be rewritten as

$$\frac{I_{\rm obs}}{I_\pi} = \sin^2\gamma\,\cos^2(\eta-\alpha) + \left\{\cos^2\gamma\,\cos^2(\eta-\alpha) + \sin^2(\eta-\alpha)\right\}\frac{I_\sigma}{I_\pi}. \qquad (6.16)$$

From Eq. (6.15), the factor $\frac{I_\sigma}{I_\pi}$ is derived to be

$$\frac{I_\sigma}{I_\pi} = \frac{1-P}{1+\left\{P\,(1+\cos^2\gamma)/(\sin^2\gamma)\right\}}, \tag{6.17}$$

where P is the experimentally observed polarization degree. For the shot no. 138800, as explained in Sec. 5.5, $P = 0.033$. It should be noted here that experimentally we can measure the magnitude of P and its value can be positive or negative. By substituting the value of $\frac{I_\sigma}{I_\pi}$ from Eq. (6.17), Eq. (6.16) becomes,

$$\frac{I_{\rm obs}}{I_\pi} = \sin^2\gamma\,\cos^2(\eta-\alpha) + \left\{\cos^2\gamma\,\cos^2(\eta-\alpha) + \sin^2(\eta-\alpha)\right\} \times \frac{1-P}{1+\left\{P\,(1+\cos^2\gamma)/(\sin^2\gamma)\right\}}. \tag{6.18}$$

By varying the value of α from 0° to 180° in above equation, we have generated synthetic profile for following cases:

- $P = 0.033$ and for inboard side ($\gamma = 77.5^\circ$ and $\eta = 56.1^\circ$)
- $P = 0.033$ and for outboard side ($\gamma = 79.0^\circ$ and $\eta = 108.5^\circ$)
- $P = -0.033$ and for inboard side ($\gamma = 77.5^\circ$ and $\eta = 56.1^\circ$)
- $P = -0.033$ and for outboard side ($\gamma = 79.0^\circ$ and $\eta = 108.5^\circ$)

The results are shown in Fig. 6.9 and 6.10 for $+P$ and $-P$, respectively, with the experimental profile. The values of γ have been obtained from Eq. (6.1) and of η from Eq. (6.8). The magnetic field values at $r_{\rm eff} = \pm 0.67\,$m on $Z = -0.4\,$m have been considered and shown in Fig. 6.3.

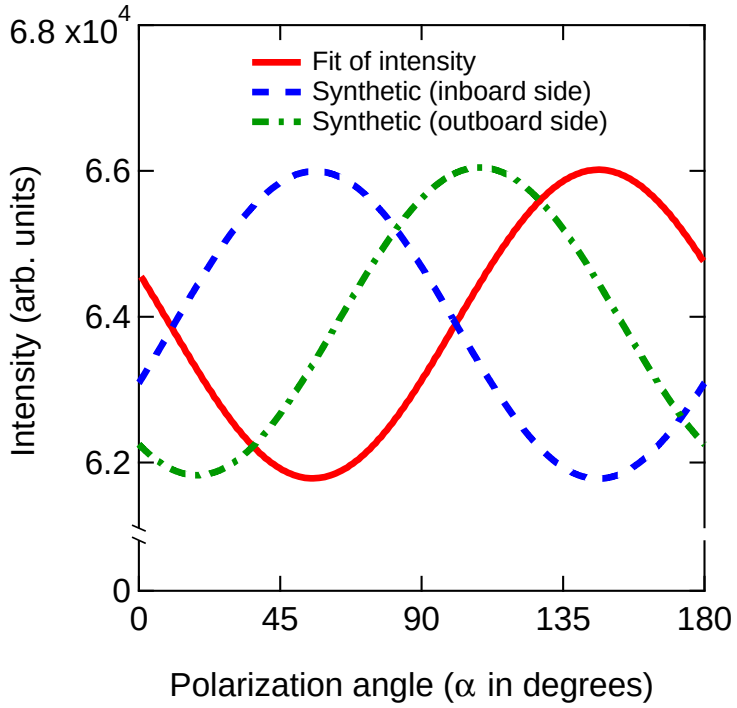

Fig. 6.9: Synthetic profiles of Lyman-α emission for $+P$ with the experimental profile

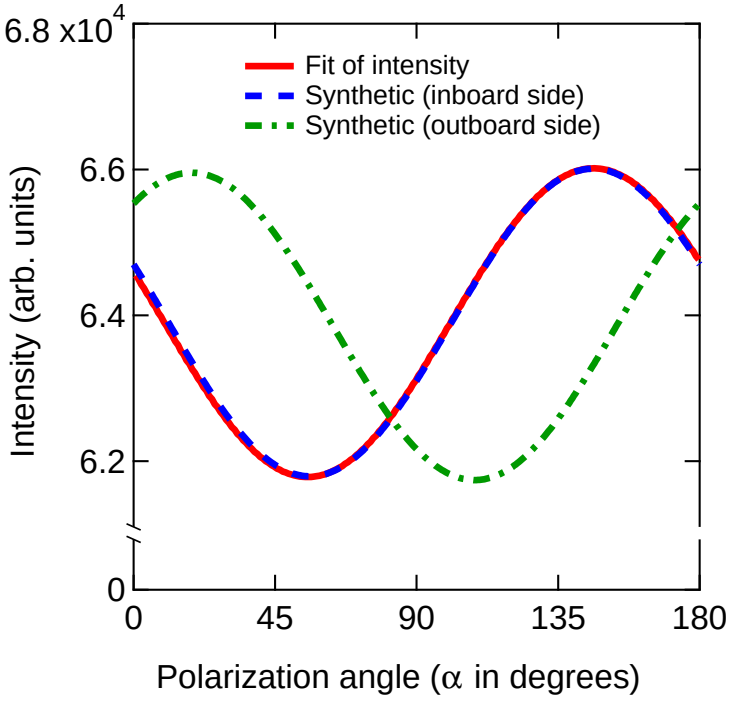

Fig. 6.10: Synthetic profiles of Lyman-α emission for $-P$ with the experimental profile

6.3.1 Conclusion from the phase analysis

It can be seen that synthetic profile for the inboard side emission agrees with the experimental profile only for the case when P is negative. From this observation following conclusion has been derived:

- In the experimental intensity dominant contribution to the polarized emission comes from the inboard side plasma. The intensity may include unpolarized emission from the outboard side plasma.
- The synthetic profile agrees only when P is negative indicates the value of experimentally measured polarization is negative. The results presented in Fig. 6.4 suggest that $-P$ implies that the electron temperature in the direction perpendicular to the magnetic field, denoted as $T_\perp$, is higher than electron temperature in the direction parallel to the magnetic field, denoted as $T_\parallel$.

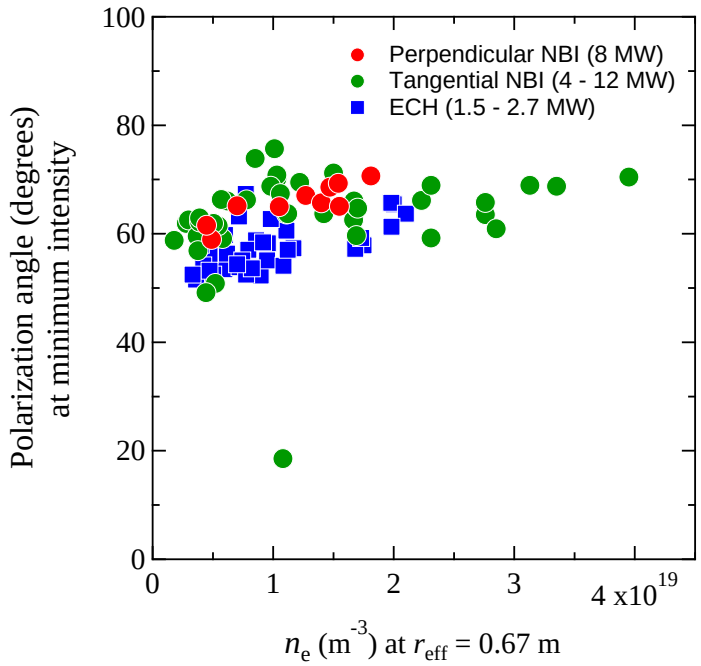

Fig. 6.11: Polarization angle in degrees at minimum intensity vs. n_e at r_{eff} for LHD discharges with different plasma parameters

Figure 6.11 shows polarization angle at minimum observed intensity vs. electron density at $r_{\mathrm{eff}} = 0.67\,\mathrm{m}$ for LHD discharges with different plasma parameters. This result indicates that for almost all discharges with various plasma conditions the variation in intensity with polarization angle, α, is similar to that for shot no. 138800 shown in Fig. 6.8. Therefore, above presented conclusion is valid for almost all LHD discharges with various plasma conditions.

6.4 Dependence of polarization degree on electron density

Sec. 5.4 describes evaluation of polarization degree with an example for shot no. 138800. Following similar method, the experimental polarization degree has been evaluated for many LHD discharges with different plasma conditions. Figure

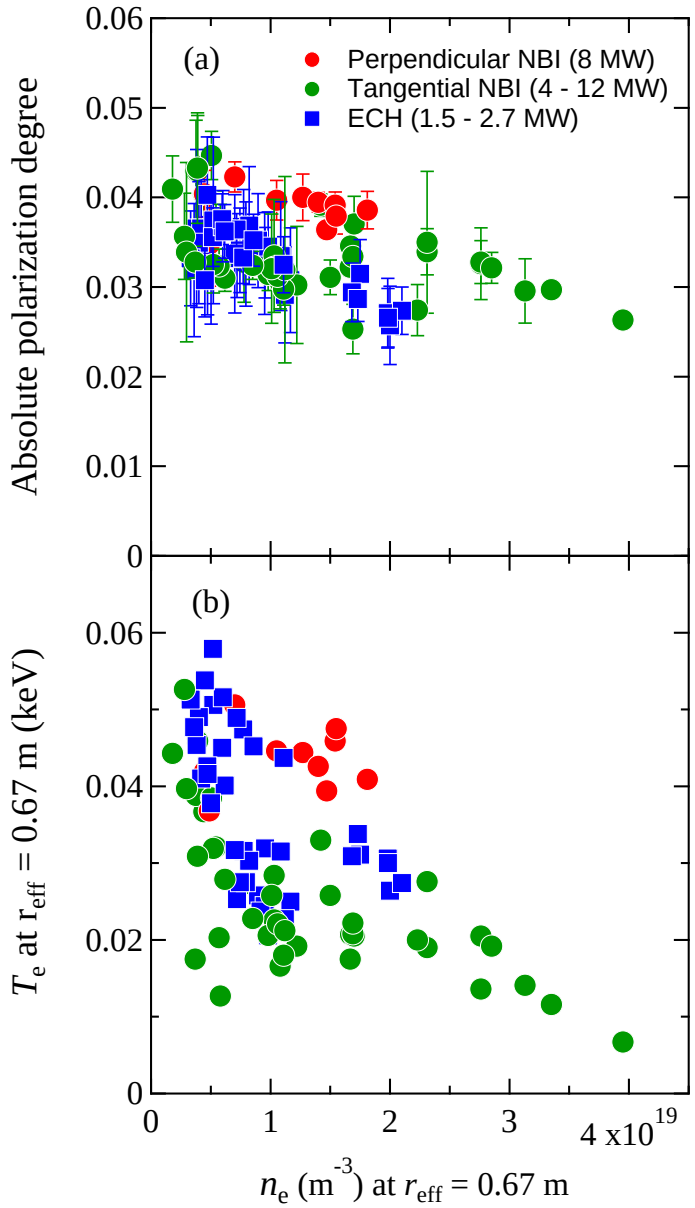

Fig. 6.12: (a) Dependence of polarization degree on n_e at $r_{eff} = 0.67\,\mathrm{m}$ (b) T_e at $r_{eff} = 0.67\,\mathrm{m}$ vs. n_e at $r_{eff} = 0.67\,\mathrm{m}$

6.12 (a) shows dependence of polarization degree on n_e at hydrogen emission location, i.e., at $r_{eff} = 0.67$ m and Fig. 6.12 (b) shows T_e at $r_{eff} = 0.67$ m vs. n_e at $r_{eff} = 0.67$ m. T_e and n_e have been obtained from Thomson scattering measurements in LHD. The discharges considered in present analysis includes ECH (Electron cyclotron heating) and NBI (Neutral Beam Injection) heated discharges. The NBI power varies from 4 MW–12 MW whereas ECH power during discharges are 1.5 MW and 2.7 MW. Heating power used during discharges vs. n_e at $r_{eff} = 0.67$ m are shown in Fig. 6.13.

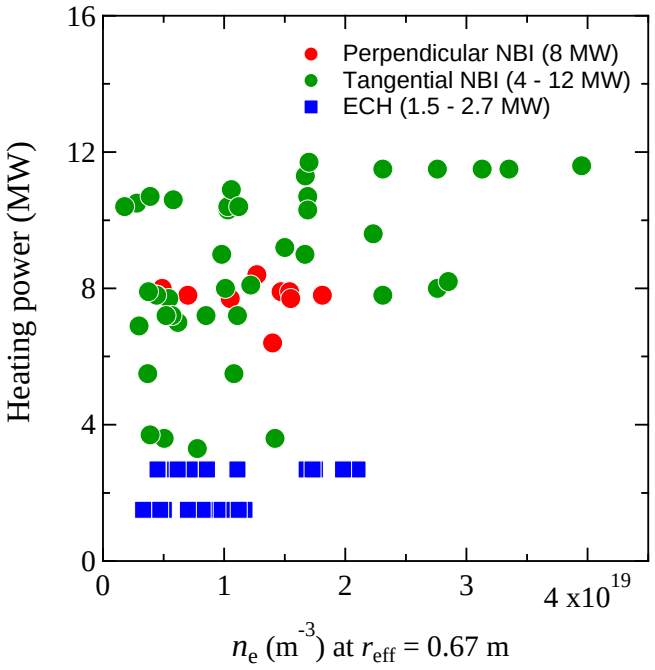

Fig. 6.13: Heating power vs. n_e at hydrogen emission location, i.e., at $r_{eff} = 0.67$ m

It is expected that polarization degree should decrease with increasing n_e due to following possibilities:

- the anisotropy in the EVDF itself reduces with increasing electron density
- collisional relaxation of population imbalance among the magnetic sublevels.

However, the result in Fig. 6.12 shows that polarization degree does not show any clear dependence on both n_e.

6.5 Evaluation of anisotropy in the EVDF

As mentioned in previous section T_e and n_e at hydrogen emission location in LHD, $r_{eff} = 0.67\,m$, can be obtained from Thomson scattering measurements. In other words, for each discharge considered in present study T_e and n_e at $r_{eff} = 0.67\,m$ are known and using these values it possible to evaluate the anisotropy from experimentally measured polarization degree. The important point to be noted here is that in LHD the measured electron temperature represents electron temperature in the direction perpendicular to the magnetic field. Therefore in present case, $T_e \equiv T_\perp$.

Evaluation of anisotropy is explained here with an example. Let's consider a case in which at $r_{eff} = 0.67\,m$, $T_\perp = 20\,eV$, $n_e = 1 \times 10^{19}\,m^{-3}$ and measured polarization degree is -0.03 (phase analysis results suggest that the value of measured polarization degree is negative). Polarization degree for these $T_\perp$ and n_e values has been calculated theoretically and it is shown in Fig. 6.14. From this

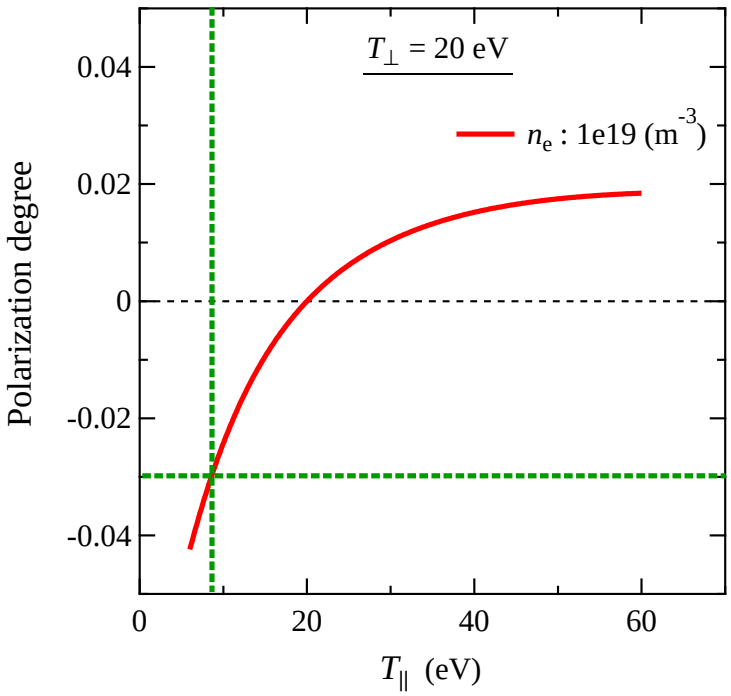

Fig. 6.14: Evaluation of temperature ratio using the PACR model results

theoretical result it can be seen that polarization degree of -0.03 corresponds to $T_{\parallel} = 8.56\,\mathrm{eV}$. Thus for this case temperature anisotropy can be obtained as $(T_{\perp} - T_{\parallel})/T_{\perp} = 0.57$.

6.6 Dependence of anisotropy on electron density and temperature

Following the method discussed in previous section anisotropy has been evaluated for many LHD discharges and it is shown in Fig. 6.15 as a function of n_{e} at $r_{\mathrm{eff}} = 0.67\,\mathrm{m}$. Although it is anticipated that with increasing n_{e} the anisotropy

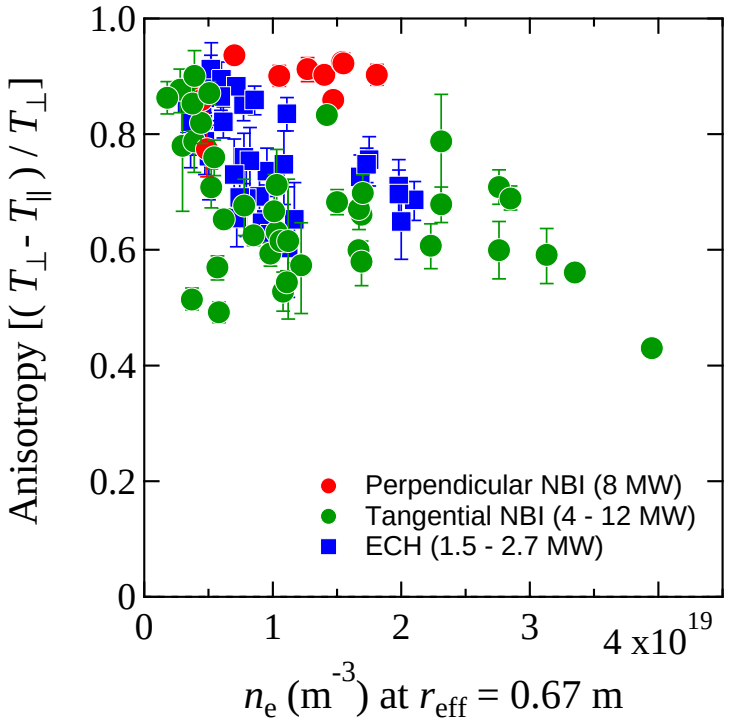

Fig. 6.15: Dependence of anisotropy on n_{e} at hydrogen emission location

should decrease due to the collisional relaxation, the result in Fig. 6.15 suggests that anisotropy has no clear dependence on n_{e}.

The dependence of anisotropy on T_e has also been investigated and it is given in Fig. 6.16. The result shown in Fig. 6.16 indicates that anisotropy demonstrates very clear depends on T_e, the anisotropy increases with increasing T_e. Increase in anisotropy with increasing T_e is expected due to the fact that increase

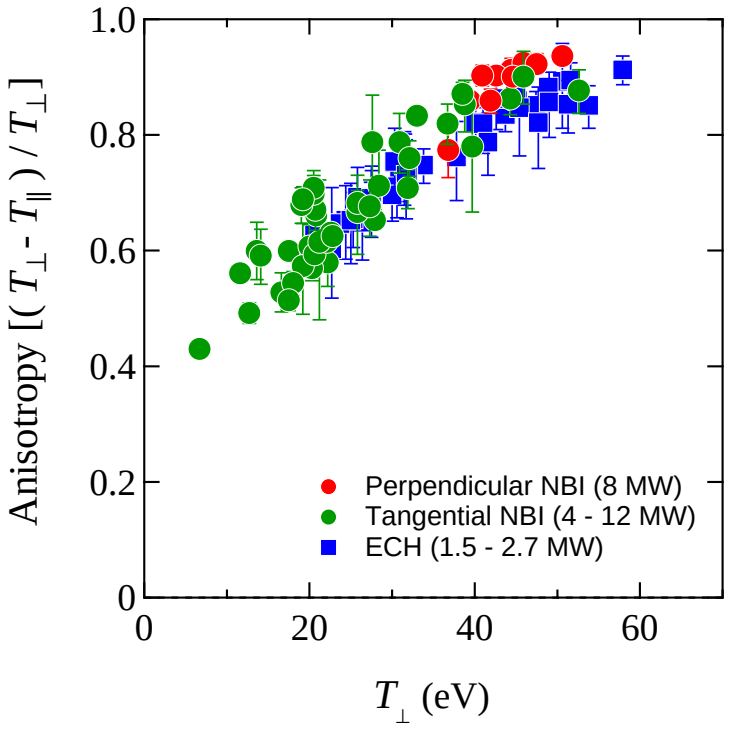

Fig. 6.16: Dependence of anisotropy on T_e at hydrogen emission location

in T_e reduces the collisionality which results in higher anisotropy.

By investigating dependence of anisotropy on n_e and T_e it can be concluded that anisotropy exhibits main dependence on T_e. The uncertainty in anisotropy in Figs. 6.15 and 6.16 originates from the uncertainty in polarization degree. In these figures error bars are not seen for some points because the error is smaller than the point size for them.

CHAPTER 7

Summary and conclusion

Measurement of anisotropy in the electron velocity distribution function (EVDF) is very important for understanding transport phenomena, equilibria, and current drive in a fusion plasma. There is a lack of research that actively investigates anisotropic EVDF in a plasma. Anisotropic electron-impact excitation creates non-uniform population distribution over the magnetic sublevels in a state and the subsequent emission is polarized. Thus, plasma polarization spectroscopy can be a useful technique to obtain information regarding the anisotropy in the EVDF.

Polarization-resolved measurements of the hydrogen Lyman-α line at 121.57 nm have been made in the Large Helical Device (LHD). In order to correlate the experimentally observed polarization degree with the anisotropy in the EVDF the Population-Alignment Collisional-Radiative (PACR) model is absolutely necessary Owing to the simple energy level structure relating to the Lyman-α line, construction of an accurate theoretical model is possible and therefore, this spectral line has been chosen for this study. In present study we deal with the polarization in Lyman-α line caused by anisotropic collisions with electrons. This thesis work is mainly divided into two parts:

1. development of the PACR model for Lyman-α line
2. measurement of polarization in Lyman-α line from the edge LHD plasma

Part-1: Development of the PACR model for Lyman-α line

Since the Lyman-α line at 121.57 nm is emitted due to radiative transition $1S - 2P$, information of processes which are governing population and depopulation of 2P level is required for construction of the theoretical model. The results of collisional-radiative calculations show that for typical electron temperature (T_e) and density (n_e) values at the observed region , i.e., for T_e : 10 eV–30 eV and n_e : $10^{18}\,m^{-3}$–$10^{19}\,m^{-3}$, the dominant populating and depopulating processes concerning 2P level are the electron impact excitation from the ground state and the radiative decay to ground state, respectively. On the basis of this knowledge rate equations have been constructed in the theoretical model.

We have developed the PACR model for the Lyman-α line. In the model each energy level is assigned with two quantities: population and alignment. The rate equations for the population and the alignment have been solved under the quasi steady-state approximation. The present model treats anisotropic EVDF having different electron temperatures in the directions parallel and perpendicular to the magnetic field. The theoretical polarization degree has been evaluated by considering the actual geometry of measurements and the plasma parameters at Lyman-α emission region.

Part-2 : Measurement of polarization in Lyman-α line from the edge LHD plasma

The polarization measurement system on LHD consists of a normal incidence VUV spectrometer (McPherson model 2253) with a CCD (Charge Coupled Device) detector, and additionally installed optical components provided by

the CLASP (Chromospheric Lyman-Alpha Spectro-Polarimeter) team. These optical components are a high-reflectivity mirror, a polarization analyzer and a half-waveplate. The components are specially designed and developed to be used at the Lyman-α wavelength and their performance is strongly wavelength dependent. Therefore, the comprehensive testing programs of these components have been carried out by utilizing the UVSOR (Ultraviolet Synchrotron Orbital Radiation) facility at the Institute for Molecular Sciences in Okazaki, Japan.

The focal length of the spectrometer is 3 m and the working wavelength range is from 30 nm to 320 nm. A back-illuminated CCD detector, Andor model DV435 with 1024×1024 pixels, is placed at the exit slit of the spectrometer to record the spectra. The high-reflectivity mirror and the polarization analyzer have been installed before the CCD detector inside the spectrometer. The analyzer, based on Brewster's angle reflection, only reflects linearly polarized light in the vertical direction to the detector. Since the Polarization analyzer must be used at its Brewster's angle, 68°, an optical component is required through which a diffracted light coming from the grating is directed to the polarization analyzer in such a way that the incidence angle is 68°. To meet this requirement, the high-reflectivity mirror is placed at 23° angle with respect to a diffracted light beam coming from the grating. The half-waveplate is placed just after the entrance slit and it is continuously rotated during the measurement. During measurements the cycle time of the Lyman-α line spectral observation is 50 ms with an exposure time of 16 ms, and the period of the half-waveplate rotation is 0.8 s. Under such conditions, linearly polarized light at every 45° angle is monitored.

The intensity in the background subtracted spectrum is integrated over the certain wavelength range for each time frame and the result is plotted as a function of time to obtain the temporal profile of Lyman-α line. In the present analysis, the integrated intensities of the hydrogen and deuterium lines are considered. Here, the angle of the observed linearly polarized light is defined as "polarization angle" and it is measured in the clockwise direction seen from the grating with reference to the vertical axis. The intensity shows a modulation which is synchronized with

the half-waveplate rotation period. This result clearly indicates that the Lyman-α line is polarized.

The polarization degree is defined as

$$P = (I_{\max} - I_{\min})/(I_{\max} + I_{\min}),$$

where $I_{\max}$ and $I_{\min}$ stand for maximum and minimum intensities in temporal profile, respectively. The least-squares fitting is performed on the temporal variation of the intensity, $I(t)$, with a function

$$I(t) = f(t)[1 + P\sin(\omega t + \theta)],$$

where $f(t)$ represents the global intensity variation, which is here expressed by a second order polynomial function, ω is fixed at 10π in the present case, P is the polarization degree, and θ is the phase offset.

Study: Dependence of polarization degree on electron density

Following the above mentioned procedure polarization degree has been evaluated for many LHD discharges with different plasma configurations. The previous studies done on LHD plasma indicate that the dominant hydrogen emissions can be approximated to be at $r_{\text{eff}} = 0.67\,\text{m}$, where r_{eff} is the effective minor radius of the plasma. The dependence of polarization degree on electron density at hydrogen emission location has been investigated. It is expected that with increasing n_{e} polarization degree should decrease due to two possibilities : (i) anisotropy in the EVDF itself reduces and (ii) collisional relaxation of population imbalance among the magnetic sublevels. However, the results suggest that polarization degree does not show any clear dependence on n_{e}.

Study: Phase analysis of measured intensity profile

The synthetic intensity profiles for the Lyman-α emission at the inboard and outboard sides have been generated by using the magnetic field data at $r_{\mathrm{eff}} = 0.67\,\mathrm{m}$ on the spectrometer line of sight, i.e., at $Z = -0.4\,\mathrm{m}$, to understand variation of an experimental intensity with a polarization angle (phase of intensity profile). From such investigation information regarding the dominant emission location and regarding the relation between the experimental intensity and the magnetic field direction can be inferred. These results suggest that the electron temperature in the direction perpendicular to the magnetic field ($T_{\perp}$) is higher than that in the direction parallel to the magnetic field ($T_{\parallel}$). The results also indicate that the dominant contribution in the polarized emission is from the plasma at the inboard side of the device.

Study: Dependence of anisotropy in the EVDF on electron density and temperature

By comparing the experimental results with the theoretical results the anisotropy in the EVDF has been evaluated for many LHD discharge with different plasma conditions. The variation in anisotropy with n_{e} and T_{e} has been investigated. It has been observed that anisotropy in the EVDF exhibits dependence mainly on T_{e} and it increases with increasing T_{e}. This behavior can be attributed to the reduction in collisionality with increase in T_{e}.

In conclusion, the results on polarization spectroscopy of Lyman-α obtained through the present thesis work give valuable information regarding anisotropy in the EVDF in the edge region of LHD plasma, which is essential for clear understanding of plasma confinement in the LHD plasma.

References

[1] Takashi Fujimoto and Atsushi Iwamae. *Plasma polarization spectroscopy*. Springer, 2008.

[2] John Wesson and David J Campbell. *Tokamaks*, volume 149. Oxford university press, 2011.

[3] Thomas J Dolan, Ralph W Moir, Wallace Manheimer, Lee C Cadwallader, and Martin J Neumann. *Magnetic fusion technology*. Springer, 2013.

[4] Denis Keefe. Inertial confinement fusion. *Annual Review of Nuclear and Particle Science*, 32(1):391–441, 1982.

[5] J Ongena, R Koch, R Wolf, and H Zohm. Magnetic-confinement fusion. *Nature Physics*, 12(5):398–410, 2016.

[6] JL Luxon, TC Simonen, RD Stambaugh, and DIII-D Team. Overview of the diii-d fusion science program. *Fusion Science and Technology*, 48(2):807–827, 2005.

[7] H Ninomiya et al. Jt-60u experimental results aimed at steady-state operation of a tokamak reactor. *Fusion engineering and design*, 51:1015–1023, 2000.

[8] Akio Komori, H Yamada, S Imagawa, O Kaneko, K Kawahata, K Mutoh, N Ohyabu, Y Takeiri, K Ida, T Mito, et al. Goal and achievements of large helical device project. *Fusion Science and Technology*, 58(1):1–11, 2010.

[9] Victor Bykov, Felix Schauer, Konstantin Egorov, Andrey Tereshchenko, Paul van Eeten, Andre Dübner, Manfred Sochor, Daniel Zacharias, Andrzej Dudek,

Wenge Chen, et al. Structural analysis of w7-x: Overview. *Fusion Engineering and Design*, 84(2-6):215–219, 2009.

[10] R Aymar, P Barabaschi, and Y Shimomura. The iter design. *Plasma physics and controlled fusion*, 44(5):519, 2002.

[11] Ryohei Makino, Shin Kubo, Takeshi Ido, Kenji Tanaka, Takashi Shimozuma, Yasuo Yoshimura, Masaki Nishiura, Hiroe Igami, Hiromi Takahashi, Akihiro Shimizu, et al. Local and fast density pump-out by ecrh in the lhd. *Plasma and Fusion Research*, 8:2402115–2402115, 2013.

[12] T Yamaguchi, KY Watanabe, S Sakakibara, Y Narushima, K Narihara, T Tokuzawa, K Tanaka, I Yamada, M Osakabe, H Yamada, et al. Measurement of anisotropic pressure using magnetic measurements in lhd. *Nuclear fusion*, 45(11):L33, 2005.

[13] T Yamaguchi, KY Watanabe, S Sakakibara, K Ida, Y Narushima, K Narihara, K Tanaka, T Tokuzawa, M Yoshinuma, T Kobuchi, et al. The effect of net toroidal current on the measurement of diamagnetic beta value in heliotron plasma. *Plasma physics and controlled fusion*, 48(9):L73, 2006.

[14] W Zwingmann, LG Eriksson, and P Stubberfield. Equilibrium analysis of tokamak discharges with anisotropic pressure. *Plasma physics and controlled fusion*, 43(11):1441, 2001.

[15] Hiroshi Aikawa. The measurement of the anisotropy of electron distribution function of a magnetized plasma. *Journal of the Physical Society of Japan*, 40(6):1741–1749, 1976.

[16] Taiichi Shikama, Shinichiro Kado, Shin Kajita, and Satoru Tanaka. The effect of superthermal electrons on mach probe diagnostics. *Japanese journal of applied physics*, 43(2R):809, 2004.

[17] RL Stenzel, W Gekelman, N Wild, JM Urrutia, and D Whelan. Directional velocity analyzer for measuring electron distribution functions in plasmas. *Review of Scientific Instruments*, 54(10):1302–1310, 1983.

[18] MD Bowden, T Okamoto, F Kimura, H Muta, Kiichiro Uchino, K Muraoka, T Sakoda, M Maeda, Y Manabe, M Kitagawa, et al. Thomson scattering measurements of electron temperature and density in an electron cyclotron resonance plasma. *Journal of applied physics*, 73(6):2732–2738, 1993.

[19] E Yatsuka, T Hatae, and Y Kusama. Principles for local measurement of anisotropic electron temperature of plasma using incoherent thomson scattering. *Nuclear Fusion*, 51(12):123004, 2011.

[20] F Skiff, DA Boyd, and JA Colborn. Measurements of electron parallel-momentum distributions using cyclotron wave transmission. *Physics of Fluids B: Plasma Physics*, 5(7):2445–2450, 1993.

[21] DJ Thuecks, F Skiff, and CA Kletzing. Measurements of parallel electron velocity distributions using whistler wave absorption. *Review of Scientific Instruments*, 83(8):083503, 2012.

[22] S. A. Kazantsev, L. Y. Margolin, N. Y. Polynovskaya, L. N. Pyatnitskii, A. G. Rys, and S. A. Edelman. Possibilities of plasma polarization spectroscopy. *Optics and Spectroscopy*, 55:326–327, September 1983.

[23] R Kano, J Trujillo Bueno, A Winebarger, F Auchère, N Narukage, R Ishikawa, K Kobayashi, T Bando, Y Katsukawa, M Kubo, et al. Discovery of scattering polarization in the hydrogen lyα line of the solar disk radiation. *The Astrophysical Journal Letters*, 839(1):L10, 2017.

[24] Ryohko Ishikawa, Ryouhei Kano, Takamasa Bando, Yoshinori Suematsu, Shin-nosuke Ishikawa, Masahito Kubo, Noriyuki Narukage, Hirohisa Hara, Saku Tsuneta, Hiroko Watanabe, et al. Birefringence of magnesium fluoride in the vacuum ultraviolet and application to a half-waveplate. *Applied optics*, 52(34):8205–8211, 2013.

[25] Noriyuki Narukage, Masahito Kubo, Ryohko Ishikawa, Shin-nosuke Ishikawa, Yukio Katsukawa, Toshihiko Kobiki, Gabriel Giono, Ryouhei Kano, Takamasa

Bando, Saku Tsuneta, et al. High-reflectivity coatings for a vacuum ultraviolet spectropolarimeter. *Solar Physics*, 292(3):40, 2017.

[26] Atsuo Iiyoshi, A Komori, A Ejiri, M Emoto, H Funaba, M Goto, K Ida, Hiroshi Idei, S Inagaki, S Kado, et al. Overview of the large helical device project. *Nuclear Fusion*, 39(9Y):1245, 1999.

[27] M Fujiwara, O Kaneko, A Komori, H Yamada, N Ohyabu, K Kawahata, PC DeVries, M Emoto, H Funaba, M Goto, et al. Experiments on nbi plasmas in lhd. *Plasma Physics and Controlled Fusion*, 41(12B):B157, 1999.

[28] T Mutoh, R Kumazawa, T Seki, F Simpo, S Masuda, and T Watari. Development of steady-state icrf heating for lhd. *Fusion Engineering and Design*, 26(1-4):387–394, 1995.

[29] Shin Kubo, T Shimozuma, Y Yoshimura, T Notake, Hiroshi Idei, S Inagaki, M Yokoyama, K Ohkubo, R Kumazawa, Y Nakamura, et al. Extension and characteristics of an ecrh plasma in lhd. *Plasma physics and controlled fusion*, 47(5A):A81, 2005.

[30] H Takahashi, T Shimozuma, S Kubo, S Ito, S Kobayashi, Y Yoshimura, H Igami, Y Mizuno, Y Takita, T Mutoh, et al. The development of a 77-ghz, 1-mw ecrh system for the large helical device. *Fusion Science and Technology*, 57(1):19–26, 2010.

[31] Takashi Fujimoto. *Plasma spectroscopy*. Oxford University Press, 2004.

[32] Keiji Sawada and Takashi Fujimoto. Temporal relaxation of excited-level populations of atoms and ions in a plasma: Validity range of the quasi-steady-state solution of coupled rate equations. *Phys. Rev. E*, 49:5565–5573, Jun 1994.

[33] Igor Bray and ANDRIST Stelbovics. Calculation of electron scattering on hydrogenic. *Advances in Atomic, Molecular, and Optical Physics*, 35:209, 1995.

[34] Ratko K Janev, William D Langer, E Douglass Jr, et al. *Elementary processes in hydrogen-helium plasmas: cross sections and reaction rate coefficients*, volume 4. Springer Science & Business Media, 2012.

[35] Alain Omont. A. omont, prog. quantum electron. 5, 69 (1977). *Prog. Quantum Electron.*, 5:69, 1977.

[36] Takashi Fujimoto, Hironori Sahara, GEORGE Csanak, and SHON Grabbe. Atomic states and collisional relaxation in plasma polarization spectroscopy: axially symmetric case. Technical report, National Inst. for Fusion Science, 1996.

[37] Karl Blum. *Density matrix theory and applications*, volume 64. Springer Science & Business Media, 2012.

[38] Nilam RAMAIYA, Motoshi GOTO, Tetsutarou OISHI, and Shigeru MORITA. Study of lyman-α polarization due to anisotropic electron collisions in lhd. *Plasma and Fusion Research*, 14:3402083–3402083, 2019.

[39] Wade L Fite and RT Brackmann. Collisions of electrons with hydrogen atoms. ii. excitation of lyman-alpha radiation. *Physical Review*, 112(4):1151, 1958.

[40] William Roger Ott, WE Kauppila, and WL Fite. Polarization of lyman-α radiation emitted in electron collisions with hydrogen atoms and molecules. *Physical Review A*, 1(4):1089, 1970.

[41] GK James, JA Slevin, D Dziczek, JW McConkey, and Igor Bray. Polarization of lyman-α radiation from atomic hydrogen excited by electron impact from near threshold to 1800 ev. *Physical Review A*, 57(3):1787, 1998.

[42] A Hirabayashi, Y Nambu, M Hasuo, and T Fujimoto. Disalignment of excited neon atoms due to electron and ion collisions. *Physical Review A*, 37(1):83, 1988.

[43] C Stehlé and R Hutcheon. Extensive tabulations of stark broadened hydrogen line profiles. *Astronomy and Astrophysics Supplement Series*, 140(1):93–97, 1999.

[44] Tetsutarou Oishi, Shigeru Morita, Chunfeng Dong, Erhui Wang, Xianli Huang, Motoshi Goto, LHD Experiment Group, et al. Space-resolved 3 m normal incidence spectrometer for edge impurity diagnostics in the large helical device. *Applied optics*, 53(29):6900–6912, 2014.

[45] Shigeru Morita and Motoshi Goto. Space-resolved vuv spectroscopy using the 3 m normal incidence spectrometer with back-illuminated ccd detector in the lhd. *Review of scientific instruments*, 74(3):2036–2039, 2003.

[46] H Watanabe, N Narukage, M Kubo, R Ishikawa, T Bando, R Kano, S Tsuneta, K Kobayashi, K Ichimoto, and J Trujillo-Bueno. Ly-alpha polarimeter design for clasp rocket experiment. In *Solar Physics and Space Weather Instrumentation IV*, volume 8148, page 81480T. International Society for Optics and Photonics, 2011.

[47] Françoise Bridou, Mireille Cuniot-Ponsard, J-M Desvignes, Alexander Gottwald, Udo Kroth, and Mathias Richter. Polarizing and non-polarizing mirrors for the hydrogen lyman-α radiation at 121.6 nm. *Applied Physics A*, 102(3):641–649, 2011.

[48] LR Canfield, G Hass, and JE Waylonis. Further studies on mgf 2-overcoated aluminum mirrors with highest reflectance in the vacuum ultraviolet. *Applied optics*, 5(1):45–50, 1966.

[49] Atsushi Iwamae, Masayuki Hayakawa, Makoto Atake, Takashi Fujimoto, Motoshi Goto, and Shigeru Morita. Polarization resolved h α spectra from the large helical device: Emission location, temperature, and inward flux of neutral hydrogen. *Physics of plasmas*, 12(4):042501, 2005.

[50] Atsushi Iwamae, Atsushi Sakaue, Nobuhiro Neshi, Jun Yanagibayashi, Masahiro Hasuo, Motoshi Goto, and Shigeru Morita. Hydrogen emission location, temperature and inward velocity in the peripheral helical plasma as observed with plasma polarization spectroscopy. *Journal of Physics B: Atomic, Molecular and Optical Physics*, 43(14):144019, 2010.

Publications

1. “Study of Lyman-α polarization due to anisotropic electron collisions in LHD”
   Nilam Ramaiya, Motoshi Goto, Tetsutarou Oishi and Shigeru Morita
   Plasma and Fusion Research, Volume 14, 3402083 (2019).

2. “Polarization measurement of hydrogen Lyman-α in the Large Helical Device”
   N. Ramaiya, M. Goto, T. Oishi and S. Morita
   Journal of Physics : Conference Series 1289, 012038 (2019)

3. “Modeling of Lyman-α line polarization in fusion plasma due to anisotropic electron collisions”
   M. Goto and N. Ramaiya
   Journal of Physics : Conference Series 1289, 012011 (2019)

4. Measurement of polarization in Lyman-α caused by anisotropic electron collisions in LHD
   Nilam Ramaiya, Motoshi Goto, Tetsutarou Oishi and Shigeru Morita
   To be submitted to Review of Scientific Instruments